Synthesis and characterisation of biocompatible metal-organic frameworks for water treatment and NO_x removal application

By

Chen Wu

A Folio Submitted to
The Education University of Hong Kong
in Partial Fulfilment of the Requirement for
the Doctor of Philosophy

July 2025

Statement of Originality

I, WU Chen, hereby declare that I am the sole author of this folio. The materials presented herein are my original work, except for those sections derived from three journal articles, of which I am the first author. Two of these articles have been published, while the third has been submitted for publication. I affirm that I have adhered to all relevant academic integrity standards and university policies regarding originality and plagiarism in the preparation of this folio.

Abstract

This folio is a collection of three separate research papers which includes three experiments studies and each contribution can also be read as a stand-alone article. The first article explores the development and application of alkaline earth metal-based metal-organic frameworks (MOFs) for the efficient removal and sensing of copper(II) ions from aqueous solutions. The unique structural properties of these MOFs, characterized by high porosity and tunable surface areas, facilitate enhanced adsorption capabilities for copper ions. The study investigates the synthesis of various MOFs and their performance in capturing copper(II) ions, demonstrating that specific structural modifications can significantly improve their efficacy. Additionally, the article examines the mechanisms underlying the adsorption processes, emphasizing the role of coordination interactions. The results highlight the potential of alkaline earth metal-based MOFs as sustainable and effective materials for environmental remediation, offering promising avenues for future research in heavy metal ion removal and sensing applications. The second article investigates the efficient removal of the pharmaceutical compounds piroxicam and ketoprofen using acid-modulated iron(III) MOFs. The study focuses on the synthesis of these MOFs, which are engineered through the strategic addition of acidic components to enhance their structural properties and adsorption capabilities. The performance of the acid-modulated iron(III) MOFs is thoroughly evaluated in terms of their ability to adsorb and eliminate the targeted drugs from aqueous solutions. Results demonstrate that the acid modification significantly improves the crystallinity and surface area of the MOFs, leading to enhanced adsorption performance. The adsorption mechanisms are also explored, providing insights into the interactions between the MOFs and the pharmaceutical compounds. This research highlights the potential of acid-modulated iron(III) MOFs as effective materials for the removal of contaminants from wastewater, contributing to the development of sustainable strategies for environmental protection. The third study explores the tuning of crystallinity in bismuth-based MOFs and their application in the removal of nitric oxide (NO) from gas streams. By systematically varying synthesis conditions, including temperature, reaction time, and ligand concentrations, we achieved bismuth MOFs with distinct crystallinities: amorphous, semi-crystalline, and well-crystallized structures. The impact of crystallinity on the adsorption performance for NO was rigorously evaluated, revealing that the amorphous structure demonstrated the highest efficiency in NO removal, followed by the semi-crystalline and well-crystallized variants. The enhanced performance of the amorphous MOF was attributed to its increased surface area and higher density of active sites, facilitating more effective gas adsorption. This research underscores the significance of crystallinity in optimizing the functionality of bismuth-based MOFs and highlights their potential as advanced materials for environmental remediation, specifically in addressing air pollution caused by nitrogen oxides.

Keywords: Metal-organic frameworks (MOFs), single crystal, phase control, water treatment, photocatalyst, NO_x removal.

Abbreviations

Metal–Organic Frameworks	MOFs
Matériaux de l'Institut Lavoisier-126	MIL-126
Acetic Acid	AA
Biphenyl-4,4′-dicarboxylic acid	H_2BPDC
Piroxicam	PIR
Ketoprofen	KET
Pharmaceuticals and Personal Care Products	PPCP
Dimethylformamide	DMF
Powder X-Ray Diffraction	XRD
X-Ray Photoelectron Spectroscopy	XPS
Fourier-Transform Infrared Spectroscopy	FTIR
Brunauer–Emmett–Teller	BET
Thermogravimetric Analysis	TGA
Scanning Electron Microscopy	SEM
Energy-Dispersive X-ray Spectroscopy	EDS
Ultraviolet–Visible Spectroscopy	UV–vis
Barrett–Joyner–Halenda	BJH
Cambridge Structural Database	CSD
2-Aminoterephthalic Acid	$H_2BDC\text{-}NH_2$
2,3,6,7,10,11-Hexahydroxytriphenylene	HHTP
Crystalline Bi-MOF	C-MOF
Semi-crystalline Bi-MOF	S-MOF
Amorphous Bi-MOF	A-MOF
Zeolitic Imidazolate Framework-67	ZIF-67

Triethylamine	TEA
Nitric Oxide	NO
Nitrogen Dioxide	NO_2
Ultraviolet–Visible Diffuse Reflectance Spectroscopy	UV-vis DRS
X-Ray Absorption Near-Edge Structure	XANES
Extended X-Ray Absorption Fine Structure	EXAFS
Wavelet Transform EXAFS	WT-EXAFS
Selected-Area Electron Diffraction	SAED
Electrochemical Impedance Spectroscopy	EIS
Photoluminescence	PL
Time-Resolved Photoluminescence	TRPL
Oxygen Reduction Reaction	ORR
5,5-Dimethyl-1-pyrroline-N-oxide	DMPO
p-Benzoquinone	PBQ
tert-Butyl Alcohol	TBA
Secondary Building Unit	SBU
Hard and Soft (Lewis) Acids and Bases	HSAB
Parts per Billion	ppb
Ligand-to-Metal Ratio	L/M ratio

Acknowledgement

I would like to express my heartfelt gratitude to those who have supported me throughout my PhD journey. First and foremost, I am deeply thankful to Dr. Vonika Ka-Man Au for her invaluable guidance during my initial years of study. Her mentorship laid a solid foundation for my research and inspired my passion for the field. Following Dr. Au departure to Japan, I had the privilege of joining Professor Wing-kei Ho research group. I am profoundly grateful for his insightful direction and encouragement, which have shaped my research endeavours.

I would also like to extend my sincere appreciation to Dr. Pui-Yu Ho, Dr. Xing Qin and Dr. Min Zhou for their unwavering support and assistance since my enrollment. Their expertise and willingness to share knowledge have greatly enriched my academic experience and provided me with the tools necessary to navigate the challenges of my research. Additionally, I want to acknowledge my parents for their endless support and encouragement. Their belief in my abilities has been a constant source of motivation, and I am forever grateful for their love throughout my academic journey.

Lastly, I would like to thank my fellow lab members and friends for their camaraderie and collaboration. The stimulating discussions and shared experiences have made this journey productive and enjoyable.

Preface

This folio is prepared as part of the PhD Programme to include three journal papers. Paper 1 was published in the Journal of Solid State Chemistry, paper 2 in the Journal of Industrial and Engineering Chemistry, and the manuscript of Paper 3 was submitted to Advanced Functional Materials. The publication details as below:

Paper 1: Wu, C., Low, K.-H., & Au, V. K.-M. (2023). Efficient removal and sensing of copper(II) ions by alkaline earth metal-based metal–organic frameworks. *Journal of Solid State Chemistry*, 322, 123936. https://doi.org/10.1016/j.jssc.2023.123936.

Paper 2: Wu, C., & Au, V. K.-M. (2024). Efficient removal of piroxicam and ketoprofen by acid-modulated iron(III) metal–organic frameworks. *Journal of Industrial and Engineering Chemistry*, 129, 544–554. https://doi.org/10.1016/j.jiec.2023.09.013.

Paper 3: Wu, C., Mu, J., Wang, X., Ho, P.-Y., Zhou, M., Yang, C., Leung, C.-F., Huang, Y., & Ho, W.-K. Tunning bismuth metal-organic framework topology for enhanced photocatalytic NO oxidation. *Small*, e2502116. https://doi.org/10.1002/smll.202502116.

Table of Contents

List of Figures

Chapter 1

Chapter 2

Chapter 3

Chapter 4

List of Tables

Chapter 2

Chapter 3

Chapter 4

Chapter 1. A brief review of the metal-organic framework

1.1 Introduction

Metal-organic frameworks (MOFs) are a fascinating class of porous materials that consist of metal ions or clusters connected by organic ligands, forming a highly ordered three-dimensional structure (Yahgi et al., 2003). Their unique properties, including high surface area, tunable pore sizes, and versatile chemical functionalities, make them ideal candidates for various applications (Zhou et al., 2012), particularly in environmental remediation (Soni et al., 2023) and photocatalysis (Sun & Jiang, 2024). These characteristics make them highly effective as adsorbents for removing contaminants from aqueous solutions, including heavy metals like copper ions (Bakhtiari & Azizian, 2015) and organic pollutants such as pharmaceutical and personal care products (PPCPs) (Rastogi et al., 2021).

Copper ions, prevalent in industrial wastewater, pose significant environmental hazards due to their toxicity to aquatic life and potential to disrupt ecosystems (Wu et al., 2023). Traditional removal methods, such as chemical precipitation and ion exchange, often lack efficiency and sustainability (Raji et al., 2023). MOFs present a promising alternative; their customizable structures allow for enhanced adsorption capacities and selectivity for copper ions (Rao et al., 2017). This adaptability enables the development of tailored MOFs that can effectively capture and remove copper from water, mitigating its harmful effects. PPCPs, which include a wide range of substances like antibiotics, analgesics, and cosmetics, have become ubiquitous in water bodies, raising concerns regarding their ecological impacts and potential risks to human health. The persistent nature of these contaminants necessitates innovative removal strategies. MOFs have shown great promise in adsorbing PPCPs due to their large surface area and the ability to functionalize their surfaces, enhancing the specificity of interactions with these organic pollutants (Seo et al. 2016).

In addition to their roles as adsorbents, MOFs can also function as photocatalysts, particularly for the degradation of nitrogen oxides (NO), a significant air pollutant produced from vehicular emissions and industrial activities (Xiao et al., 2018). When exposed to light, specific MOFs can activate charge carriers that facilitate the breakdown of NO into less harmful substances, offering a dual approach to environmental remediation (Wang et al., 2012). The integration of MOFs as both adsorbents for copper ions and PPCPs and as photocatalysts for NO removal underscores their multifaceted potential in addressing multiple environmental challenges simultaneously.

1.2. Metal-organic framework

Metal-organic frameworks (MOFs) are crystalline materials that self-assemble through the coordination of metal nodes (secondary building units, or SBUs) and organic ligands via coordination bonds, resulting in infinite structures (Yahgi et al., 2003). The tunable characteristics of these frameworks, such as porosity, surface area, crystallinity, and degree of interpenetration, render them structure dependent functional materials (Zhou et al., 2012). Consequently, MOFs can be applied in various fields, including gas storage and separation, catalysis, sensing, drug delivery, adsorption, and antibacterial agents, etc (Kondo rt al., 1999, Li et al., 2009).

A stable metal-organic framework (MOF) is typically constructed through robust coordination bonds that can withstand attacks from guest molecules and other external energies (Yahgi et al., 2003). When the ligands and coordination environment remain unchanged, high charge density, high-valence metal ions can form stronger coordination bonds, resulting in more stable frameworks (He et al., 2021). This trend aligns with Pearson's Hard/Soft Acids and Bases (HSAB) principle and is supported by numerous observations in the study of MOFs (Ho, 1975) (Figure 1 (a)). Early MOFs predominantly utilized borderline transition metals such as Cu(II), Co(II), Ni(II), Cd(II), and Zn(II), which coordinated with hard base carboxylate ligands (Hamisu et al., 2020). A notable example is Yaghi and co-workers design a novel design concept in which negatively charged carboxylate linkers coordinate with positively charged transition metal-based nodes, resulting in a charge-neutral framework. This framework remains stable after the removal of solvent guest molecules, thereby providing the first instance of MOF-5 (Yaghi et al., 1999) (Figure 1 b) that exhibits permanent porosity. In addition, these frameworks are among the first to utilize transition metal cluster groups as nodes, thereby laying the groundwork for the development of more complex multinuclear secondary building units (SBUs) relative to single transition metal ions. Subsequently, Férey and co-workers synthesized the MIL-series (MIL = Materials of "Institut" Lavoisier) of MOFs, which employed carboxylate-based ligands as Lewis hard bases coordinating with metal ions like Fe^{3+}, Cr^{3+}, and Al^{3+}. This approach not only enhances the structural integrity of the MOFs but also ensures that they maintain their original framework in harsh environmental conditions (Dan-Hardi et al., 2012). Similarly, borderline acids that are classified as intermediate between soft and hard acids, such as the low-valent metals Co(II), Ni(II), Cu(II), and Zn(II), can also form strong bonds with azolate anions and other soft bases (Hamisu et al., 2020). An example of this is the imidazole-based framework derived from Zn(II) and imidazolates. Therefore, these complementary stability profiles illustrate how researchers can customize the design of metal-organic frameworks (MOFs) to suit specific applications.

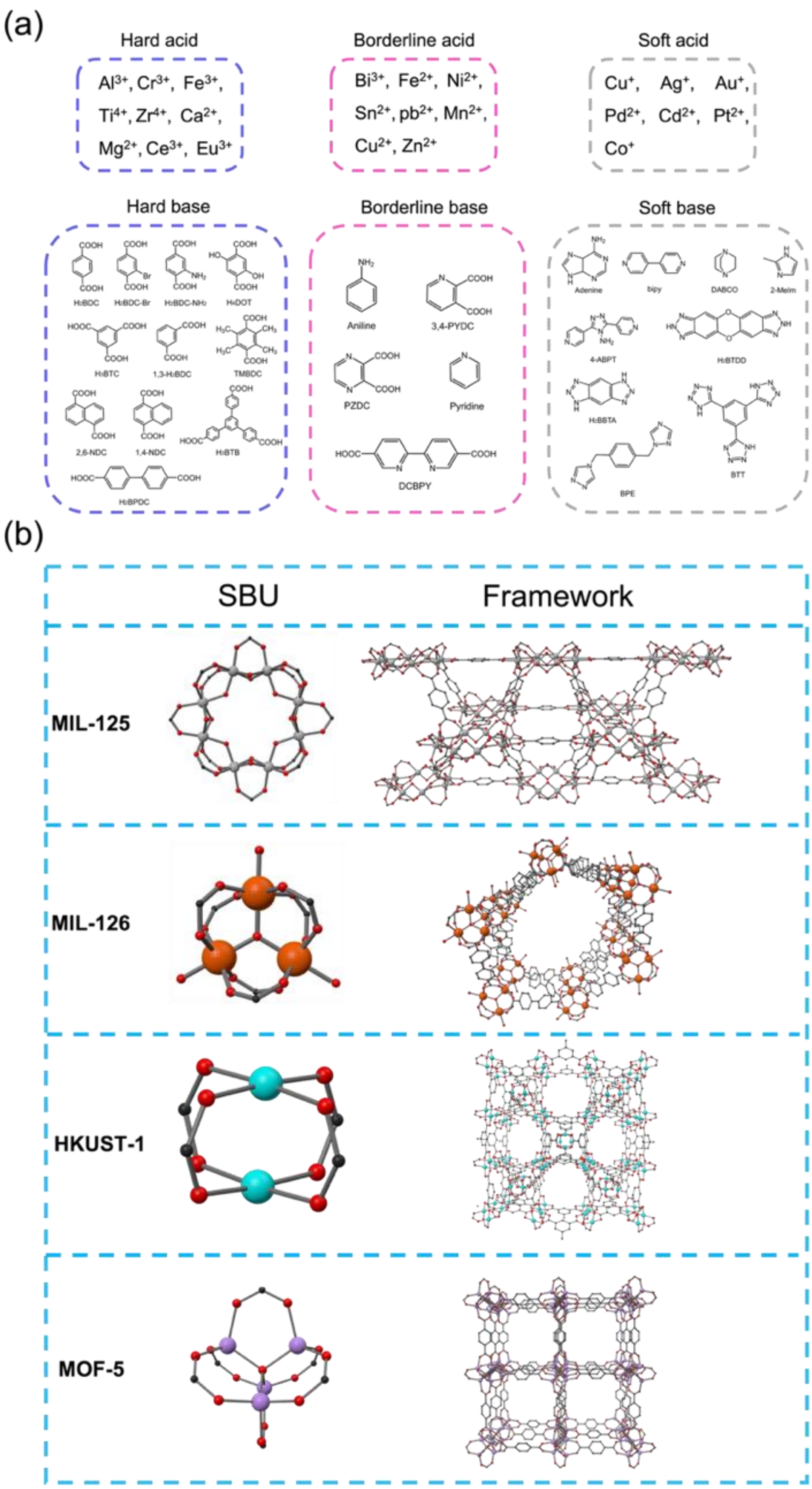

Figure 1. (a) Classification of Lewis acids (metal cations) and selected Lewis bases (ligands), (b) Four representative MOFs synthesized based on the HSAB principle.

1.2.1 Synthesis metal-organic framework

The methods used to synthesize MOFs significantly influence the formation of their skeletal structures. There are various synthesis techniques for MOFs, each of which directly affects the physical properties of the frameworks, including their crystal structure, morphology, size, porosity, and surface area (Yusuf et al., 2022). The most commonly used method is solvothermal synthesis (Jain et al., 2024) (Figure 2a), which typically occurs at temperatures ranging from room temperature to 250 °C. In this process, the metal source and ligand are dissolved in a solvent and then transferred into a Teflon-lined vessel. The microwave method is an environmentally friendly synthesis technique which has a short reaction time, allowing for precise control over the size of the resulting products (Liu et al., 2021) (Figure 2b). A modular MOF synthesis strategy has been developed by exploiting the formation of ligand and covalent bonds, in which monoacid ligands are reacted to form ditopic ligands (Lyu et al., 2019) (Figure 2c). The mechanochemical method for synthesizing MOFs offers several advantages, including reduced reaction times, lower solvent usage, and the ability to achieve high yields in a more environmentally friendly manner. This solid-state synthesis technique relies on mechanical energy, such as grinding or milling, to promote the formation of MOFs without the need for solvents, minimizing chemical waste and enhancing sustainability (Martinez et al., 2023) (Figure 2d). Electrosynthesis of MOFs offers significant advantages, including enhanced control over the synthesis process and the ability to selectively tune the framework's properties. By applying an electric field, this method facilitates the rapid formation of MOFs with improved crystallinity and uniformity, often at lower temperatures and in shorter reaction times compared to traditional methods (Guo et al., 2023) (Figure 2e). The sonochemical method for synthesizing MOFs leverages ultrasonic waves to enhance reaction kinetics, resulting in faster synthesis times and improved crystallinity. This approach generates localized high temperatures and pressures through cavitation bubbles, which can facilitate the self-assembly of metal ions and organic linkers with greater efficiency (Kazemi et al., 2023) (Figure 2f). The microfluidics method for synthesizing MOFs offers precise control over reaction conditions, enabling the rapid and reproducible production of uniform MOF structures. By manipulating small volumes of reactants in confined channels, this technique allows for fine-tuning of parameters such as temperature, flow rates, and concentrations, leading to enhanced control over crystallization and morphology (Koryakina et al., 2023) (Figure 2g). Ionothermal synthesis is a powerful method for producing MOFs that utilizes ionic liquids as both solvents and structure-directing agents. This approach offers several advantages, including the ability to achieve high reaction temperatures and pressures, which can promote the formation of highly crystalline and stable MOFs. The unique properties of ionic liquids, such as their tunability and low volatility, allow for enhanced solubility of metal salts and organic linkers, facilitating the self-assembly process. (Azbell et al., 2023) (Figure 2h).

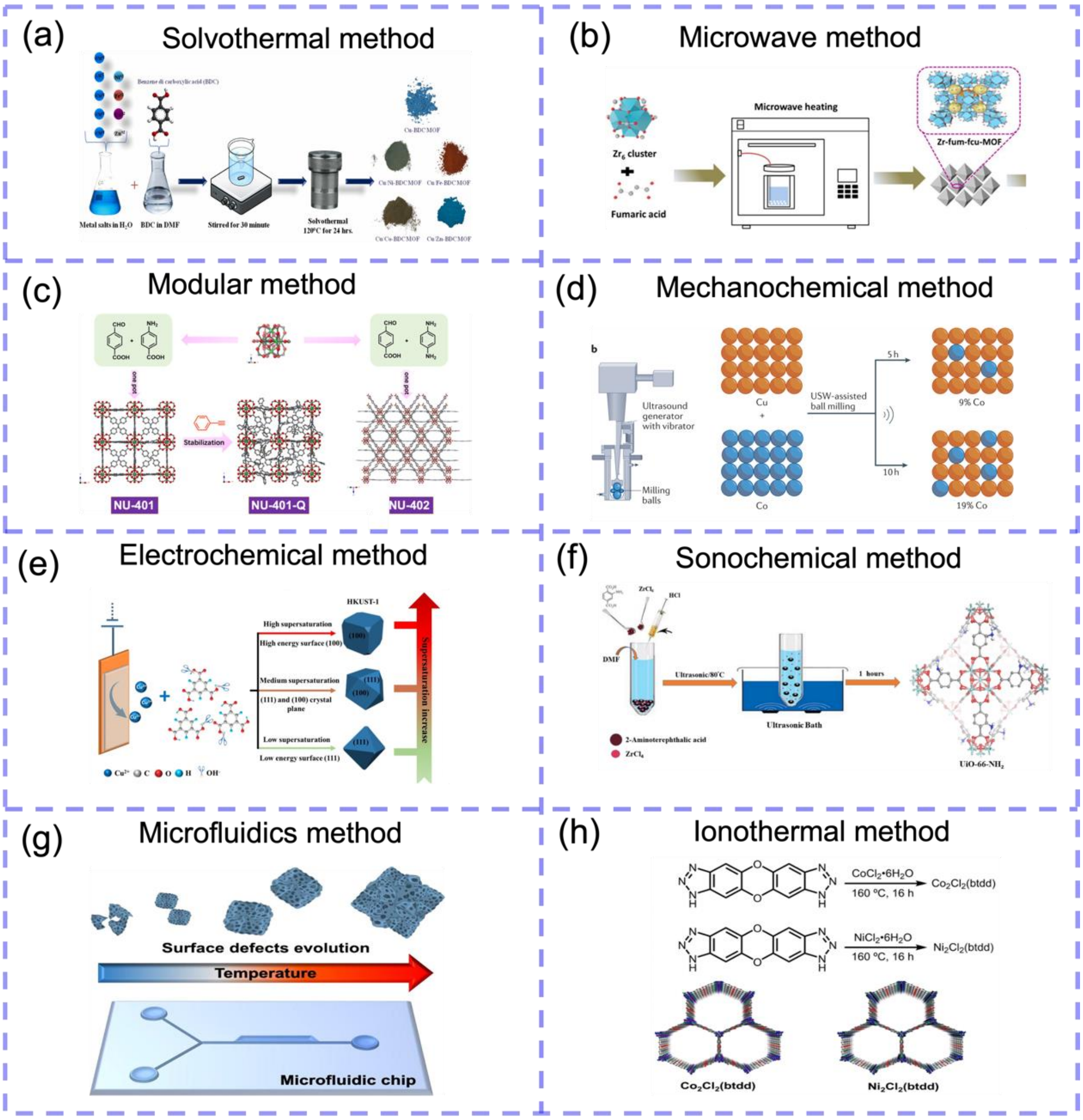

Figure. 2. The typical synthetic strategies for MOFs (a) Solvothermal method (Jain et al., 2024), (b) Microwave method (Liu et al., 2021), (c) Modular method (Lyu et al., 2019), (d) Mechanochemical method (Martinez et al., 2023), (e) Electrochemical method (Guo et al., 2023), (f) Sonochemical method (Kazemi et al., 2023), (g) Microfluidics method (Koryakina et al., 2023) and (h) Ionothermal method (Azbell et al., 2023).

1.2.2 MOF Nucleation and growth

Nucleation of metal-organic frameworks (MOFs) is a critical step in the formation of these versatile materials, which are composed of metal ions or clusters coordinated to organic ligands (Carpenter et al., 2023). MOFs are recognized for their high surface area, tunable porosity, and functional versatility, making them suitable for applications in gas storage, separation, catalysis, and drug delivery. The nucleation process entails the initial formation of small clusters or nuclei that serve as the foundation for the growth of larger crystalline structures (Carpenter et al., 2023). This process is often governed by thermodynamic and kinetic factors, which influence the stability and growth of nuclei (Cheetham et al., 2018). Three principal methodologies are utilized, either independently or in conjunction, to represent the nucleation and growth of MOFs: classical nucleation theory, nonclassical nucleation models, and the secondary building unit (SBU) model (Carpenter et al., 2023). The process of metal-organic framework (MOF) formation, as explained by classical nucleation theory (CNT), begins with the supersaturation of a solution containing metal ions and organic ligands. Under these conditions, small clusters of these components form spontaneously, competing between dissolution and growth. For a cluster to become a stable nucleus, it must reach a critical size, which requires overcoming an energy barrier associated with the balance of volume and surface energy contributions. Once this critical nucleus is established, it can grow by incorporating additional metal ions and ligands from the surrounding solution, eventually leading to the crystallization of well-defined MOF structures. Factors such as temperature, precursor concentration, and solvent choice play crucial roles in influencing the nucleation and growth dynamics, allowing for the optimization of synthesis conditions to tailor the properties of the resulting frameworks (Filez et al., 2021). The process of MOFs formation through non-classical nucleation theory involves the emergence of intermediates and metastable phases that deviate from the predictions of classical nucleation theory. In this framework, the initial stages of MOF crystallization can involve the formation of molecular clusters or solute-rich areas as precursors concentrate and phase separate from the bulk solution (Van Vleet et al., 2018). These solute-rich regions may condense into amorphous particles or dense liquid phases, serving as metastable states that facilitate the establishment of local supersaturation necessary for nucleation. The transition from these metastable phases to a critical nucleus involves overcoming an energy barrier, often through the aggregation of particles based on attractive forces. This transition can take the form of an amorphous-to-crystalline pathway, observed in various materials, where disordered metal-ligand-metal bonds rearrange into an ordered structure. Once a critical nucleus is formed, MOFs can grow through mechanisms such as particle attachment or oriented attachment, where either amorphous or crystalline precursors integrate into the growing crystal, ultimately leading to the formation of well-defined MOF structures. The secondary building unit (SBU) model of MOF nucleation theory posits that the formation of MOFs occurs through the assembly of discrete, pre-formed structural units rather than through the direct aggregation of individual metal ions and organic linkers (Carpenter et al., 2023). In this model, SBUs are composed of metal clusters coordinated to organic ligands, serving as the fundamental building blocks that dictate the overall architecture of the MOF. During the nucleation process, these SBUs can combine in various configurations to form larger aggregates, ultimately leading to the formation of the final crystalline structure. For example, McGrail and co-workers introduce the SBU nucleation of MIL-Cr(101), as shown in Figure 3b, all reactions leading to the SBU, initiated by hexaaquachromium(III) ions $[Cr(H_2O)_6]^{3+}$ and terephthalate linkers. The terephthalate linkers, also referred to as benzene dicarboxylate linkers, were modified at one end in their protonated form to cap the ends of the fully formed SBU (Cantu et al., 2014).

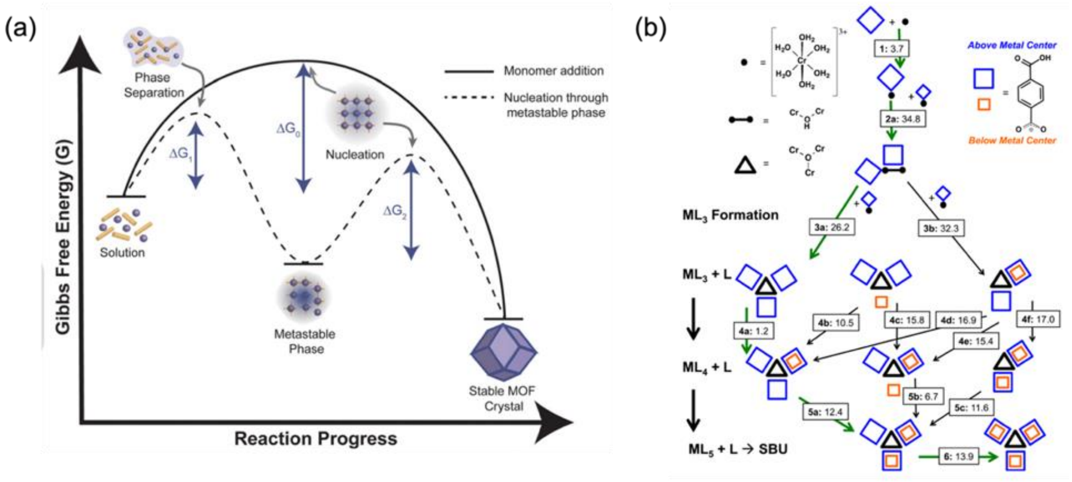

Figure 3. (a) A free energy diagram comparing two mechanisms: 1. monomer addition as described by classical nucleation theory, 2. nucleation via metastable phases as outlined in nonclassical nucleation theory (Carpenter et al., 2023). (b) Reaction series that lead to the formation of the SBU of MIL-101 (Cantu et al., 2014).

1.2.3 Morphology control

Designable morphologies and predictable properties represent some of the most challenging goals in materials engineering (Łuczak et al.,2023). The characteristics of MOFs, such as their shape, size, porosity, and aggregation rate, significantly influence their final performance and can be adjusted through synthesis parameters. However, achieving this requires a comprehensive understanding of the formation mechanisms of MOFs. Through literature analysis, it can be concluded that there are three mechanisms for controlling morphology: coordination modulation, protonation/deprotonation (acid-base regulation), and the regulation by surfactants/capping agents, respectively (Jiang et al., 2021). Coordination modulation, which involves the use of organic acids or bases that compete with ligands to disrupt the coordination equilibrium during crystal growth, was first introduced by the Kitagawa group in the synthesis of $[\{Cu_2(NDC)_2(dabco)\}]_n$ crystals through added acetic acid modulator that can be directly influence the coordination equilibria (Zahn et al., 2014). Forgan and co-workers investigated the effects of different template agents and their quantities on the morphology of the Fe-BDPC framework, demonstrating that the introduction of coordination modulation can slow down the self-assembly process, thereby favoring the thermodynamic product of the interpenetrated MIL-126(Fe) framework, while the non-interpenetrated MIL-88D(Fe) framework appears to be a kinetic product that can only be obtained without modulation (Bara et al., 2019). Different the competitive interaction with carboxylic acid ligands, the alteration of the acid-base environment within the reaction system can also influence the morphology of the final product by affecting the protonation/deprotonation equilibria. For example, Nayuk and co-workers developed a novel method to control crystal size by utilizing an excess of bridging bidentate ligands and various simple auxiliary monodentate ligands with different chemical functionalities (carboxylate, N-heterocycles, and alkylamines) (Cravillon et al., 2011). The function of the monodentate ligands can modulate the formation and deprotonation equilibrium of complexes during crystal nucleation and growth processes. A specific additive used to regulate crystal morphology is surfactants. The adsorption of amphiphilic compounds on the crystal surface can play a crucial role in altering crystal morphology and controlling particle size (Figure 3c). Depending on the affinity (interaction energy) of the surfactant for specific crystal facets, the adsorption can be either strong or weak. This differential adsorption can lead to an accelerated growth rate on one crystal facet while slowing down growth on another, thereby making it more difficult or easier for reactants to adhere to the surface (Cravillon et al., 2011). Consequently, the addition of surfactants influences the shape and size distribution of the final product. Furthermore, amphiphilic compounds can aggregate in water and other solvents, forming nanostructured soft matrices.

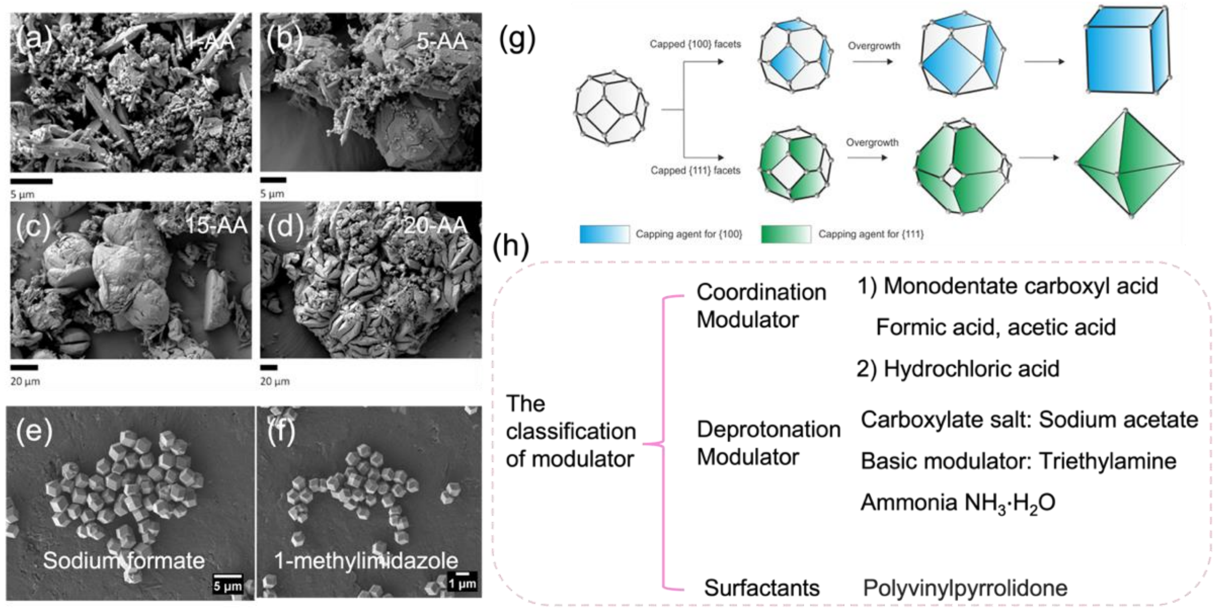

Figure 4. SEM images of MIL-126(Fe) synthesized with (a) 1, (b) 5, (c) 15, and (d) 20 equ acetic acid (Bara et al., 2019). SEM images of intermediate particle during the formation of microcrystals in the presence of (e) sodium dormmate and (f) 1-methylimidazole (Cravillon et al., 2011). (g) Controlling the morphology of metal-organic frameworks through the adsorption of surfactants on specific facets (Łuczak et al.,2023). (h) The brief conclusion of classification of the modulator.

In addition to the above mechanisms, several critical parameters, including pH, temperature, solvent type, and metal source, significantly influence the crystallization process, resulting in variations in particle size and morphology (Łuczak et al.,2023). Although these variations may pertain to a specific type of MOF and correspond to simulated powder X-ray diffraction (PXRD) patterns, differing morphologies can exhibit distinct functionalities. A comprehensive understanding of these parameters is essential for designing MOFs for specific applications, including gas storage, catalysis, and drug delivery. Wang and co-workers investigated the parameters for the fabrication of nanosized Dy(BTC)(H_2O) metal-organic framework crystals using sodium acetate as a modulator (Guo et al., 2012). SEM images (Figure 5a) revealed that the addition of one equivalent of sodium acetate resulted in rod-shaped crystals, while two equivalents led to rod-like submicron crystals with a gradually decreasing aspect ratio. When three equivalents of sodium acetate were present, spherical monodisperse nanoparticles were obtained. However, when the amount of sodium acetate exceeded 3.5 equivalents, the particle size increased again. In this case, the increase in particle size may be attributed to the rapid formation of small nuclei or nanoparticles in the presence of excess sodium acetate, which subsequently grow through aggregation (Guo et al., 2012). Guo and co-workers conducted an investigation into the morphological changes of Ni-MOF at various temperatures (Shen et al., 2022). Their findings indicated that at lower temperatures, Ni-MOF displayed a hexagonal structure. Further magnification revealed a clearly defined cross-linked network structure on the surface of Ni-MOF. Notably, the surface exhibited a significant smoothing effect as the temperature increased (Shen et al., 2022). Zhang and co-workers synthesized NH_2-MIL-53(Al) samples with various morphologies by controlling the ratios of DMF-water solvents. When pure DMF was used as the solvent, along with a small amount of added water, the product consisted of spherical crystal aggregates composed of numerous small crystals (Cheng et al., 2013). The morphology elongated as the water content increased and exhibited an ellipsoidal shape. Rhomboidal crystals were obtained when 100% water was used as the solvent (Cheng et al., 2013). Balan and co-workers investigated the influence of different zinc precursors on the morphology of ZIF-8 synthesis. By adjusting these parameters, various morphologies of MOFs can be achieved (Schejn et al., 2014). Meanwhile, a comparative analysis of their X-ray diffraction (XRD) patterns revealed that the simulated peaks remained almost unchanged. This observation indicates that modifications to the morphology of the MOFs can effectively lead to corresponding variations in their functional properties. Such findings underscore the potential of tailoring MOF structures to optimize their performance for specific applications.

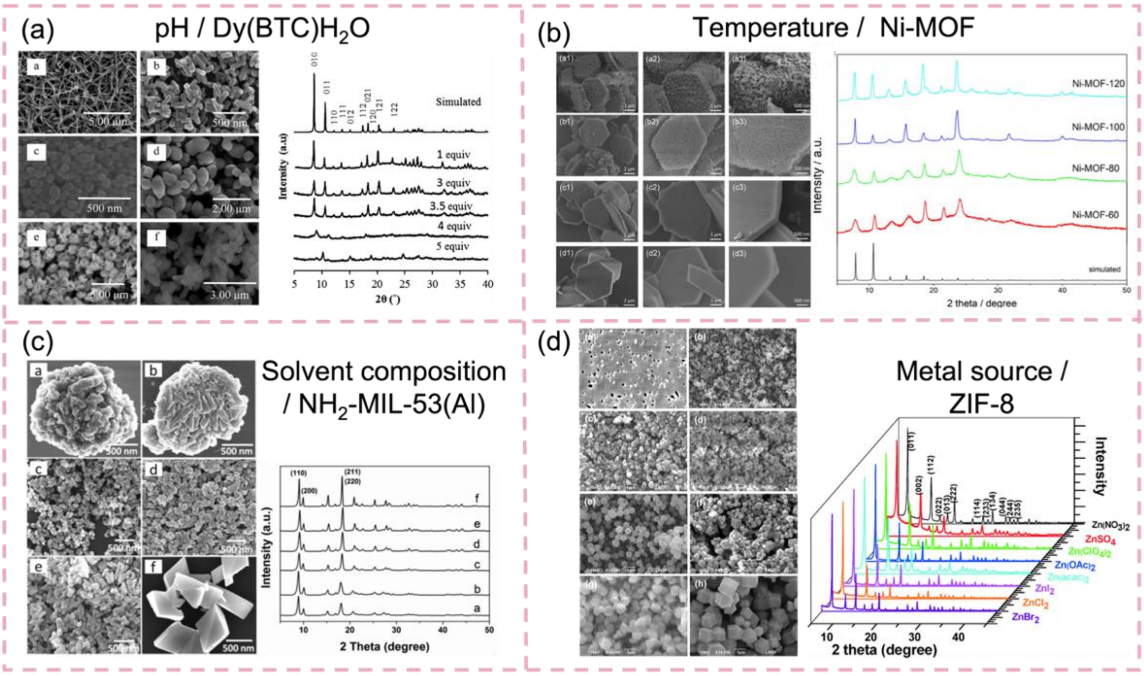

Figure 5 (a) SEM images (left side) and XRD patterns (right side) of Dy(BTC)(H_2O) synthesized with varying amounts of sodium acetate (Guo et al., 2012). (b) SEM images (left side) and XRD patterns (right side) of Ni-MOF synthesized in various temperatures (Shen et al., 2022). (c) SEM images (left side) and XRD patterns (right side) of NH2-MIL-53(Al) were synthesized in different compositions of DMF and water (Cheng et al., 2013). (d) SEM images (left side) and XRD patterns (right side) of ZIF-8 in various Zinc precusor (Schejn et al., 2014).

1.2.4 Three reprehensive topologies of MOF： crystalline, semi-crystalline and amorphous

Despite the well-documented success and widespread application of crystalline MOFs, there has been a notable surge of interest in amorphous and semicrystalline MOFs in recent years. This growing fascination can be attributed to several factors that highlight the unique properties and potential applications of these non-crystalline materials. Crystalline MOFs are characterized by their ordered structures, which result from the precise arrangement of metal ions and organic linkers (Ashling et al., 2019). This order imparts distinct features, such as high surface area, tunable porosity, and well-defined adsorption sites, making them highly effective for applications in gas storage, separation, catalysis, and drug delivery (Zou et al., 2024). However, the inherent limitations associated with crystalline MOFs, including their stability under varying environmental conditions and the challenges in synthesizing frameworks with uniformity and reproducibility, have led researchers to explore alternative structures. Amorphous MOFs, in contrast, lack long-range order, which results in a more flexible and dynamic framework. This absence of crystalline order can lead to enhanced structural diversity, allowing for tailored properties that may not be achievable with their crystalline counterparts (Wu et al., 2019). For instance, amorphous MOFs can exhibit improved stability in the presence of moisture and other solvents, making them suitable for applications in humid environments where crystalline structures might degrade (Lin et al., 2023). Additionally, the increased flexibility of amorphous performance in gas storage and separation applications. The semicrystalline category represents a hybrid state between crystalline and amorphous structures, where the framework exhibits both ordered and disordered regions. This unique characteristic allows for the retention of some desirable properties of crystalline MOFs, such as high surface area and porosity, while simultaneously benefiting from the enhanced stability and flexibility associated with amorphous materials.

1.3 The relationship among the three publications

The three articles all design environmentally friendly MOFs. The first article focuses on alkaline-based metal-based MOFs, the second on iron-based MOFs, and the third one is bismuth-based MOFs. Environmentally friendly MOFs are designed to focus on sustainability, utilizing non-toxic metal ions and biodegradable organic linkers to minimize environmental impact. These MOFs are constructed from non-toxic materials and renewable resources, reducing the risk of pollution and toxicity associated with conventional MOFs that may contain harmful chemicals. The production of these materials generates less waste and reduces energy consumption.

In the first article, as I have just started exploring the field of MOFs, I chose to begin with the synthesis of single crystals, which is a crucial technique in the design and synthesis of MOFs. By continuously adjusting the ratio of metal to ligand, as well as varying the volume of the solvent and the reaction temperature, I successfully obtained my first single crystal after delving into this area. This result laid the foundation for future crystal design. Subsequently, I utilized this environmentally friendly material for the adsorption of copper ions from aqueous solutions.

Inspired by the first article, I confirmed that adjusting the parameters in the synthesis of MOFs can alter their morphology. Different morphologies of MOFs can lead to significantly different applications in the same field. Therefore, in my second project, I chose iron as the metal source and H_2BPDC as the ligand. By varying the amount of acetic acid, I aimed to modify the morphology of Fe-BPDC and apply it to the adsorption of pharmaceuticals. I found that the Fe-BPDC synthesized with a small amount of acid exhibited a mixed-phase structure with poor crystallinity yet demonstrated very strong adsorption performance for the pharmaceuticals. Conversely, when a larger amount of acid was added, the crystallinity increased, but the adsorption performance did not improve. This suggests that the addition of the modulator agent created a competitive interaction with the ligand. Consequently, the product with a small amount of acid contained the highest number of Fe−O bonds. Therefore, I infer that the adsorption of pharmaceuticals by Fe−BPDC primarily relies on coordination interactions.

In the third article, inspired by the findings of the second article, I recognized that MOFs can consist not only of materials with high crystallinity but also of mixed-phase materials. I pursued this direction further and discovered that recent research has extensively studied amorphous and semi-crystalline structures of MOFs. In addition to alkaline metal series and iron-based MOFs, bismuth—a biocompatible and environmentally friendly metal—has also gained attention in recent years. Therefore, in my third project, I designed three different bismuth-based MOFs with varying degrees of crystallinity and applied them to the degradation of nitric oxide (NO). Ultimately, I found that among the three MOFs with different crystallinities, the amorphous structure exhibited the best performance, followed by the semi-crystalline structure, while the well-crystallized material performed the least effectively. This work also proposes a research direction for the development of MOFs with different crystallinities.

Therefore, this collection of works illustrates a progressive evolution in material design, beginning with the straightforward synthesis of alkaline metal-based MOFs, advancing to the exploration of iron-based frameworks, and culminating in the more complex development of bismuth-based MOFs. This trajectory not only reflects the increasing sophistication and versatility in the design of these materials but also highlights the innovative approaches taken to enhance their performance and applicability in various environmental remediation processes. Each phase of this research contributes to a deeper understanding of how adjustments in the choice of metal sources and structural characteristics can significantly influence the effectiveness of MOFs in tackling specific challenges, such as pollutant degradation.

By exploring the synthesis parameters and their impact on the properties and performance of these frameworks, this thesis aims to elucidate the relationship between material design and functionality, ultimately contributing to the advancement of sustainable strategies for environmental remediation. Each study encapsulates significant findings that not only demonstrate the efficacy of the developed MOFs but also pave the way for future research in this vital field.

Chapter 2 Paper 1-Efficient removal and sensing of copper(II) ions by alkaline earth metal-based metal–organic frameworks

Chen Wu[a,b], Kam-Hung Low[c], Vonika Ka-Man Au[a,b,*]

Abstract

A class of alkaline earth metal-based metal–organic frameworks (MOFs), namely ^{NDC}MOF(Ca) and ^{NDC}MOF(Sr), has been synthesized using 2,6-naphthalenedicarboxylic acid (NDC) as the linker. In view of the biocompatibility of the starting materials, these MOFs are expected to be environmentally benign and, in this work, have been employed for the removal of copper(II) ions (Cu^{2+}) from aqueous systems. The results showed that the maximum adsorption capacities of ^{NDC}MOF(Ca) and ^{NDC}MOF(Sr) for Cu^{2+} were 299.4 and 398.4 mg g^{-1}, respectively, which were comparable to those of related MOFs and porous materials. Meanwhile, ^{NDC}MOF(Ca) and ^{NDC}MOF(Sr) displayed blue luminescence in the solid state at room temperature upon photoexcitation with ultraviolet (UV) light. This emission would be readily quenched after the adsorption of Cu^{2+} ions. Such visible changes in the observed color and emission of the MOFs have rendered them versatile adsorbents and sensors for Cu^{2+} in the aqueous environment.

Keywords

Metal–organic framework; alkaline earth metal; adsorptive removal; heavy metal; copper(II)

1.Introduction

Metal–organic frameworks (MOFs) are crystalline materials consisting of organic linkers and inorganic metal nodes that are assembled together via coordination bonds (Zhou et al., 2012). The diversity of metal ions and organic linkers makes it possible to generate structures with tunable porous properties (Yaghi et al., 2003). The porosity, directional structure and large surface area of MOFs have made them good candidates for diverse applications (Kitagawa et al., 2022; Long et al., 2009; Li et al., 2009; He et al., 2014 and Zhang et al., 2022)), including gas sorption (Kondo et al., 1999) and separation (Duan et al., 2017 and Lin et al., 2019), catalysis (Phan et al., 2011, Fang et al., 2019 and Wu et al., 2022), drug delivery (Harrison et al., 2021 and Huxford et al., 2010) and sensing (Kumar et al., 2015 and Hu et al., 2014). Recently, there has been increasing interest in using MOFs for environmental remediation (Howarth et al., 2015; Hossain et al.,2022; Au et al., 2021 and Au et al., 2020) such as the adsorptive removal of heavy metal ions from aqueous media (Lv et al., 2019).

Copper(II) ions (Cu^{2+}) are usually released from factories. They are one of the common types of heavy metal ions that can be found in water, and their presence has aroused environmental concerns (Yang et al., 2022 and Basta et al., 2005). For example, plants are very sensitive to copper toxicity. Metabolic disturbances and growth inhibition would occur when the copper levels in tissues are only slightly above normal (Fernandes et al., 1991). Although the copper element plays an important role in the metabolism of biological systems and is a kind of micronutrient for humans, excess Cu^{2+} ions in the body would lead to serious toxicological problems such as nausea, vomiting and stomach cramps (Krstic et al., 2018). Therefore, it is of immense research interest to develop an efficient and economical method to reduce the concentration of Cu^{2+} in water sources. Adsorption is considered as an effective method to remove toxic ions because of its simple operation, high efficiency and reasonable cost-effectiveness(Abbasi et al., 2015). Recent biocompatibility data indicate that a few carboxylic acids such as 2,6-naphthalenedicarboxylic acid (NDC) are relatively non-toxic due to their highly polar character. On the other hand, alkaline earth metal-based MOFs exhibit many advantages compared to those based on other metals, especially because of their light and non-toxic nature (Matlinska et al., 2019). Considering that MOFs based on these biocompatible linkers and alkaline earth metals are relatively less studied (Purna et al., 2014), this work targets to explore the adsorption properties of MOFs based on alkaline earth metals and their applications in water remediation.

Herein, a series of three-dimensional MOFs based on the alkaline earth metals, namely calcium and strontium, has been synthesized and characterized. These MOFs have been utilized for the rapid removal and sensing of Cu^{2+} in aqueous systems. The kinetics and mechanism of adsorption have also been investigated in detail.

2. Experimental

2.1 Materials

Calcium nitrate tetrahydrate (99 %) and strontium nitrate (99.5 %) were purchased from Duksan Pure Chemicals Co. Ltd. and UNI-CHEM Chemical Reagents, respectively. Dimethylformamide (99.8 %) was obtained from TCI and 2,6-naphthalenedicarboxylic acid was from Acros. All other reagents and solvents were commercially available and used as received.

2.2 Physical measurements and instrumentation

Elemental analysis was performed on an Elementor vario EL cube CHNS Elemental Analyzer. Infrared spectra were obtained on a PerkinElmer Frontier FTIR spectrometer (4000-530 cm^{-1}) with a universal ATR accessory. Powder X-ray diffraction data were collected on a Bruker D8 ADVANCE Powder X-ray Diffractometer in Bragg-Brentano ($\theta/2\theta$) reflection mode with graphite monochromatized Cu-Kα radiation. X-Ray photoelectron spectroscopy was performed using a Nexsa G2 Surface Analysis System with a monochromatic 12kV aluminum K^{-1} X-ray source at the University Research Facility in Materials Characterization and Device Fabrication, The Hong Kong Polytechnic University.

Emission spectra were obtained on an Edinburgh Spectrofluorometer FS5. Thermogravimetric analysis was obtained on a PerkinElmer Thermogravimetric Analyzer TGA 4000. Brunauer–Emmett–Teller nitrogen adsorption-desorption isotherm tests were performed on a Micromeritics 3Flex adsorption analyzer. Scanning electron microscopy (SEM) was performed on a ZEISS Sigma 500 field emission scanning electron microscope. Ultraviolet-visible (UV-vis) absorption spectra were obtained on an Agilent Technologies Cary 8454 UV-vis spectrophotometer.

2.3 Crystal structure determination

Crystals suitable for X-ray diffraction were mounted on a MiTeGen dual-thickness micro-mount and placed under a cold stream of nitrogen (Oxford). Single-crystal X-ray diffraction measurements were recorded on a Bruker D8 VENTURE Duo FIXED-CHI X-Ray Diffractometer using a IμS micro-focus Mo-Kα radiation ($\lambda = 0.71073$ Å) with a Quazar multilayer optics. Data collection was conducted with the *APEX3* v2019.3-2click4 (Bruker Nano, 2019) program. Cell refinement and data reduction were performed with the *SAINT* V8.38A (Bruker AXS Inc., 2017) program. The structure was solved using *XT* 2014/5 (Sheldrick et al., 2015) in the APEX3 suite and refined with *SHELXL2018/3* (Sheldrick et al., 2015*)*. Hydrogen atoms were placed in idealized positions and were set riding on the respective parent atoms. All non-hydrogen atoms were refined with anisotropic thermal parameters. The structure was refined by weighted least squares refinement on F^2 to convergence. All e.s.d.'s (except the e.s.d. in the dihedral angle between two least-square planes) are estimated using the full covariance matrix. The X-ray crystallographic data of ^{NDC}MOF(Ca) have been deposited at the Cambridge Crystallographic Data Centre (CCDC), under the deposition number CCDC 2163583. The data can be obtained free of charge from the joint Cambridge Crystallographic Data Centre and Fachinformationszentrum Karlsruhe Access Structures service (https://www.ccdc.cam.ac.uk/structures).

2.4 Synthesis of ^{NDC}MOF(Ca) and ^{NDC}MOF(Sr)

^{NDC}MOF(Ca) and ^{NDC}MOF(Sr) were both synthesized by the solvothermal method. A mixture of the metal nitrate precursor (0.6 mmol) and NDC (66 mg, 0.3 mmol) was dissolved in 10 mL of dimethylformamide (DMF) and sonicated for 30 min. The mixture was subsequently heated at 120 °C for 24 hours. After cooling to room temperature, the crystalline product was washed with DMF and methanol, and then dried overnight under vacuum. ^{NDC}MOF(Ca) (Yield: 30 mg, 30 %) and ^{NDC}MOF(Sr) (Yield: 45 mg, 23 %) were respectively obtained as crystalline light-yellow and white solids. Elemental analysis calcd. (%) for [$CaC_{12}H_6O_4 \cdot DMF \cdot 0.5H_2O$]: C 53.56, H 4.20, N 4.16; found: C 53.61, H 3.84, N 3.78; for [$SrC_{12}H_6O_4 \cdot DMF \cdot 0.5H_2O$]: C 46.93 H 3.68, N 3.65; found: C 47.14, H 3.29, N 3.40.

3. Results and discussion

3.1 Synthesis

The alkaline metal-based metal organic frameworks, ^{NDC}MOF(Ca) and ^{NDC}MOF(Sr), were synthesized solvothermally from calcium nitrate tetrahydrate or strontium nitrate and NDC in DMF at 120 °C. Considering their biocompatibility and regular distribution of micropores, ^{NDC}MOF(Ca) and ^{NDC}MOF(Sr) are expected to be useful adsorbents for the removal of heavy metal ions such as Cu^{2+} from aqueous solutions as an environmentally friendly material. While the detailed adsorption studies will be discussed in Sections 3.8–3.10, the characterization of the Cu^{2+}-loaded MOFs will also be discussed in Sections 3.2–3 3.7 for the ease of comparison.

3.2 X-Ray diffraction studies

Single crystals of ^{NDC}MOF(Ca) suitable for X-ray diffraction analysis were obtained. Figure 1 shows the single crystal structure of as-synthesized ^{NDC}MOF(Ca) which exhibits an orthorhombic structure with a Pnma space group and is consistent with the report by Schröder and co-workers (Williams et al., 2008). Each calcium center is coordinated to eight oxygen atoms to form a CaO_8 unit. Figure 1a illustrates a pair of CaO_8 units that are connected to each other via bridging oxygen atoms. In the crystal structure, each NDC linker is coordinated to a calcium center as a bidentate ligand via two oxygen atoms, and one of these oxygen atoms further coordinates to another calcium center to form a secondary building unit (SBU) as shown in Figure 1d and c. Hence, each calcium is overall coordinated to two NDC linkers in bidentate mode, two NDC linkers in monodentate mode, and two bridging, disordered DMF molecules to form an eight-coordination sphere (Øien-Ødegaard et al.,2017). Similar CaO_8 coordination has been observed in other calcium MOFs (You et al., 2021) including a related MOF prepared with 1,4-naphthalenedicarboxylic acid (Kojima et al., 2018). When the SBU is viewed along the *a* axis as depicted in Figure 1d, the calcium nodes and NDC linkers would arrange in a manner that is similar to the paddlewheel units commonly observed in other MOFs such as those of copper (Au et al., 2019 and Gao et al., 2015) and zinc (Gadzikwa et al., 2009 and Bhunia et al., 2013). As shown in Figure 1e, the SBUs further coordinate to each other to form an extended framework with rhomboidal pores of about 18.1 Å × 6.7 Å. The coordinated DMF moieties are observed to point towards the center of the pores, approximately bisecting the porous channels. The crystallographic data of ^{NDC}MOF(Ca) are summarized in Table S1. Although single crystals of ^{NDC}MOF(Sr) have not been obtained, this MOF is expected to exhibit a structure that is analogous to ^{NDC}MOF(Ca) (Williams et al., 2008).

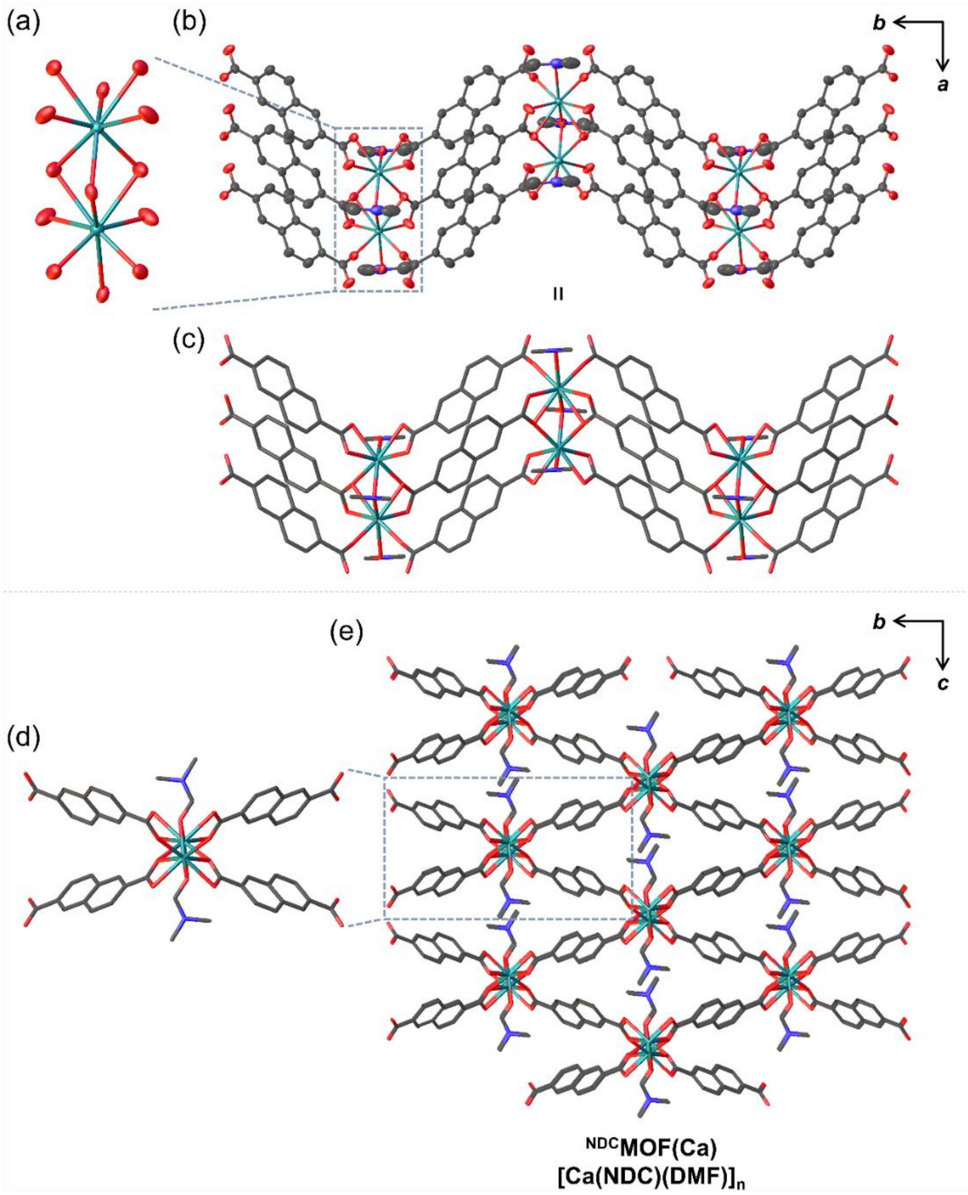

Figure 1. Single crystal structure of ^{NDC}MOF(Ca): Ball and stick models showing (a) a pair of coordinated calcium centers forming the CaO_8 core and (b) the secondary building unit (SBU) of ^{NDC}MOF(Ca). Wireframe models showing the SBU viewed (c) along the *c* axis and (d) along the *a* axis, and (e) the three-dimensional packing of ^{NDC}MOF(Ca). Calcium atoms are shown in cyan, carbon in grey, nitrogen in blue and oxygen in red. Hydrogen atoms are omitted and only one of the disordered positions of the DMF molecules is shown for clarity.

In addition, both ^{NDC}MOF(Ca) and ^{NDC}MOF(Sr) were structurally characterized by powder X-ray diffraction (PXRD) studies. Figure S1 depicts the simulated PXRD pattern of ^{NDC}MOF(Ca), as well as the experimental PXRD patterns of as-synthesized and Cu^{2+}-loaded ^{NDC}MOF(Ca) and ^{NDC}MOF(Sr). The experimental pattern of ^{NDC}MOF(Ca) was found to be consistent with the simulated pattern. The minor differences were caused by the evaporation of solvent molecules from the ^{NDC}MOF(Ca) powder and symmetry breaking, as dried powdery ^{NDC}MOF(Ca) was used for the PXRD studies whereas the single crystal sample was solvated. Furthermore, it has been reported in the literature that these MOFs were often synthesized as a multiphase material (Williams et al.,2008). The crystalline product tended to mix with the starting materials and/or other products, and this could be another probable cause of the additional minor peaks. ^{NDC}MOF(Sr), on the other hand, was observed to be a monophasic material according to the PXRD studies. When the PXRD patterns of both as-synthesized MOFs were compared, corresponding peaks could be identified and this suggested that the structure of ^{NDC}MOF(Sr) was analogous to that of ^{NDC}MOF(Ca). However, structural changes in the MOFs were observed after the adsorption of Cu^{2+} ions.

3.3 Infrared spectroscopy

Figure 2 illustrates the Fourier transform infrared (FTIR) spectra of the NDC linker, the as-synthesized MOFs (^{NDC}MOF(Ca) and ^{NDC}MOF(Sr)) and the Cu^{2+}-loaded MOFs (Cu^{2+}@^{NDC}MOF(Ca) and Cu^{2+}@^{NDC}MOF(Sr)). NDC showed a broad O–H stretch at 2250–3250 cm^{-1} from the COOH group. The absence of this broad O–H signal in ^{NDC}MOF(Ca) and ^{NDC}MOF(Sr), as well as the shift of the υ(C=O) vibration from about 1670 cm^{-1} in NDC to about 1648 cm^{-1} in ^{NDC}MOF(Ca) and 1645 cm^{-1} in ^{NDC}MOF(Sr) suggested the successful deprotonation of the carboxylic acid moieties and their coordination to calcium and strontium in the MOFs. A broad O–H peak at 3009 cm^{-1} for water appeared after the adsorption of Cu^{2+} from aqueous solutions. In addition, the peak at 1563 cm^{-1} in ^{NDC}MOF(Ca) and ^{NDC}MOF(Sr), which was assigned to aromatic C=C stretching, was shifted to about 1540 cm^{-1} in both Cu^{2+}-loaded MOFs.

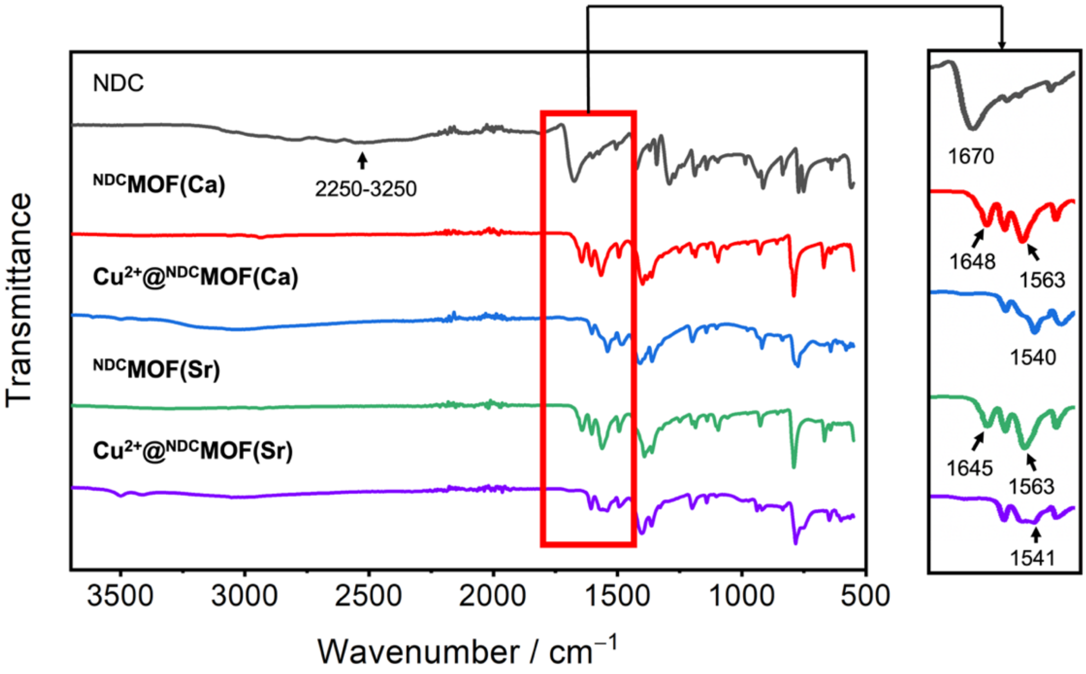

Figure 2. FTIR spectra of the NDC ligand, ^{NDC}MOF(Ca), Cu^{2+}@^{NDC}MOF(Ca), ^{NDC}MOF(Sr) and Cu^{2+}@^{NDC}MOF(Sr).

3.4 X-ray photoelectron spectroscopy (XPS)

In order to understand the adsorption mechanism of Cu^{2+} by the MOFs, XPS was conducted for both ^{NDC}MOF(Ca) and ^{NDC}MOF(Sr) before and after the adsorption of Cu^{2+}. As shown in Figure 3a, a new Cu 2p peak appeared in the broad scan spectrum of Cu^{2+}@^{NDC}MOF(Sr) at 934.58 eV (Chen et al.,2010), indicating that Cu^{2+} was successfully adsorbed by ^{NDC}MOF(Sr). The Cu 2p spectrum (Figure 3b) revealed obvious peaks at around 934.59 and 954.22 eV for $2p_{3/2}$ and $2p_{1/2}$, respectively, which was suggestive of the presence of Cu^{2+} (Wang et al., 2015). In addition, the presence of satellite peaks indicated the formation of CuO and/or $Cu(OH)_2$ on the surface of ^{NDC}MOF(Sr) (Wang et al., 2015; Zhu et al., 2017 and Biesinger et al., 2017). Furthermore, the apparent decrease in the intensity of the Sr 3d peak suggested the reduced amount of exposed Sr centers on the surface of the material, probably due to the binding of Cu^{2+} ions on the surface active sites of ^{NDC}MOF(Sr). The O 1s XPS spectrum of Cu^{2+} @^{NDC}MOF(Sr) (Figure 3d), on the other hand, showed a red shift from 531.28 eV to 531.68 eV when compared to ^{NDC}MOF(Sr) (Figure. 3c). Before the adsorption of Cu^{2+}, the O 1s spectrum of ^{NDC}MOF(Sr) consisted of three peaks at 530.58, 531.40 and 533.03 eV, which were attributed to the oxygen component of the Sr–O bond and the carboxylate groups of ^{NDC}MOF(Sr). Upon the adsorption of Cu^{2+}, the O 1s spectrum showed an additional peak at 529.83 eV, which was associated to either CuO or Cu(OH)$_2$ formed on the MOF surface (Biesinger et al., 2017). Similar observations were also found in the XPS analysis of ^{NDC}MOF(Ca) before and after the adsorption of Cu^{2+} (Figure. S2).

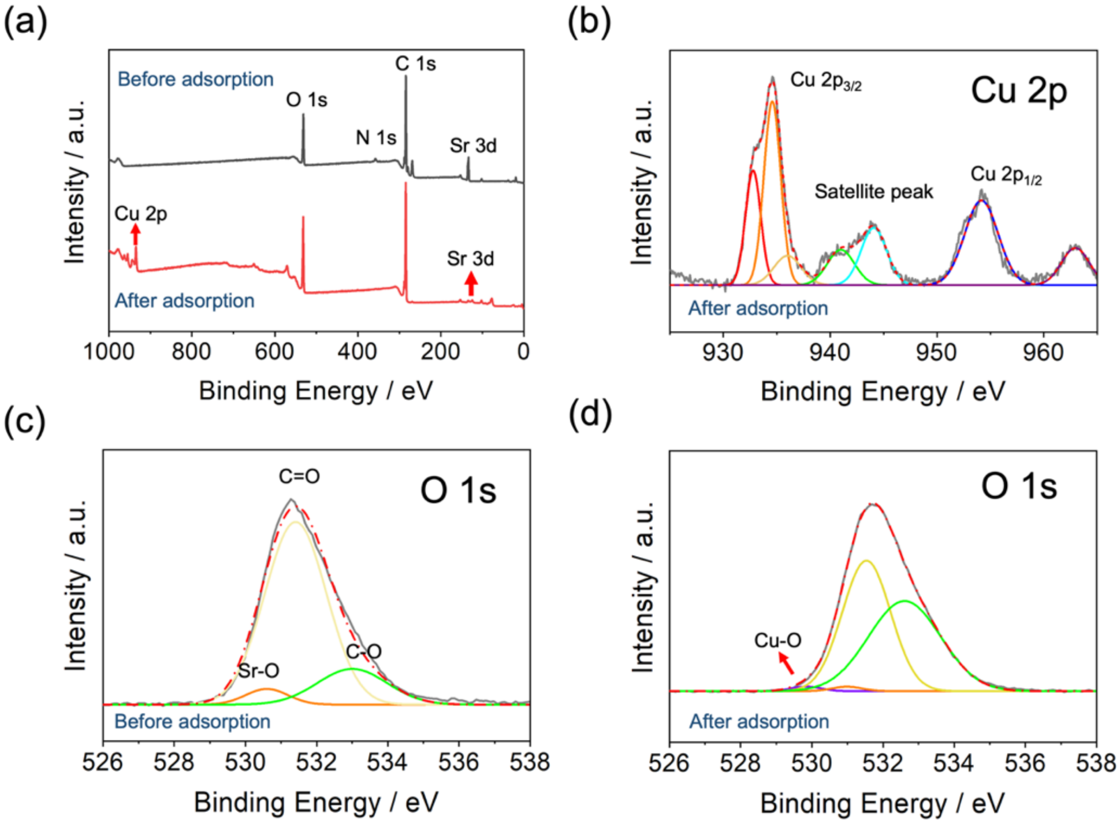

Figure. 3. XPS spectra of ^{NDC}MOF(Sr): (a) Broad scan spectra of ^{NDC}MOF(Sr) and Cu^{2+}@^{NDC}MOF(Sr). (b) Cu 2p spectrum of Cu^{2+}@^{NDC}MOF(Sr). O 1s spectra of ^{NDC}MOF(Sr) (c) before and (d) after the adsorption of Cu^{2+}. Dashed and full lines represent the raw intensity data and the deconvolution fitting intensities, respectively.

3.5 Thermogravimetric analysis (TGA) and stability tests

TGA was used to characterize the as-synthesized and Cu^{2+}-loaded MOFs as shown in Figure 4. The TGA profiles of the as-synthesized MOFs showed that ^{NDC}MOF(Ca) and ^{NDC}MOF(Sr) first experienced a weight loss before 270 °C and 230 °C, respectively, due to the loss of water and DMF solvent molecules. The typical weight loss in ^{NDC}MOF(Ca) and ^{NDC}MOF(Sr) was determined to be 84.48 wt.% (starting at 270 °C) and 86.6 wt.% (starting at 230 °C), respectively, which was attributed to the removal of the organic linkers and structural decomposition. While the as-synthesized MOFs were found to show moderate heat stability, the TGA profiles of the Cu^{2+}-loaded MOFs (Figure 4) revealed that the loaded MOFs would start to decompose at a much lower temperature of about 200 °C. PXRD studies (Section 3.2) of the Cu^{2+}-loaded MOFs also revealed structural changes in the MOFs upon the adsorption of Cu^{2+} (Figure. S1), suggesting the relatively low stability of the framework structures. Attempts have been made to recycle the MOFs by soaking the Cu^{2+}-loaded MOFs in methanol but it was found that Cu^{2+} could not be readily desorbed.

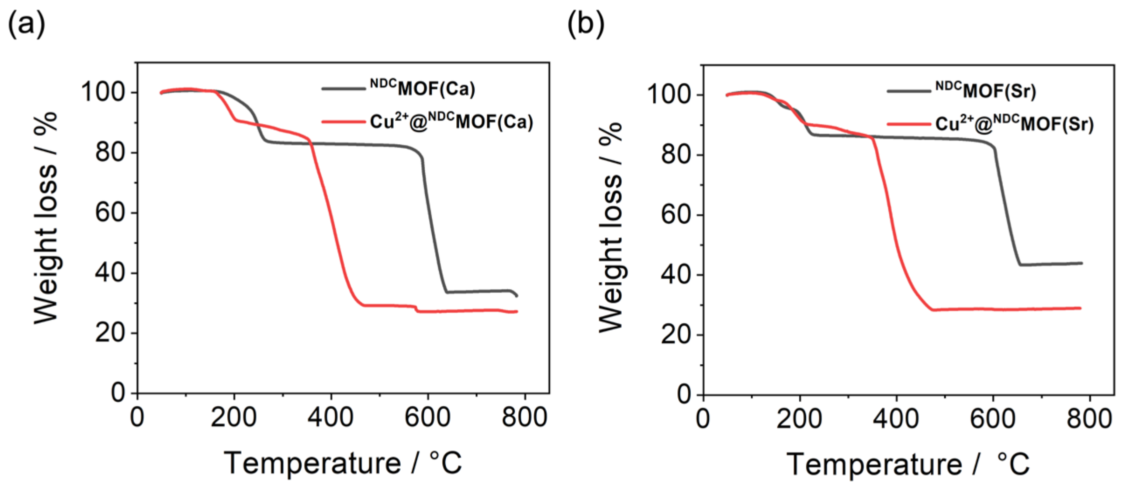

Figure 4. TGA profiles of as-synthesized and Cu^{2+}-loaded (a) ^{NDC}MOF(Ca) and (b) ^{NDC}MOF(Sr).

3.6 Brunauer–Emmett–Teller (BET) analysis

The nitrogen (N_2) sorption isotherms for both ^{NDC}MOF(Ca) and ^{NDC}MOF(Sr) at 77 K before and after the adsorption of Cu^{2+} were determined by the BET method as shown in Figure. S3. Results from the N_2 sorption experiments with ^{NDC}MOF(Ca) and ^{NDC}MOF(Sr) gave rise to pseudo-type II isotherms with type H3 hysteresis loops at the higher P/P_o region beyond 0.87 (Sing et al., 2004). While a typical Type II isotherm would reveal the occurrence of monolayer-multilayer adsorption, the pseudo-type II character of the isotherms for ^{NDC}MOF(Ca) and ^{NDC}MOF(Sr) suggested that the adsorbed multilayer, which was formed after complete monolayer coverage, would be metastable (Sing et al., 2004). This was probably due to the structural non-rigidity of the MOFs (Sing et al., 2004), as shown by the aforementioned changes in their PXRD patterns after adsorption (Figure. S3). On the basis of the analysis of adsorption models to be discussed in Section 3.8, it was plausible that the Langmuir model and hence monolayer adsorption played a dominant role in the adsorption of Cu^{2+} ions.

After the adsorption of Cu^{2+}, BET analysis showed a similar pseudo-type II isotherm. On the other hand, a reversible type II isotherm was observed for Cu^{2+}@^{NDC}MOF(Sr). This indicated that the pores of ^{NDC}MOF(Sr) were almost completely blocked after the adsorption of Cu^{2+} to give a non-porous structure (Sing et al., 1985). The BET surface area was determined to be 13.38 m^2 g^{-1} for ^{NDC}MOF(Ca) and 9.05 m^2 g^{-1} for ^{NDC}MOF(Sr), respectively.

3.7 Scanning electron microscopy (SEM)

The morphologies of the MOFs were characterized by SEM. The SEM images of as-synthesized and Cu^{2+}-loaded ^{NDC}MOF(Sr) are shown in Figure 5, whereas those for ^{NDC}MOF(Ca) are shown in Figure S4. Both MOFs showed a homogeneous distribution of rod- to plate-like structures. The surface morphologies of both MOFs became relatively rough after the adsorption of Cu^{2+}, but the overall rod- to plate-like morphologies were preserved, as in the as-synthesized MOFs.

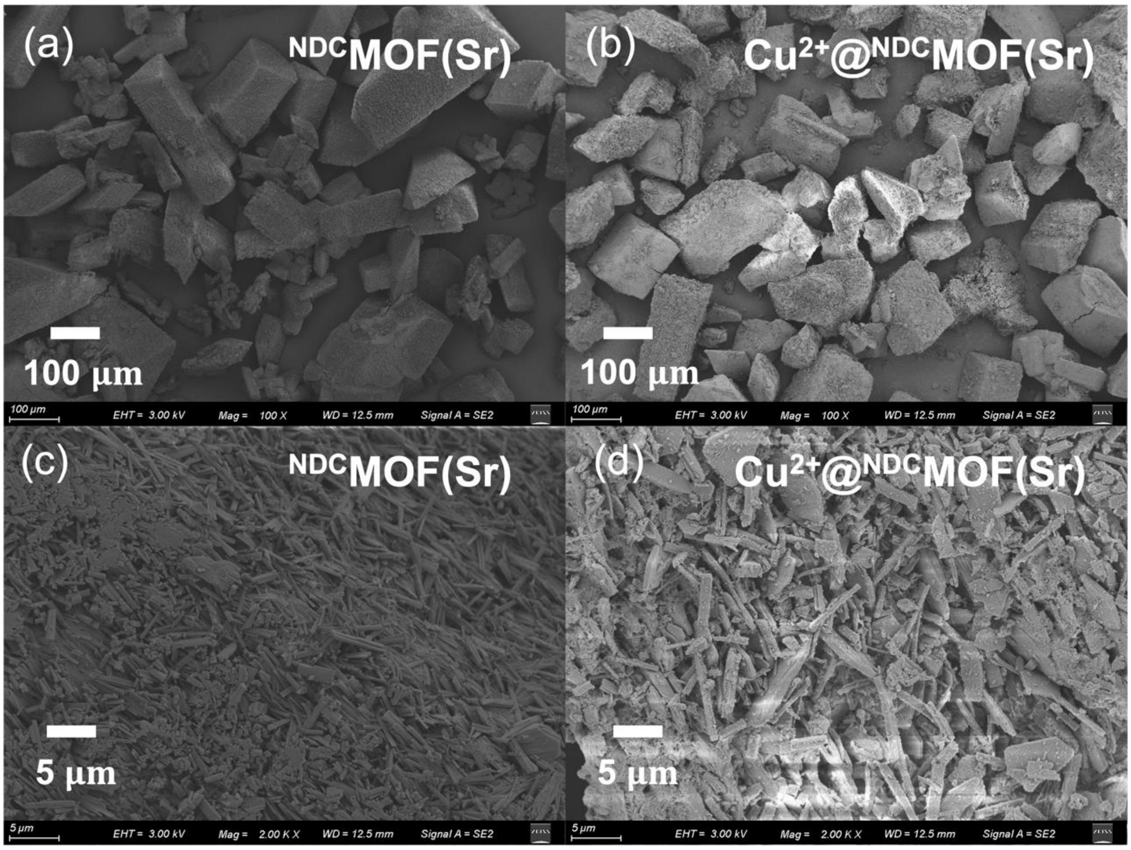

Figure 5. SEM images of (a,c) ^{NDC}MOF(Sr) and (b,d) Cu^{2+}@^{NDC}MOF(Sr) at different magnifications.

3.8 Adsorption kinetics

Activated crystalline powder samples of ^{NDC}MOF(Ca) and ^{NDC}MOF(Sr) have been utilized in the remediation of Cu^{2+} ions, and it was observed that the adsorption of Cu^{2+} occurred instantaneously when the MOFs were soaked into an aqueous solution of copper(II) nitrate. The adsorption process was monitored by UV-vis absorption studies. The linear relationship between the concentration of Cu^{2+} and the absorption intensity at 806 nm is shown in Figure S5. Crystalline powder samples of ^{NDC}MOF(Ca) (100 mg) and ^{NDC}MOF(Sr) (100 mg) were respectively suspended in an aqueous solution of Cu^{2+} (3995 mg L^{-1}) and allowed to stand in the dark at room temperature. At predetermined time intervals, a sample (2.5 mL) was extracted from the suspension and centrifuged to obtain a clear supernatant solution. The concentration of Cu^{2+} in the supernatant was determined from the absorbance based on UV-vis absorption measurements, as shown in Figure 6a and b. The adsorption of Cu^{2+} by ^{NDC}MOF(Ca) and ^{NDC}MOF(Sr) was accompanied by a change in the color of the supernatant solution from blue to colorless, as shown in the inset of Figure. 6c. Both systems reached equilibrium after about 500 minutes. ^{NDC}MOF(Sr) was observed to remove a higher percentage of copper ions of around 93%, while the removal percentage for ^{NDC}MOF(Ca) was about 87%.

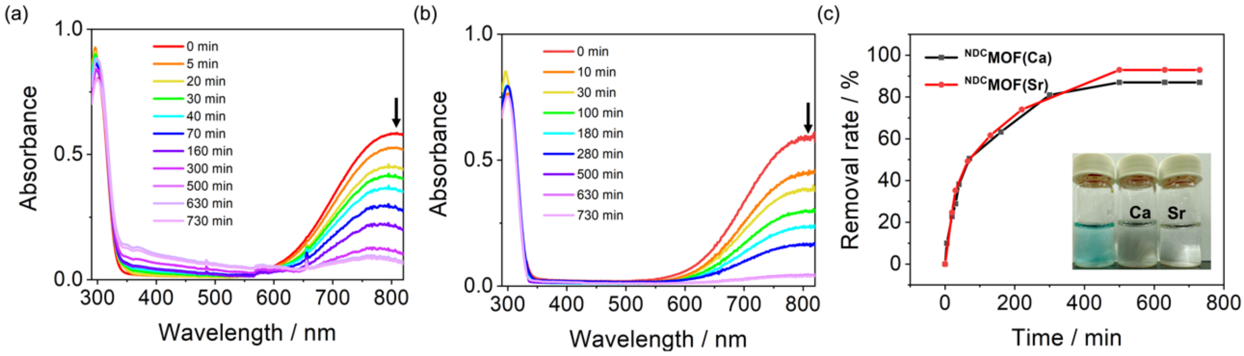

Figure. 6. Changes in the UV-vis absorption spectra of the supernatant solution at different times for (a) ^{NDC}MOF(Ca) and (b) ^{NDC}MOF(Sr). (c) Changes in the removal rate of Cu^{2+} from solution with respect to time for ^{NDC}MOF(Ca) and ^{NDC}MOF(Sr). The inset shows (left) the initial color of the Cu^{2+} solution and the appearance of the supernatant solution after 500 min in the presence of (middle) ^{NDC}MOF(Ca) and (right) ^{NDC}MOF(Sr).

The adsorption capacity (q_t, mg g^{-1}) and Cu^{2+} removal rate (%) were calculated by Equations (1) and (2) (Hameed et al., 2007), respectively.

$$q_t = (C_o - C_t)V/m \ (1)$$

$$Removal\ rate = [(C_o - C_t)/C_o] \times 100\% \ (2)$$

where C_o (mg L^{-1}) is the initial concentration of the aqueous Cu^{2+} solution, C_t (mg L^{-1}) is the equilibrium concentration of Cu^{2+} at time t, V (L) is the volume of the aqueous Cu^{2+} solution, and m is the mass of the MOF added. Based on equation (1), the experimental adsorption capacity of Cu^{2+} by ^{NDC}MOF(Ca) was found to be 347.5 mg g^{-1}, while that by ^{NDC}MOF(Sr) was found to be 371.5 mg g^{-1} at 500 min when equilibrium was reached.

The adsorption rate is one of the key aspects regarding the performance of adsorption. The pseudo-first order (Figure 7a) and pseudo-second-order (Figure 7b) models have been used to study the kinetics of the Cu^{2+} adsorption process, and the respective parameters are presented in Table 1.

The equations for the pseudo-first order and the pseudo-second order models are expressed by Equations (3) and (4) (Hameed et al., 2007), respectively.

$$\ln(q_e - q_t) = ln q_e - K_1 t \ (3)$$

$$t/q_t \ = 1/(K_2 q_e^2) + t/q_e \ (4)$$

where q_e and q_t are the adsorption capacities (mg g^{-1}) at equilibrium and time t, respectively. K_1 (min^{-1}) is the rate constant of the pseudo-first-order model, whereas K_2 (g mg^{-1} min^{-1}) is the rate constant of the pseudo-second-order model.

According to the pseudo-first-order kinetic model, the calculated q_e values of ^{NDC}MOF(Ca) and ^{NDC}MOF(Sr) were 1227 and 961.6 mg g^{-1}, respectively, which were inconsistent with the experimental values. The pseudo-first order plot (Figure. 7a) also deviated from linearity. In the pseudo-second-order kinetic model, when t/q_t was plotted against t, a linear plot was obtained for the adsorption of Cu^{2+} (Figure 7b), suggesting that the adsorption process followed pseudo-second-order kinetics.

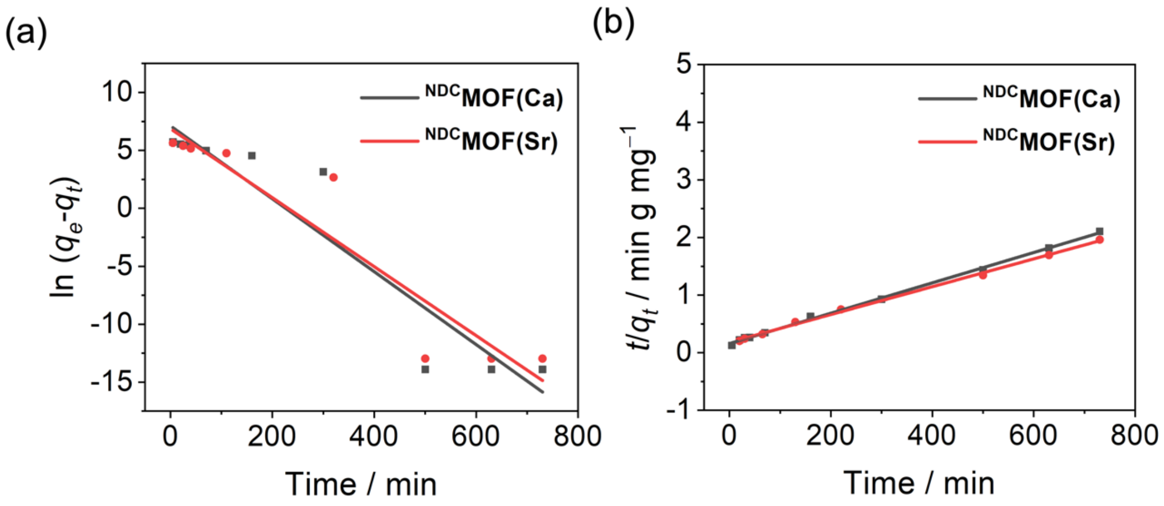

Figure 7. (a) Pseudo-first-order kinetic model for the adsorption of Cu^{2+} by ^{NDC}MOF(Ca) and ^{NDC}MOF(Sr). (b) Pseudo-second-order kinetic model for the adsorption of Cu^{2+} by ^{NDC}MOF(Ca) and ^{NDC}MOF(Sr).

Table 1. Adsorption kinetic constants for the adsorption of Cu^{2+} by ^{NDC}MOF(Ca) and ^{NDC}MOF(Sr).

Adsorbent	^{NDC}MOF(Ca)	^{NDC}MOF(Sr)
	Pseudo-first-order kinetic model	
q_e (mg g^{-1})	1227	961.6
K_1 (min^{-1})	7.11	6.87
R^2	0.9036	0.8972
	Pseudo-second-order kinetic model	
q_e (mg g^{-1})	380.2	414.9
K_2 (g mg^{-1} min^{-1})	4.35×10^{-5}	3.23×10^{-5}
R^2	0.9984	0.9981

3.9 Adsorption isotherm

In order to study the relationship between the initial concentration of Cu^{2+} and the adsorption capacity, aqueous solutions of Cu^{2+} (10 mL) with different concentrations (255–2245 mg L^{-1}) were prepared. To each of these solutions, either ^{NDC}MOF(Ca) (3 mg) or ^{NDC}MOF(Sr) (3 mg) was added. The UV-vis absorption spectra of the supernatant solution were measured after 24 hours. The variation of the absorption intensity at 806 nm was measured to determine the equilibrium concentration (C_e) of Cu^{2+} in the solution.

The Langmuir and Freundlich models have been used to analyze the data and investigate the adsorption properties of the MOFs. The Langmuir isotherm model assumes that adsorption is confined to a single layer. In this case, the energy of adsorption is the same for all sites and is independent of the degree of surface coverage. The adsorption to one site is independent of the occupancy conditions of neighboring sites and there is no interaction between neighboring adsorbed molecules (Kalam et al., 2021). The Langmuir adsorption model (Saadi et al., 2015) is expressed as:

$$C_e/q_e = C_e/q_{max} + 1/(q_{max}K_L) \quad (5)$$

where q_e (mg g^{-1}) is the amount of Cu^{2+} adsorbed at the equilibrium concentration, C_e (mg L^{-1}). $q_{\max}$ represents the maximum adsorption capacity of the adsorbent and K_L (L mg^{-1}) is the Langmuir constant.

On the other hand, the Freundlich model assumes that the adsorption process takes place on the surface of a heterogeneous adsorbent and can be applied to multilayer adsorption (Zhao et al., 2020). The Freundlich adsorption model (Mustapha et al., 2019) is expressed as:

$$lnq_e = \ln k_F + \ 1/n\ (lnC_e) \quad (6)$$

where q_e (mg g^{-1}) indicates the equilibrium adsorption capacity, C_e (mg L^{-1}) is the equilibrium concentration of Cu^{2+} in the solution. n and K_F are the Freundlich constants which represent the adsorption capacity and adsorption intensity, respectively.

Based on the Langmuir and Freundlich adsorption models, the fitting curves for the adsorption of Cu^{2+} by ^{NDC}MOF(Ca) and ^{NDC}MOF(Sr) at 298 K could be plotted as shown in Figure 8a and b. The adsorption isotherm constants could be obtained according to equations (5) and (6), and they are listed in Table 2. It could be observed that the R^2 values for the adsorption of Cu^{2+} by both MOFs were closer to unity (0.9993 for ^{NDC}MOF(Ca) and 0.9988 for ^{NDC}MOF(Sr)) according to the Langmuir model. Such higher coefficients of determination suggested that the Langmuir model would be a more appropriate description of the adsorption process, which was homogeneous and confined to a monolayer (Margariti et al., 2017). The maximum adsorption capacity for Cu^{2+} ($q_{\max}$) could thus be estimated from the reciprocal of the slopes of the Langmuir fitting curves, which were 299.4 and 398.4 mg g^{-1}, respectively, for ^{NDC}MOF(Ca) and ^{NDC}MOF(Sr).

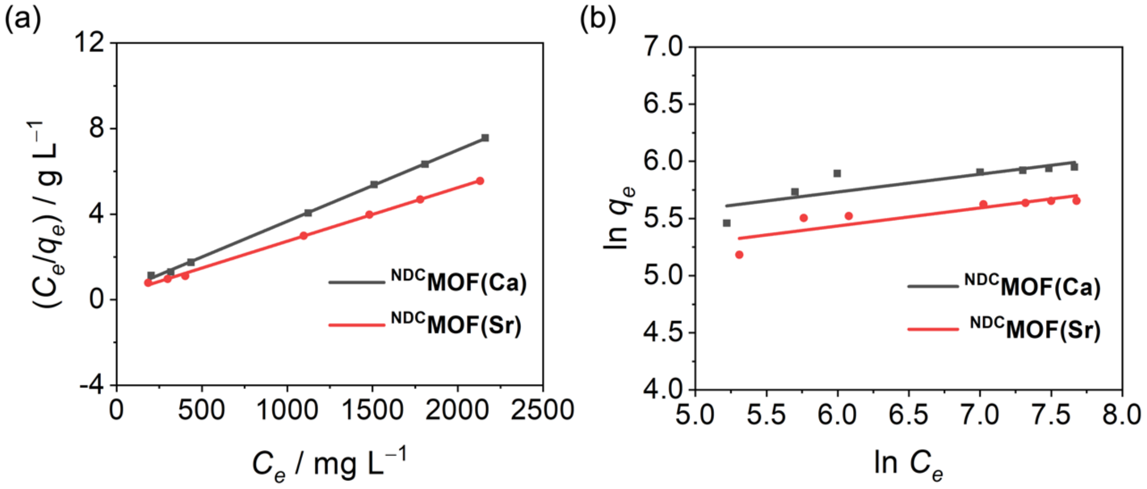

Figure 8. Fitting curves of the (a) Langmuir and (b) Freundlich adsorption isotherm models for the adsorption of Cu^{2+} by ^{NDC}MOF(Ca) and ^{NDC}MOF(Sr).

Table 2. Adsorption isotherm constants for the adsorption of Cu^{2+} by ^{NDC}MOF(Ca) and ^{NDC}MOF(Sr).

Adsorbent	^{NDC}MOF(Ca)	^{NDC}MOF(Sr)
Langmuir model		
$q_{\max}$ (mg g^{-1})	299.4	398.4
K_L (mg^{-1})	0.01021	0.01139
R^2	0.9993	0.9988
Freundlich model		
K_F (mg g^{-1})	121.0	89.00
n	6.414	6.342
R^2	0.8468	0.8733

Table 3. Maximum adsorption capacities of various adsorbents for Cu^{2+} in the literature.

Adsorbent	Maximum adsorption capacity (mg g^{-1})	Reference

$[Ca(H_4L)(DMA)_2]\cdot 2DMA$	67.4	Margarriti et al., 2017
WSA/starch/Fe_3O_4	45.4	Foroutan et al., 2022
Modified activated carbon	84.51	Chen et al., 2022
MOF-5	290	Bakhtiari et al., 2015
EDPMTA-Zr	110.4	Guo et al., 2019
Zn(Bim)(OAc)	335.57	Xu et al., 2020
Xylan/Graphene Oxide Composite Hydrogel	228	Sun et al., 2022
Ni/Fe-LDH-SA	192.6	Long et al., 2022
Zeolite NaX	95.29	Liang e al., 2022
Organosilica hybrid	153	Santhamoorthy et al., 2022
N-methylene phosphonic acid chitosan	276.12	Liu et al., 2021
Graphene oxide	179.32	Zhang et al., 2023
IRMOF-3/GO	254.14	Rao et al., 2017
Zr-MOF	125	Subramaniyam et al., 2022
pz-UiO-66	247	Shao et al., 2023
$[(Zn_3L_3(H_2O)_6][(Na)(NO_3)]$	379.13	Yu et al., 2018

^{NDC}MOF(Ca)	299.4	This work
^{NDC}MOF(Sr)	398.4	This work

The values obtained were compared with those of various adsorbents for Cu^{2+} (Table 3). It was observed that the adsorption performance of ^{NDC}MOF(Ca) and ^{NDC}MOF(Sr) was comparable to the reported materials, with ^{NDC}MOF(Sr) showing the highest adsorption capacity which outperformed related MOFs. This suggests that ^{NDC}MOF(Ca) and ^{NDC}MOF(Sr) are promising candidates for the adsorptive removal of Cu^{2+}.

3.10 Effect of co-existing ions

The presence of other ions such as Na^{+} and Mg^{2+} is inevitable in wastewater. To estimate the potential of ^{NDC}MOF(Ca) and ^{NDC}MOF(Sr) in practical applications, Na^{+} and Mg^{2+} were introduced as co-existing ions to assess the adsorption performance of the MOFs for Cu^{2+} (Figure 9). The q_e of both ^{NDC}MOF(Ca) and ^{NDC}MOF(Sr) initially increased when the Na^{+} concentration was increased from 0 to 4000 mg L^{-1} and when the Mg^{2+} concentration was increased from 0 to 2000 mg L^{-1}. When the salinity was further increased to 8000 mg L^{-1} for either Na^{+} or Mg^{2+}, q_e was found to decrease for both ^{NDC}MOF(Ca) and ^{NDC}MOF(Sr). In the initial stage when the adsorption amount increased with increasing salinity, it was probable that the adsorption process was dominated by an innersphere adsorption mechanism (Goldberg et al., 2005), during which the polar water molecules in the first hydrated shells of the $[Cu(H_2O)_6]^{2+}$ complex ions would interact with the MOF surface groups. When the concentration of Na^{+} or Mg^{2+} ions was further increased, the adsorption would be dominated by electrostatic interactions (Chen et al., 2012). Moreover, the increasing salinity would cause more counterions to gather at the adsorption sites and weaken the affinity of the MOFs towards Cu^{2+}. The competitive adsorption between Cu^{2+} and the co-existing ions would also increase, leading to an overall reduction in the adsorption capacity for Cu^{2+} ions (Chen et al., 2012).

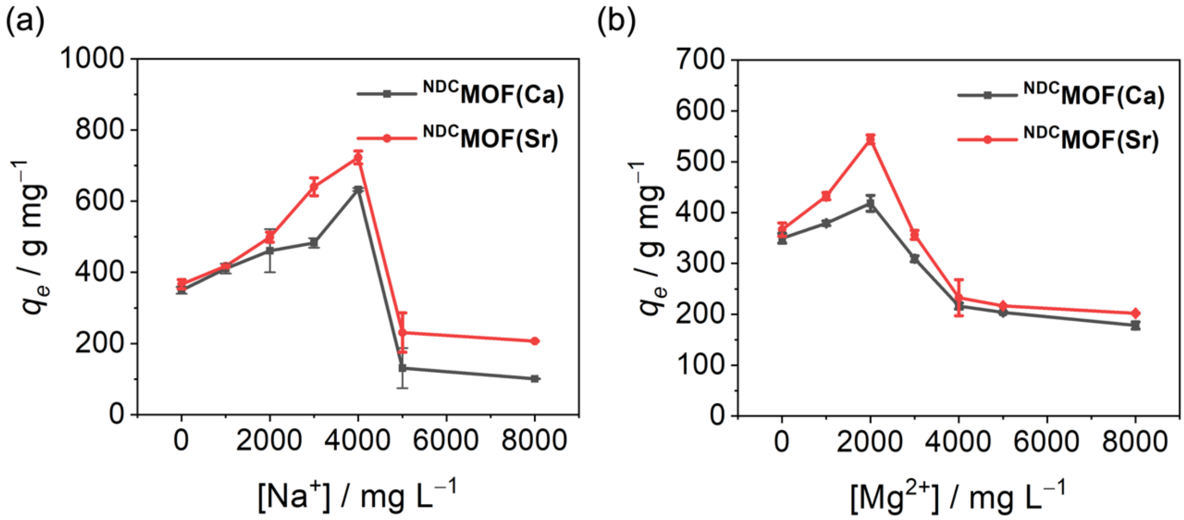

Figure 9. Effects of co-existing ions on the adsorption of Cu^{2+} by ^{NDC}MOF(Ca) and ^{NDC}MOF(Sr).

3.11 Emission quenching

The solid-state emission spectra of the as-synthesized and Cu^{2+}-loaded MOFs at room temperature have been measured to study their luminescence sensing properties. Upon photoexcitation at 330 nm, ^{NDC}MOF(Ca) (Figure S6) and ^{NDC}MOF(Sr) (Figure 10) showed a broad emission band which peaked at 453 and 435 nm, respectively. By comparing with the emission spectrum of the NDC ligand (Figure S7) which showed an emission maximum at 458 nm, the emission in the MOFs was tentatively assigned to an intraligand origin. On the other hand, both MOFs adsorbed Cu^{2+} to give loaded MOFs with deep blue color. At the same time, the blue emission of the as-synthesized MOFs was readily quenched upon the adsorption of Cu^{2+}. The representative emission changes in the presence ^{NDC}MOF(Sr) are shown in Figure 10. Attempts have been made to conduct the emission quenching experiments at different initial concentrations of Cu^{2+} (Figure S8). It was observed that the emission quenching was essentially an “on/off” phenomenon in which the emission of the MOFs would be instantaneously and completely quenched in the presence of a trace amount of Cu^{2+} ions with an initial concentration as low as 50 mg L^{-1}. Thus, in addition to adsorptive removal, ^{NDC}MOF(Ca) and ^{NDC}MOF(Sr) could be used as an efficient sensor for the detection of trace amounts of Cu^{2+} in the aqueous environment.

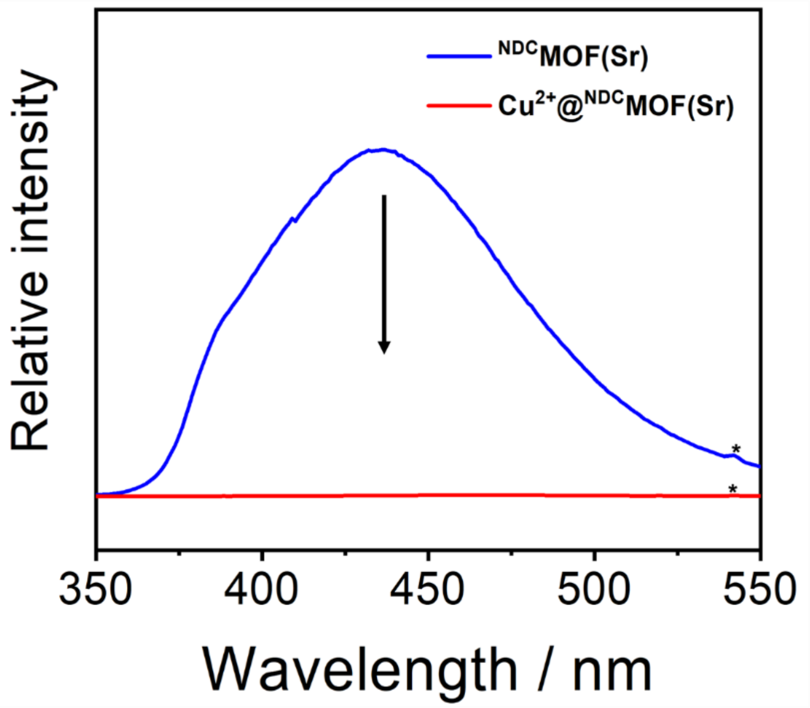

Figure 10. Solid-state emission spectrum of ^{NDC}MOF(Sr) and Cu^{2+}@^{NDC}MOF(Sr) at 298 K (asterisks indicate instrumental artifacts). λ_{ex} = 330 nm.

4. Conclusion

In conclusion, a series of alkaline earth metal-based MOFs has been synthesized, characterized and employed for the adsorptive removal of Cu^{2+} ions. Both MOFs were found to exhibit high adsorption capacities of 299.4 and 398.4 mg g^{-1}, respectively, for Cu^{2+} in aqueous media. The performance of ^{NDC}MOF(Sr), in particular, was observed to surpass related MOFs and common adsorbents. Furthermore, the MOFs were found to exhibit blue emission upon photoexcitation by UV light, and this emission would be readily quenched after the adsorption of Cu^{2+} ions. In addition to adsorptive removal, the obvious color and emission changes have rendered these MOFs good candidates for the visual detection of Cu^{2+} in water, thus providing new insights for the remediation of heavy metal ions and other water pollutants in the environment.

5. Supplementary Data of article 1

Table S1. Selected crystallographic data and structural refinement summary for as-synthesized ^{NDC}MOF(Ca).

	^{NDC}MOF(Ca)
Crystal system	Orthorhombic
Space group	*Pnma*
a / Å	6.906(10)
b / Å	21.00(3)
c / Å	9.941(13)
V / Å^3	1442(3)
Z	4
Density (calcd) / g cm^{-3}	1.508
μ / mm^{-1}	0.46
Radiation type	Mo K$_\alpha$
Radiation wavelength / Å	0.71073
Temperature / K	200
F (000)	680
Restrained goodness-of-fit	1.287
Reflections collected	5648
Independent reflections	1590
R_1 [$F^2 > 2\sigma(F^2)$]	0.1290
wR_2 [F^2]	0.1582

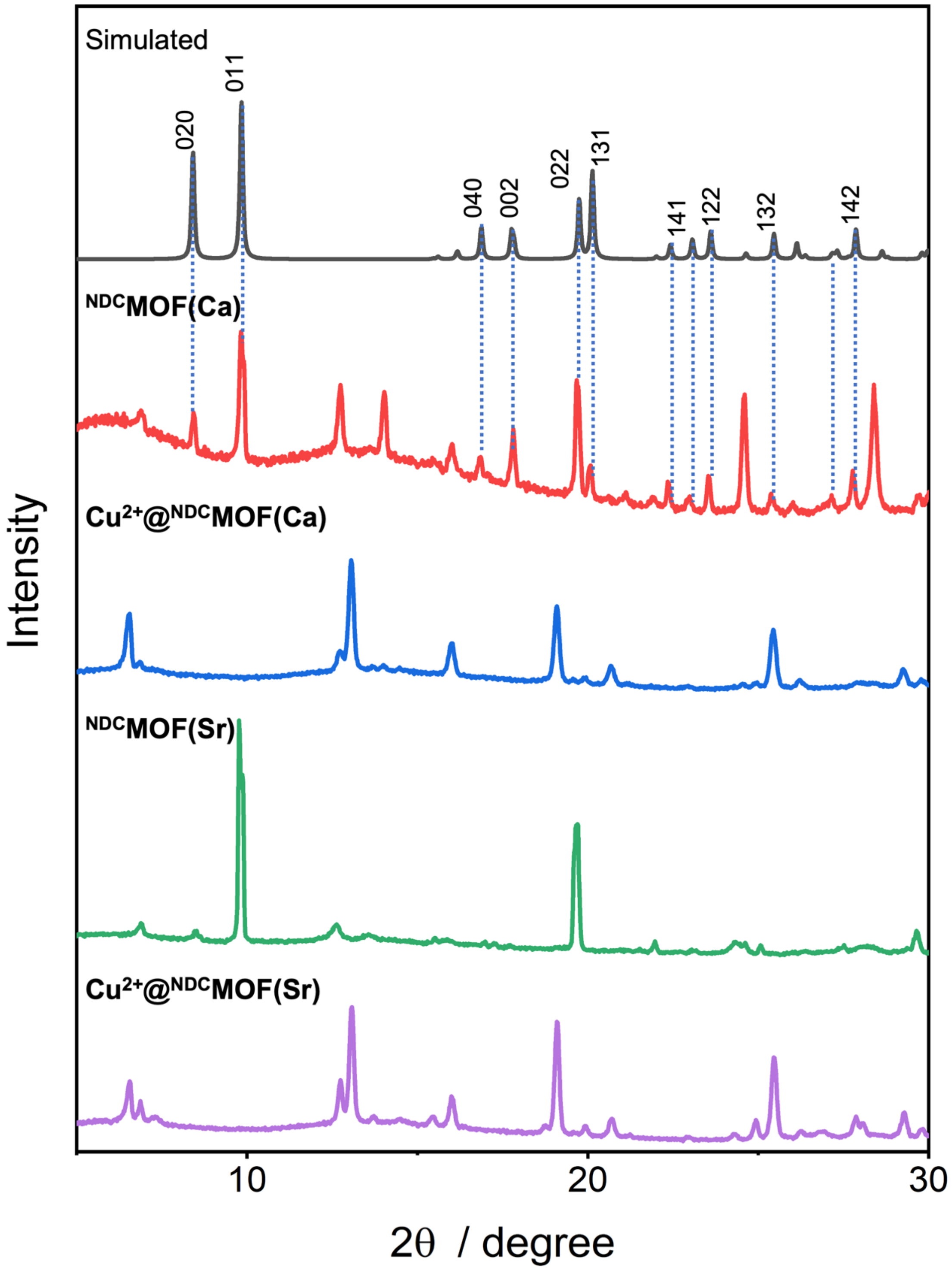

Figure S1. The simulated PXRD patterns of ^{NDC}MOF(Ca) and the experimental powder X-ray diffraction patterns of as-synthesized and Cu^{2+}-loaded (a) ^{NDC}MOF(Ca) and (b) ^{NDC}MOF(Sr).

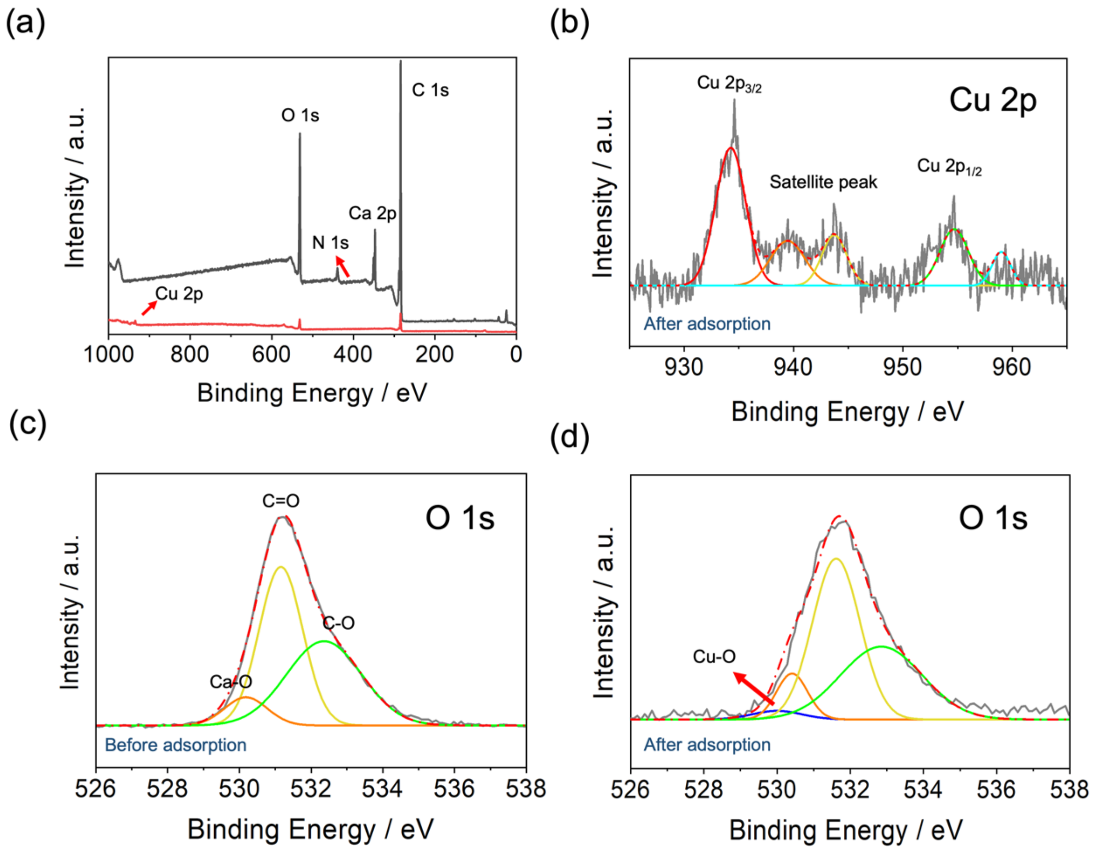

Figure S2. X-ray photoelectron spectroscopic (XPS) spectra of ^{NDC}MOF(Ca). (a) Broad scan spectra of ^{NDC}MOF(Ca) (black line) and Cu^{2+}@^{NDC}MOF(Ca) (red line). (b) Cu 2p spectrum of Cu^{2+}@^{NDC}MOF(Ca). O 1s spectra of ^{NDC}MOF(Ca) (c) before and (d) after the adsorption of Cu^{2+}. Dashed and full lines represent the raw intensity data and the deconvolution fitting intensities, respectively.

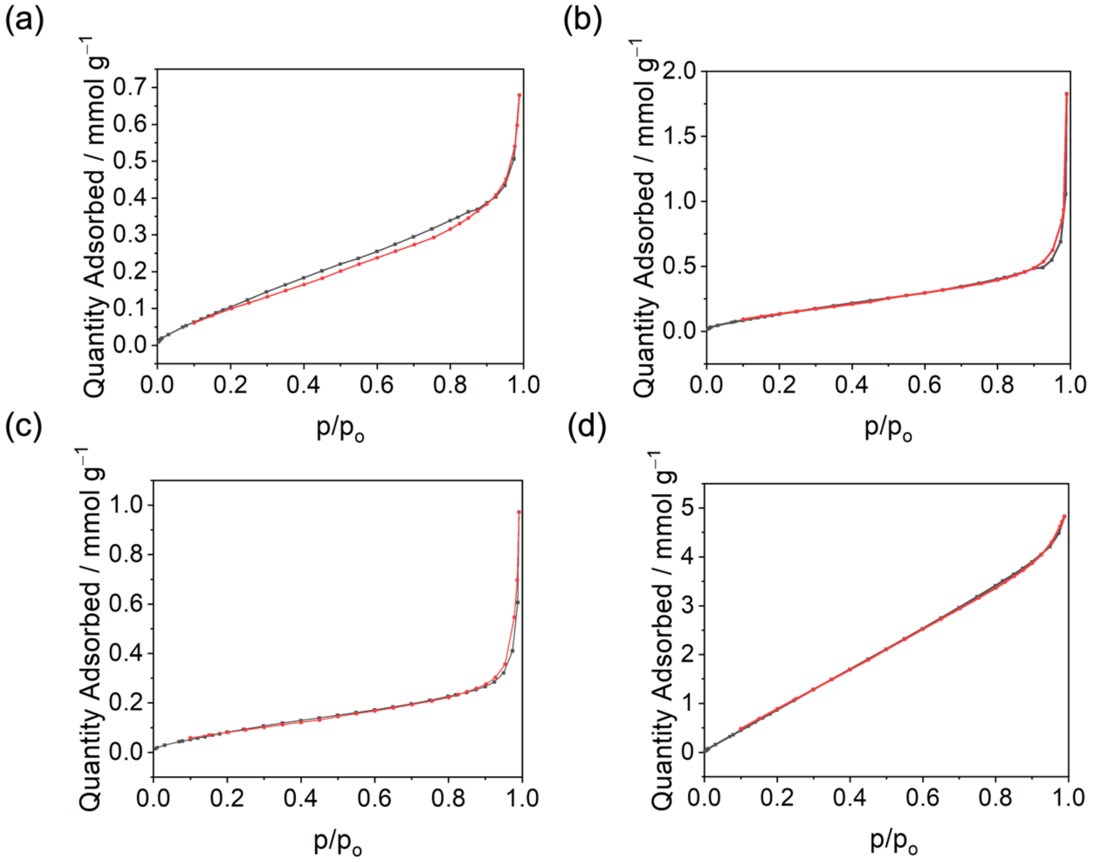

Figure S3. Nitrogen sorption isotherms of (a) ^{NDC}MOF(Ca), (b) Cu^{2+}@^{NDC}MOF(Ca), (c) ^{NDC}MOF(Sr) and (d) Cu^{2+}@^{NDC}MOF(Sr) at 77 K. Black and red lines represent adsorption and desorption branches, respectively.

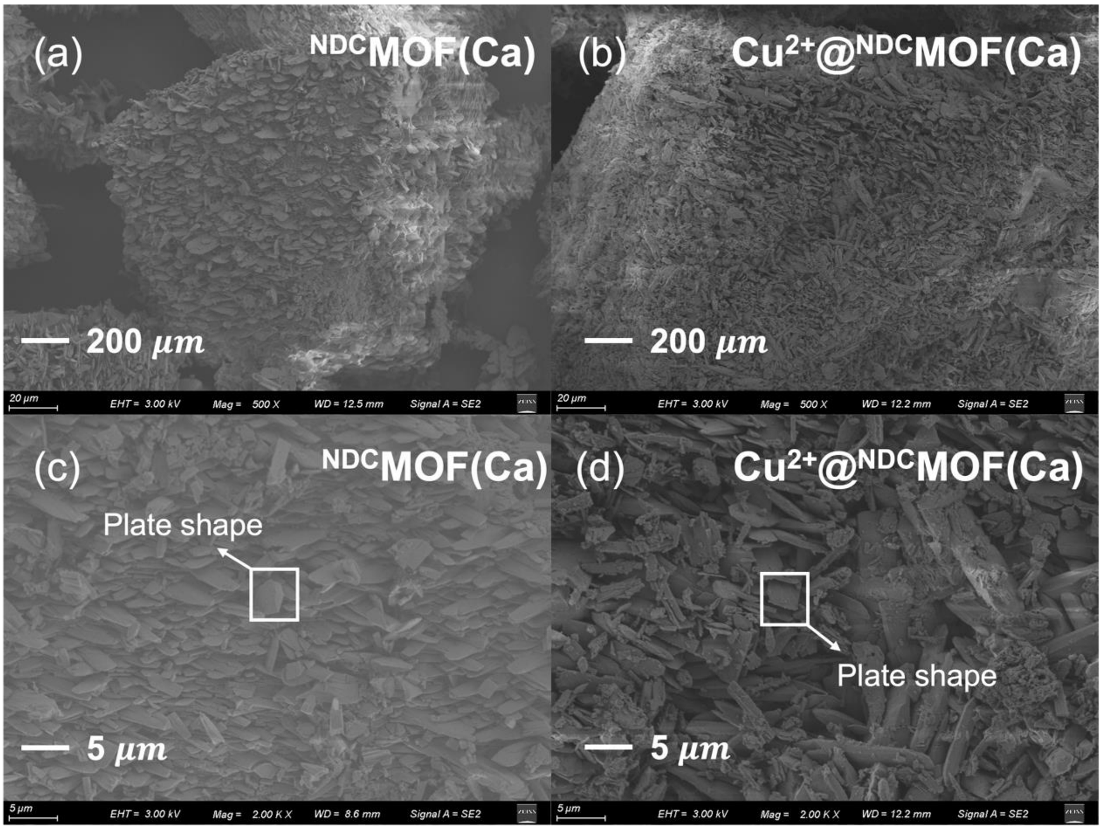

Figure S4. The SEM images of (a) ^{NDC}MOF(Ca) and (b) Cu^{2+}@^{NDC}MOF(Ca). (c) the enlarged images of ^{NDC}MOF(Ca). (d) the enlarged images of Cu^{2+}@^{NDC}MOF(Ca).

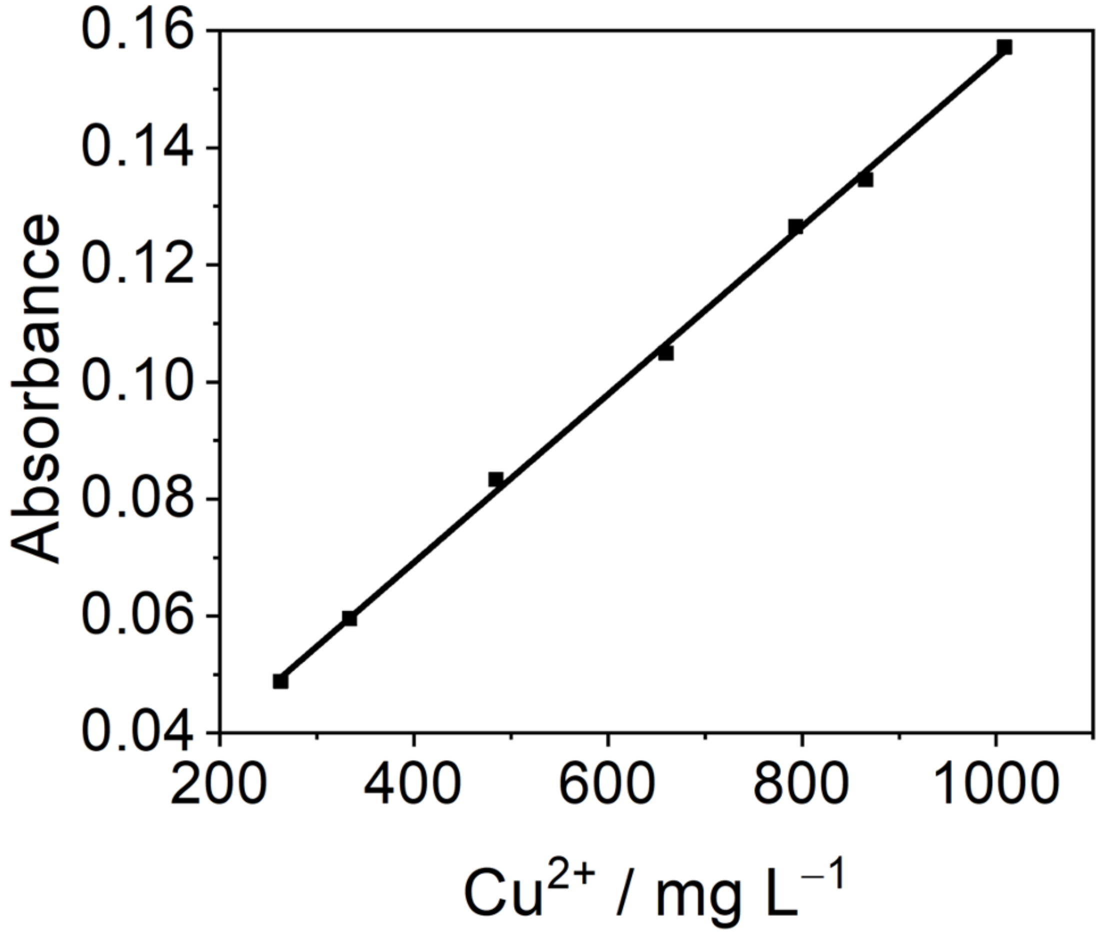

Figure S5. Cu^{2+} ions concentration (mg L^{-1}) against the UV-vis absorbance intensity (R^2 = 0.99893).

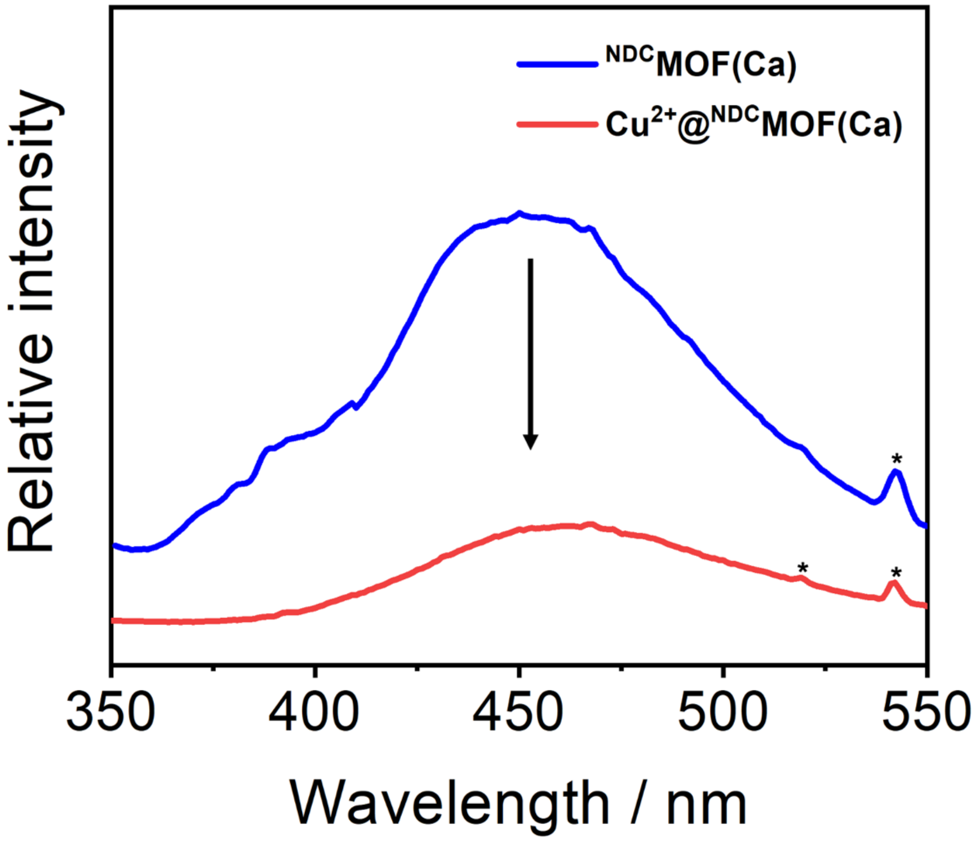

Figure. S6. Solid-state fluorescence spectrum of ^{NDC}MOF(Ca) and Cu^{2+}@^{NDC}MOF(Ca) at 298 K (asterisks indicate instrumental artifacts). λ_{ex} = 330 nm.

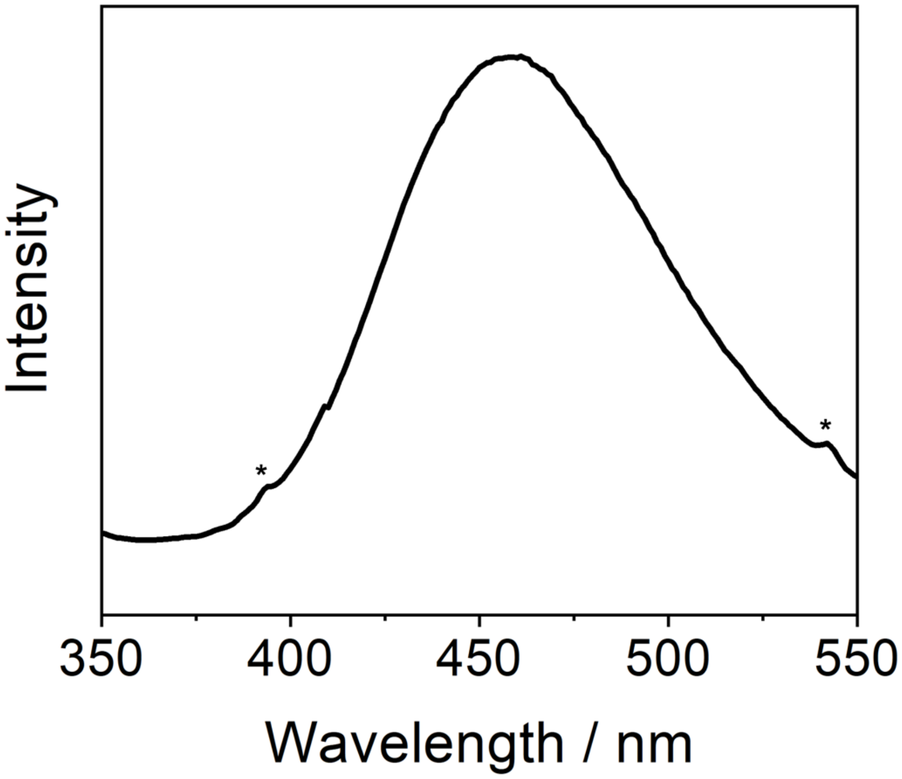

Figure S7. Solid-state fluorescence spectrum of NDC at 298 K (asterisk indicates instrumental artifacts). λ_{ex} = 330 nm.

Chapter 3 Paper 2-Efficient removal of piroxicam and ketoprofen by acid-modulated iron(III) metal-organic frameworks

Chen Wu[a,b], Vonika Ka-Man Au[a,b,]*

Abstract

Pharmaceutical substances such as piroxicam and ketoprofen have been detected in worldwide water sources, posing an emerging risk to environmental health. Therefore, developing a low-energy and efficient method to remove these pollutants from the environment is necessary. Herein, the adsorption of piroxicam and ketoprofen from water has been investigated by using a series of modulated metal organic frameworks, namely MIL-126 synthesized in the presence of various amounts of acetic acid. The material synthesized with 1 equivalent of the acid modulator, MIL-126-1AA, has been found to show impressive adsorption activities, irrespective of its lower surface area than the other MOF samples studied. MIL-126-1AA exhibits maximum adsorption capacities of 209.65 mg g^{-1} for piroxicam and 452.49 mg g^{-1} for ketoprofen, respectively. Such high adsorption capacities can be attributed to the permanent porosity of MIL-126, an optimal amount of defects in the modulated MOFs, as well as a delicate balance of hydrogen bonding and non-covalent interactions between the MOFs and the adsorbates, as revealed from the adsorption studies and X-ray photoelectron spectroscopic analysis. Additionally, the durability of the adsorbents allows them to be reusable after multiple cycles without significant decrease in the adsorptive performance, further highlighting their potentials for the remediation of pharmaceuticals and other organic pollutants from the aqueous environment.

Keywords

Metal-organic framework, modulated synthesis, adsorption, ketoprofen, piroxicam

1.Introduction

There has been increasing attention to the occurrence of pharmaceuticals and personal care products (PPCPs) in the environment in recent years. In particular, the extensive use of non-steroidal anti-inflammatory drugs (NSAIDs) has led to significant concerns regarding their increasing occurrence in the aqueous environment globally (Rastogi et al., 2021). For instance, the anti-inflammatory drugs piroxicam (PIR) and ketoprofen (KET) have already been detected in raw hospital wastewater and effluents from industries (Collado et al., 2014). Meanwhile, PIR is among the most consumed NSAIDs and has been used for nearly 30 years to treat chronic inflammatory diseases, fever symptoms, pain and rheumatic diseases, and is also used as a protective agent against various oxidants (Gutiérrez et al., 2019). However, the accumulation of PIR in the water environment has been found to promote the expansion of cyanobacterial populations by pushing eukaryotic algae back into the water systems (Aydin et al., 2013). KET is also widely used around the world because of its availability over the counter and at a relatively affordable price. It is commonly used to treat pain in muscles and joints, as well as conditions such as arthritis, gout, rheumatoid osteoarthritis and general inflammation (Georgin et al., 2022). As a result, these pharmaceutical substances are consumed in large quantities (tons per year) due to the high demand and have been detected in wastewater worldwide (Thelusmond et al., 2018). According to recent environmental risk assessments, human pharmaceuticals have been detected in soils, surface waters and effluents (Ferrari, et al., 2004 and Jin et al., 2020). Although these pollutants exist at low concentrations in the natural environment, they are difficult to be biodegraded and may lead to high environmental toxicity, causing negative impacts on ecosystems and human health.

For the removal of NSAIDs from water, common methods include biofiltration, advanced oxidation processes, membrane filtration and adsorption (Rastogi et al., 2021). Among these processes, adsorption represents a simple, energy-efficient and low-cost treatment with high removal efficiency for contaminants in aqueous systems (Bunmahotama et al., 2020). Clay, zeolite, activated carbon and aluminum phosphate are well-known porous adsorbents for the removal of water pollutants. However, the adsorption performance of these materials tends to be limited by the lack of tailor-made design to control their surface properties and functions (Ali, 2012). Metal-organic frameworks (MOFs), on the other hand, are modifiable crystalline materials consisting of metal nodes and organic ligands that are assembled via coordination bonds (Zhou, et al., 2012). The outstanding features such as adjustable and switchable pore size (Yaghi et al., 2003, Castellanos et al., 2016 and Zhang et al., 2022), huge surface area (Collins et al., 2007), high porosity (Ghasempour et al., 2021) and large pore volume (Kitagawa et al., 2022) make MOFs ideal for the adsorption and removal of pollutants (Lin et al., 2022; Wu et al., 2023 and Au et al., 2021). To obtain MOFs with desired homogeneity and properties, one way to control the synthetic process of MOFs is to use modulators. Novel or mixed phases of MOFs can also be generated by producing ordered defects such as missing linkers and/or nodes to the MOFs in the presence of modulators (Ma et al., 2022). Recent studies have also shown that the modulated synthesis of MOFs can be considered as an excellent strategy to obtain MOFs with enhanced porosity and more active sites (Dissegna et al., 2018), thus achieving higher adsorption efficiency.

Among various classes of MOFs, iron-based MOFs are non-toxic to the environment and highly stable under adsorption conditions (Govarthanan et al., 2021). In particular, the MIL (*Matériaux de l'Institut Lavoisier*) family of MOFs has been extensively studied due to the high tunability and structural diversity of these frameworks with trivalent metal centers (Dan-Hardi et al., 2012 and Kuznicki et al., 2021) While the MIL family has been used in gas separation (Zhang et al., 2012), sensing (Iacomi et al., 2022) and photocatalysts (Araya et al., 2017), the utilization of iron-based MIL-type MOFs for the adsorption of pharmaceutical substances from water remains relatively underexplored and is mainly limited to the use of

MIL-53 (Navarathna et al., 2020 and Xiong et al., 2018) and MIL-101 (Li etal., 2019 and Dong et al., 2020)

Herein, the use of a modulated iron(III) MOF, namely MIL-126 with biphenyl-4,4’-dicarboxylate as the linker, for the adsorptive removal of pharmaceuticals is reported. The iron(III) MOFs have been synthesized in the presence of acetic acid as a modulator to adjust the morphology and properties. The MIL-126 samples synthesized with different equivalents of the modulator have been characterized in detail, and utilized for the removal of PIR and KET from the aqueous environment. The kinetics and mechanism of the adsorption have also been investigated in detail.

2. Experimental

2.1 Chemicals

Iron(II) chloride tetrahydrate (97 %) and biphenyl-4,4’-dicarboxylic acid (H_2BPDC; 98 %) were purchased from J&K Scientific, whereas piroxicam was from Bidepharm. Dimethylformamide (DMF; 99.8 %), methanol (99.8 %) and dichloromethane (99.8 %) were purchased from TCI. All other reagents and solvents are commercially available and used as received.

2.2 Physical Measurements and Instrumentation

Powder X-ray diffraction (PXRD) data were collected on a Bruker D8 ADVANCE Powder X-ray Diffractometer in Bragg-Brentano (θ/2θ) reflection mode with graphite monochromatized Cu-Kα radiation. X-Ray photoelectron spectroscopy (XPS) was performed using a Thermo ESCALA 250Xi X-ray Photoelectron Spectrometer Microprobe. Fourier-transform infrared (FTIR) spectra were obtained on a PerkinElmer Frontier FTIR spectrometer (4000–530 cm^{-1}) with a universal attenuated total reflection (ATR) accessory. Brunauer-Emmett-Teller nitrogen adsorption–desorption isotherm tests were performed on a

Micromeritics 3Flex adsorption analyzer. Thermogravimetric analysis (TGA) was conducted on a PerkinElmer instruments Thermogravimetric Analyzer TGA 4000. Scanning electron microscopy (SEM) were performed on a Sigma 500 scanning electron microscope and energy-dispersive X-ray (EDX) spectroscopy was performed with a Bruker XFlash 6130 detector at 10 kV. Ultraviolet-visible (UV-vis) absorption spectra were obtained on an Agilent Technologies Cary 8454 UV-vis spectrophotometer. Zeta potentials were measured on a Zetasizer NANO ZS90, and the pH of the samples was measured by a FiveEasy F20 pH meter.

2.3 Modulated synthesis of MIL-126

The modulated MIL-126 samples were synthesized according to a modified literature procedure (Bara et al., 2019). Iron(II) chloride tetrahydrate (99.5 mg, 0.50 mmol) and biphenyl-4,4’-dicarboxylic acid (60.6 mg, 0.25 mmol) were mixed in DMF (17 ml). The mixture was sonicated for 30 min and subsequently added with 1, 5 or 10 molar equivalents of acetic acid. The resulting mixture was heated at 120 °C for 20 hours. After cooling to room temperature, the product was washed with DMF, dichloromethane and methanol, and then dried overnight under vacuum. The MIL-126 samples obtained with 1, 5 and 10 equivalents of acetic acid are named as MIL-126-1AA, MIL-126-5AA and MIL-126-10AA, respectively. MIL-126-1AA (Yield: 60 mg, 37.5 %), MIL-126-5AA (Yield: 30 mg, 18.75 %) and MIL-126-10AA (Yield: 45 mg, 28.13 %) were obtained as crystalline pale orange, orange, and red-orange powders, respectively.

2.4 Adsorption experiments

2.4.1 Kinetic experiments

An activated crystalline powder samples of the MOF under study (MIL-126-1AA, MIL-126-5AA or MIL-126-10AA; 2 mg) was added to an aqueous solution (10 mL) of either

PIR (20, 10 or 5 ppm) or KET (35, 20 or 5 ppm) at 25 °C. A sample (2.5 mL) is extracted from the suspension at predetermined time intervals and centrifuged to obtain a clear supernatant. The concentration of PIR or KET in the supernatant was determined from the absorbance based on UV-vis absorption measurements. The adsorption capacity (q_t, mg g^{-1}) and the removal rate (%) were calculated by Equations (1) and (2), respectively:

$$q_t = (C_0 - C_t)V \ / \ m \ (1)$$

$$Removal\ rate = [(C_0 - C_t) \ / \ C_0] \ \times \ 100\% \ (2)$$

2.4.2 Isothermal experiments

Aqueous solutions of PIR and KET (10 mL) in different concentrations (5–20 ppm for PIR; 5–35 ppm for KET) were prepared by successive dilution of premade stock solutions without pH adjustments. To each of these solutions, an activated crystalline sample of MIL-126-1AA, MIL-126-5AA or MIL-126-10AA (1 mg) was added. The UV-vis absorption spectra of the supernatant solution were measured after 24 hours. The variations of the absorption intensity at 360 nm for PIR and 259 nm for KET were measured to determine the respective equilibrium concentration (C_e) of PIR and KET in the supernatant solution.

2.4.3 Thermodynamic experiments

An activated crystalline sample of MIL-126-1AA, MIL-126-5AA or MIL-126-10AA (1 mg) was added to an aqueous solution (10 ml) of PIR or KET. The resulting suspension was kept at a constant temperature (25 °C, 35 °C and 55 °C). After 24 hours, the remaining concentration of the pharmaceuticals in each aqueous sample was determined by performing UV-vis absorption measurements with the supernatant solution.

2.4.4. Effect of coexisting ions and adsorption cycles

Sodium nitrate and magnesium nitrate hexahydrate were respectively used as the source of Na^+ and Mg^{2+} in the following measurements. An activated crystalline sample of

MIL-126-1AA, MIL-126-5AA or MIL-126-10AA (1 mg) was added to an aqueous solution (10 ml) of either PIR or KET in the presence of a known amount of Na^+ (0–1000 ppm) or Mg^{2+} (0–1000 ppm). After 24 hours, the remaining concentration of PIR and KET in the supernatant solutions was measured.

The reusability of the MIL-126-1AA, MIL-126-5AA and MIL-126-10AA was also determined. After the adsorption of KET, the used MIL-126 sample was washed and centrifuged with acetone and then ethanol, and subsequently dried under vacuum overnight. The recovered MIL-126 samples were used in subsequent cycles of adsorption after successive reactivation.

2.4.5 Effect of pH

The pH of the aqueous PIR solutions was adjusted by adding small amounts of 0.1 M NaOH or 0.1 M HCl solutions until the desired pH range (4–9) has been reached. In each measurement, an activated crystalline sample of MIL-126-1AA, MIL-126-5AA or MIL-126-10AA was soaked in one of the PIR solutions (5 ppm; 10 ml) with known pH values at 25 °C for 24 h.

3. Results and discussion

3.1 Synthesis and characterization

The iron(III) MOF, MIL-126, was synthesized solvothermally in the presence of acetic acid (AA) as the modulator according to a modified literature procedure by Forgan and co-workers (Bara et al., 2019). In MOF synthesis, ligands and modulators are reported to be in a competitive relationship. In the presence of modulators, the growth of MOFs are restricted and a better control of the crystallinity can be achieved (Schaate et al., 2011). Specifically, in the present case when AA is used as the modulator, the carboxylic acid unit of AA will compete with the carboxylic acid groups of H_2BPDC for coordination to the iron centers. The addition of a small amount of AA can affect the equilibrium reaction and slow down the crystallization process. On the other hand, a high concentration of AA is expected to facilitate the capping of the metal clusters by acetates, reducing the probability for the BPDC linkers to coordinate to iron, leading to missing linker defects. The unequal distribution of linker defects within the MOF structure will in turn result in the formation of missing cluster defects (Dissegna et al., 2018). Meanwhile, although Fe^{3+} salts are commonly used in the synthesis of iron(III) MOFs, there have been some reports on the use of Fe^{2+} salts (Bara et al., 2019; Choi et al., 2007; Sanselme et al., 2004 and Guesh et al., 2017). The autoxidation of Fe^{2+} to Fe^{3+} is suggested to slow down the assembly of the framework structure. Moreover, Fe^{2+} is a softer Lewis acid and it will increase the liability of ligands. This will enhance the reversibility of the metal–ligand coordination, directing to the formation of a structure with reduced defects, thus enhancing the crystallinity of the products (Dong et al., 2020 and Sanselme et al., 2004). Together with the use of acid modulators, a finer control on the amount of defects and crystallinity can then be achieved.

Fig. S1 illustrates the FTIR spectra of the free H_2BPDC linker and the as-synthesized MOFs, namely MIL-126-1AA, MIL-126-5AA and MIL-126-10AA. H_2BPDC shows a broad O–H stretch at 2250–3250 cm^{-1} from the carboxylic acid (–COOH) group. The absence of this O–H stretch in the spectra of the MOFs suggests the successful deprotonation of H_2BPDC for coordination with iron in the MOFs. The three acid-modulated MIL-126 samples exhibit highly similar structural vibrations. The peaks at 620 and 768 cm^{-1} correspond to the Fe–O stretching modes and C–H bending vibrations, respectively. The characteristic absorption peaks at approximately 1687, 1604 and 1398 cm^{-1}, respectively correspond to the C=O stretching vibrations, C–O asymmetric vibrations and C–O symmetric vibrations, and these vibrations mainly originate from the BPDC linkers in the MOFs (Sun et al., 2022).

The phase purity of the as-synthesized MIL-126 samples has been examined by PXRD as presented in Figure S2. The experimental PXRD patterns of MIL-126-5AA and MIL-126-10AA are in close agreement with the predicted PXRD pattern of MIL-126 (pattern predicted from Cambridge Structural Database (CSD) reference code MIBMERS2) (Horcajada et al., 2011), confirming that these two samples contain MIL-126 as a pure interpenetrating phase of the iron(III) MOF as reported in the literature. For the sample synthesized with a lower equivalent of the modulator, MIL-126-1AA, reduced phase purity is observed. Additional peaks that correspond to another iron(III) MOF, MIL-88D, can be observed in the PXRD pattern, indicating that a mixed phase has been formed (Bara et al., 2019).

To further confirm the phase purity and to investigate the textural and morphological properties, the modulated MOF samples have been characterized by SEM. As shown in Figure 1a and b, modulation produces predominantly MIL-126 as larger block-like structures in the presence of 1 equivalent of acetic acid. However, at a lower concentration of the modulator, rod-shaped structures corresponding to MIL-88D are also observed, many of which are intergrown with the block structures. The observations from SEM are consistent with the PXRD pattern of MIL-126-1AA (Figure S2), which shows additional minor peaks from MIL-88D (Bara et al., 2019). With an increase in the equivalents of the modulator, both MIL-126-5AA (Figure 1c and d) and MIL-126-10AA (Figure 1e and f) consist predominantly of the MIL-126 phase and a significant amount of intergrown block crystallites are observed. In addition, MIL-126-10AA exhibits a rough surface because more defects have been introduced upon the addition of a larger amount of the modulator (Forgan et al., 2020). Moreover, EDX mapping analysis has been performed to map the elemental distribution in the modulated MOFs. A uniform distribution of Fe, C, and O is observed in all of MIL-126-1AA, MIL-126-5AA and MIL-126-10AA as shown in Figure S3.

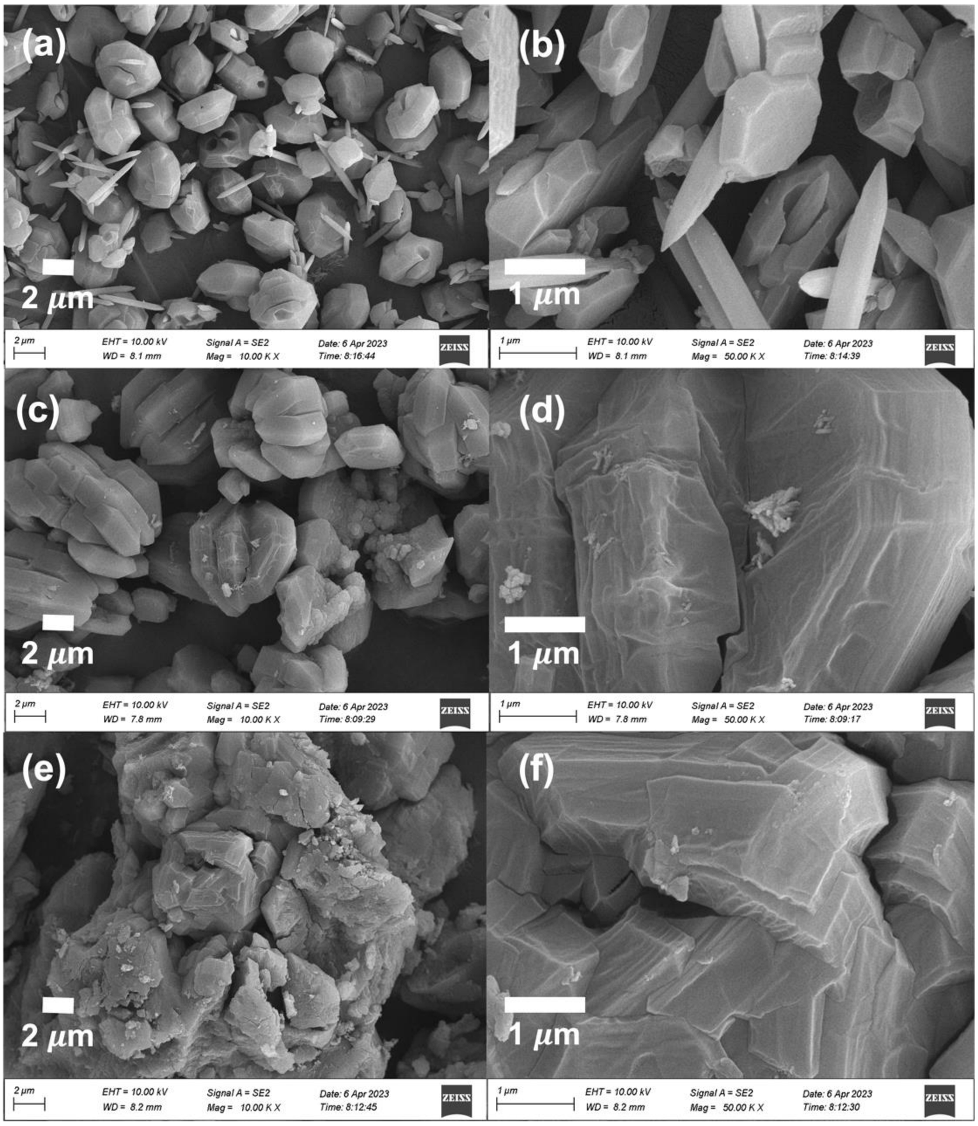

Figure 1. SEM images of (a,b) MIL-126-1AA, (c,d) MIL-126-5AA and (e,f) MIL-126-10AA at different magnifications.

Meanwhile, XPS analysis has provided additional information on the elemental contents and their oxidation states in the MOFs. The survey spectra in Figure 2a indicate the presence of iron (Fe), carbon (C) and oxygen (O) in the modulated MIL-126 samples. Fig. 2(b) shows the high-resolution Fe 2p XPS spectra of the MOFs. The Fe $2p_{1/2}$ peak is centered at 725.3 eV for MIL-126-1AA and at 725.7 eV for MIL-126-5AA and MIL-126-10AA, whereas the Fe $2p_{3/2}$ peak is centered at 711.4 eV for MIL-126-1AA and at 711.8 eV for MIL-126-5AA and MIL-126-10AA. The observation of these Fe $2p_{1/2}$ and Fe $2p_{3/2}$ peaks suggests that iron is present in the MOFs in the +3 oxidation state (Tan et al., 1990), which is consistent with the XPS analysis of other iron(III) MOFs (Tian et al., 2019). The deconvolution fitting in Figure 2c illustrates that the Fe 2p spectrum for each MOF sample consists of 4 peaks corresponding to Fe $2p_{3/2}$ (Fe^{3+}), Fe $2p_{1/2}$ (Fe^{3+}), and two additional satellite peaks corresponding to valence interband transitions (Fu et al., 2021 and Sun et al., 2023). This confirms the complete conversion of Fe^{2+} into Fe^{3+} during the MOF synthesis and thus the oxidation state of iron in the MIL-126 samples is iron(III). Moreover, the observation of a peak at 530 eV for all modulated MIL-126 samples is in accordance with the presence of Fe–O–C bonds in the MOFs.

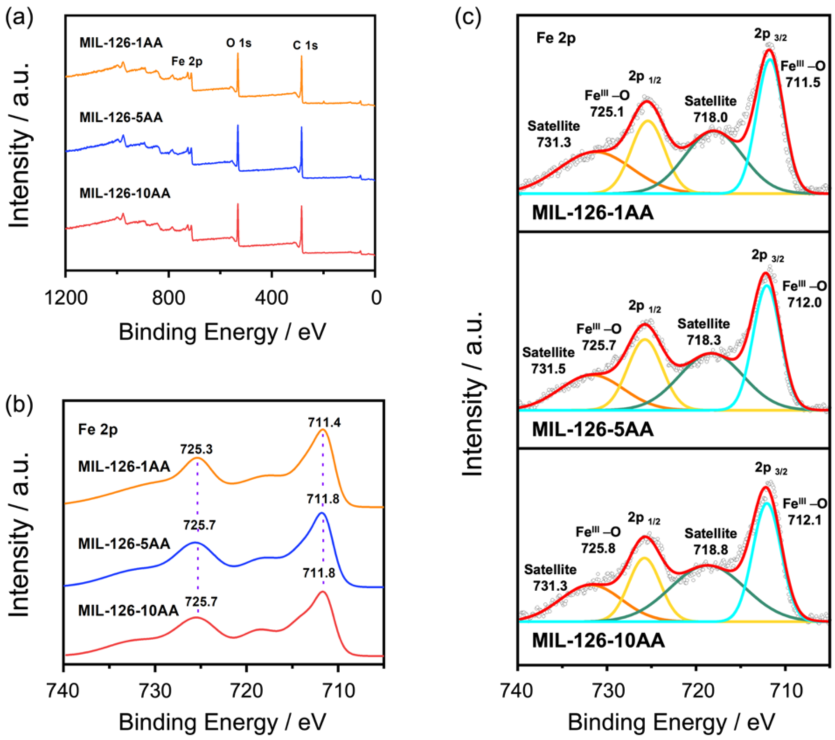

Figure 2. (a) XPS spectra of MIL-126-1AA, MIL-126-5AA and MIL-126-10AA. (b,c) Fe 2p spectra of MIL-126-1AA, MIL-126-5AA and MIL-126-10AA. Dots and full lines represent the raw intensity data and the deconvolution fitting intensities, respectively.

The nitrogen adsorption isotherms of MIL-126-1AA (S_{BET} = 447.1 m^2 g^{-1}) and MIL-126-5AA (S_{BET} = 737.1 m^2 g^{-1}) display Type I behavior while MIL-126-10AA (S_{BET} = 1068

$m^2\ g^{-1}$) displays Type IV behavior (Sing et al., 2004) as shown in Figure 3. The lower surface area of MIL-126-1AA is attributed to the lower phase purity in the presence of MIL-88D, which has been reported to collapse into a non-porous form after drying (Bara et al., 2019). The pore size distributions of the three MOFs based on the Barrett–Joyner–Halenda (BJH) calculation method are shown in Figure S4. While MIL-126-1AA shows the smallest pore size distribution among the three modulated MOF samples, MIL-126-10AA is found to show the highest porosity with mesopores ranging from 7.7 nm to 40 nm in diameter. This reveals that the use of a larger amount of the acid modulator during the synthesis can enhance the porosity of MOFs. The higher BET surface area in MIL-126-10AA, as well as the existence of mesopores as suggested by the Type IV isotherm, are associated to a larger amount of missing linker and/or missing cluster defects in the framework (Dissegna et al., 2018), in agreement with other previous studies (Marshall et al., 2018). The presence of more defects gives rise to larger pores within the framework (Cao et al., 2023 and Zhao et al., 2023) and hence the nitrogen uptake of MIL-126 increases with the amount of acid modulators used in the synthesis.

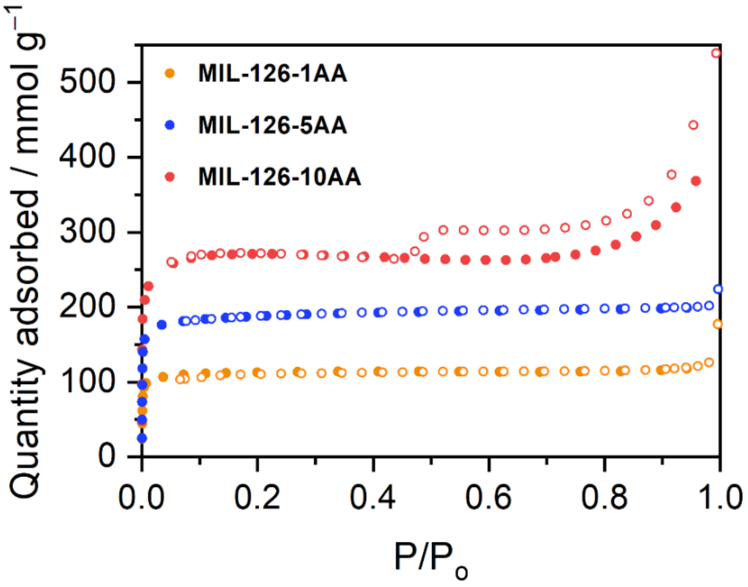

Figure 3. Nitrogen sorption isotherms of MIL-126-1AA, MIL-126-5AA and MIL-126-10AA at 77 K. Closed and open circles represent adsorption and desorption branches, respectively.

Moreover, the stability of the MOFs have been evaluated by TGA. As the compositions of the MIL-126 samples are essentially the same, the TGA patterns of the three modulated MIL-126 samples exhibit similar shapes with similar decomposition temperatures as illustrated in Figure S5. Upon heating, moisture is removed from the activated MOFs until about 130 °C. There continues to be a slow decrease in the weight between 250 and 400 °C, which is attributed to the removal of hydroxyl (–OH) groups from the framework (Ahmed et al., 2023). The dehydroxylated phase is stable up to about 400 °C (Larabi et al., 2012). Based on the weight loss between 250 and 400 °C, the concentration of –OH groups in MIL-126-1AA, MIL-126-5AA and MIL-126-10AA are estimated to be 4.36, 3.32 and 4.56 wt.%, respectively, corresponding to hydroxyl contents of 2.42, 1.84 and 2.53 mmol g^{-1}(Ahmed et al., 2023).

Above 400 °C, a significant weight loss is observed, which indicates a degradation of the MOF structures with the removal of linkers from the framework structures. As the amount of acetic acid was increased from 1 to 10 equivalents from MIL-126-1AA to MIL-126-10AA, the amount of oxide residues is observed to decrease. This suggests that there are relatively fewer Fe_3O metal clusters per unit in MIL-126-5AA and MIL-126-10AA, associated with larger amounts of missing cluster defects due to acid etching. On the other hand, MIL-126-1AA with the smallest amount of defects gives the largest amount of oxide residues after decomposition, in agreement with previous studies (Bara et al., 2019). This indicates that MIL-126-1AA contains the highest density of Fe_3O clusters among the three modulated MIL-126 samples.

3.2 Adsorption studies

As revealed from the characterization and morphological studies, the use of acetic acid as a modulator has successfully promoted the synthesis of MIL-126 as the dominant phase. With improved phase purity, the metal clusters in the MOFs can become more exposed and accessible for the contact with guests such as pollutants, thus significantly increasing the adsorption ability when compared to a multiphase material. To evaluate the applications of the modulated MIL-126 samples in water remediation, adsorption studies have been performed using activated samples of the MOFs to study their performance in the elimination of PIR and KET from aqueous solutions.

3.2.1 Adsorption kinetics and adsorption isotherm

The effect of contact time on the adsorption of PIR and KET at different initial concentrations is respectively shown in Figure S6 and Figure 4. The adsorption process has been monitored by UV-vis absorption spectroscopy. The linear relationship between the concentration of PIR and the absorption at 360 nm, and that between the concentration of KET and the absorption intensity at 259 nm, are shown in Figure S7. The pseudo-first-order and pseudo-second-order kinetic models have been applied to study the kinetics of the adsorption processes, and the respective parameters are presented in Tables S1 and S2. The equations for the pseudo-first order and pseudo-second order models are expressed by Equations (3) and (4) (Seo et al., 2015), respectively:

$$\ln(q_e - q_t) = ln q_e - K_1 t \ (3)$$

$$t/q_t = 1/(K_2 q_e^2) + t/q_e \ (4)$$

where q_e and q_t are respectively the adsorption capacities (mg g^{-1}) at equilibrium and time t, K_1 (min^{-1}) is the rate constant of the pseudo-first-order model, and K_2 (g mg^{-1} min^{-1}) is the rate constant of the pseudo-second-order model.

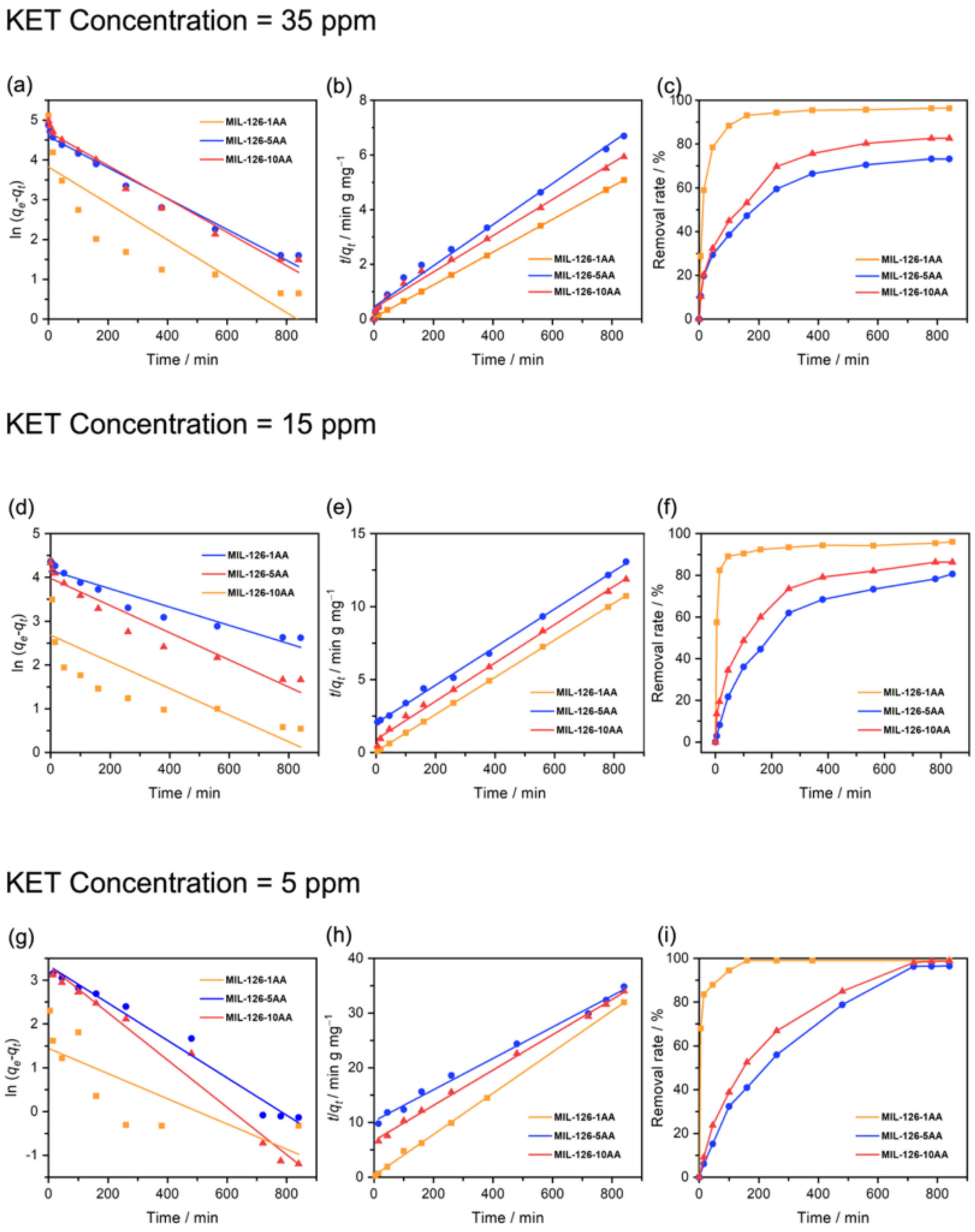

Figure 4. (a,d,g) Pseudo-first-order model fitting curves; (b,e,h) pseudo-second-order model fitting curves; (c,f,i) changes in the removal rates with time for the adsorption of KET by MIL-126-1AA, MIL-126-5AA and MIL-126-10AA at three different initial concentrations of KET (35, 15 and 5 ppm).

The adsorption of the pharmaceuticals, especially KET, by the MIL-126 samples is rapid at the initial stages of the contact period. Equilibrium is reached within 800 min, and this is probably due to the saturation of active sites as the adsorption proceeds. The removal rates for both PIR and KET are in order of MIL-126-1AA > MIL-126-10AA > MIL-126-5AA throughout the adsorption process irrespective of the initial concentrations of PIR and KET.

In particular, for the adsorption of KET (Figure 4), MIL-126-1AA shows excellent performance when compared to MIL-126-5AA and MIL-126-10AA. The adsorption reaches equilibrium within 200 min and the removal efficiency exceeds 96 % at all initial concentrations of KET. Almost quantitative removal (98.8 %) can be reached in 160 min when the initial concentration is 5 ppm. As shown in Table S2, for the three modulated MOF samples, the coefficient of determination (R^2) of the pseudo-second-order model is always higher than that of the pseudo-first-order model. Moreover, the q_e obtained by the pseudo-second-order model fitting is closer to the equilibrium adsorption capacity obtained in the experiment ($q_{e,\mathrm{exp}}$), indicating that the adsorption of KET follows pseudo-second-order kinetics.

The adsorption isotherm models have been used to explore the distribution of adsorbed molecules on the adsorbents when the adsorption reaches equilibrium. The Langmuir and Freundlich models (Haque et al., 2010) are chosen to analyze the experimental data and are expressed as follows:

Langmuir model: $C_e/q_e = C_e/q_{max} + 1/(q_{max}K_L)$ (5)

Freundlich model: $lnq_e = \ln k_F + 1/n(lnC_e)$ (6)

where q_e (mg g^{-1}) is the amount of PIR or KET adsorbed at the equilibrium concentration, C_e (mg L^{-1}). q_{max} represents the maximum adsorption capacity of the adsorbent and K_L (dm^3 mg^{-1}) is the Langmuir constant. n and K_F are the Freundlich constants which represent the adsorption capacity and adsorption intensity, respectively.

The liner curves fitted by the Langmuir and Freundlich isotherm models for PIR and KET are shown in Figure 5. The R^2 values of the liner curves fitted by the Langmuir model are higher than those for the Freundlich model, indicating that the Langmuir model is more suitable for describing the adsorption process. Therefore, the adsorption of PIR and KET by the MIL-126 samples is probably dominated by monolayer adsorption, in which the adsorption of PIR and KET mainly occur at the surface active sites of the MOFs (Yang et al., 2020). The maximum adsorption capacities (q_{max}) of PIR and KET follow the order MIL-126-1AA > MIL-126-10AA > MIL-126-5AA (Table S3). The sample prepared with the lowest equivalent of the modulator, namely MIL-126-1AA (q_{max} = 452.49 for KET and q_{max} = 209.65 for PIR), has been observed to show about two times higher q_{max} values when compared to MIL-126-5AA and MIL-126-10AA at 298 K. The q_{max} values are compared with those of various adsorbents for the removal of PIR and KET (Table S4). It is observed that the adsorption performance of MIL-126-1AA, MIL-126-5AA and MIL-126-10AA is comparable to that of the reported materials, with MIL-126-1AA showing the highest adsorption capacity that outperforms other MOFs and porous adsorbents. This suggests that MIL-126-1AA, MIL-126-5AA and MIL-126-10AA are promising candidates for the adsorptive removal of NSAIDs and other PPCPs.

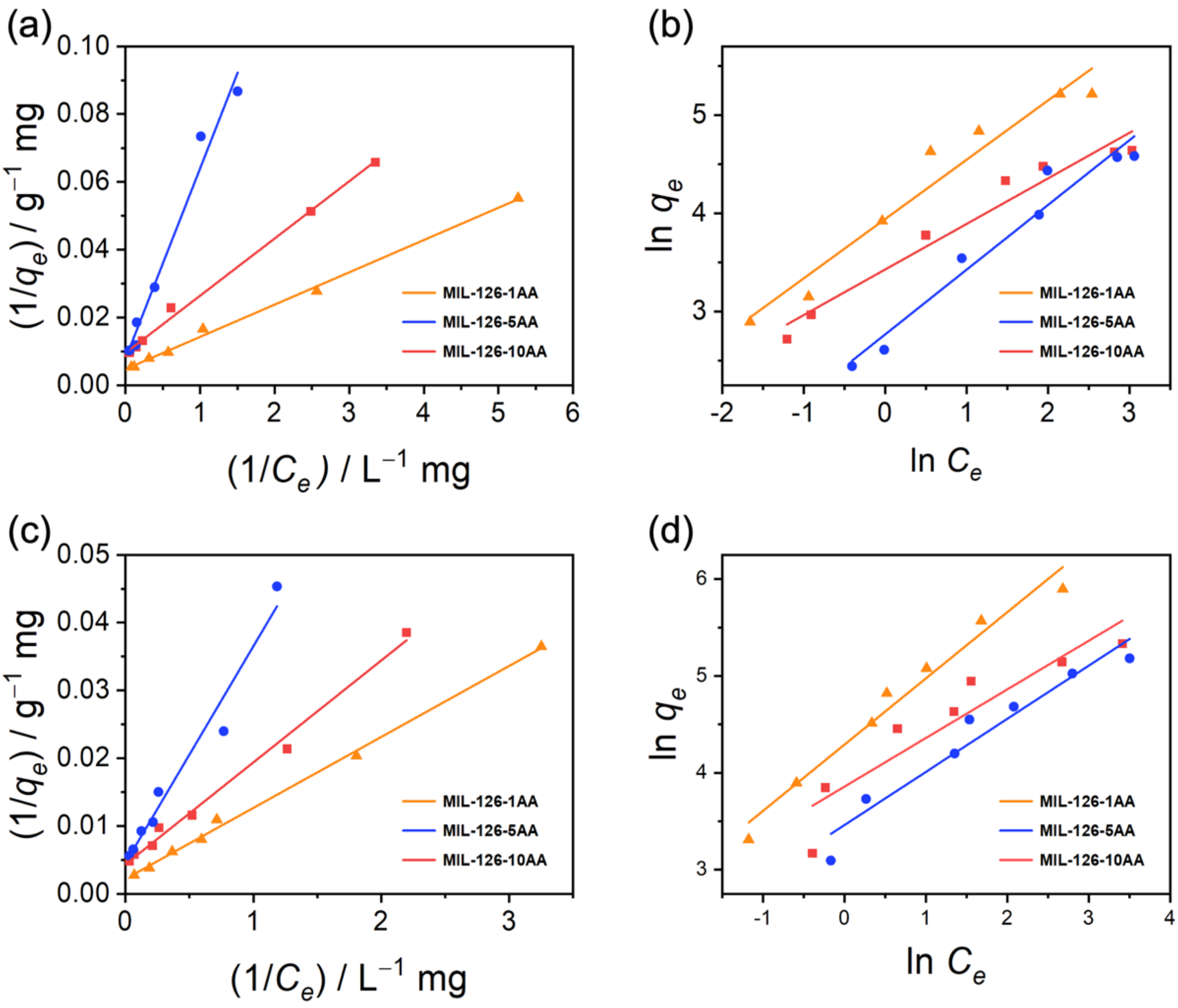

Figure 5. Fitting curves of the (a,c) Langmuir and (b,d) Freundlich adsorption isotherm models for the adsorption of PIR and KET by MIL-126-1AA, MIL-126-5AA and MIL-126-10AA.

3.2.2 Thermodynamic experiments

The effect of temperature on the removal of PIR and KET by the MIL-126 samples has been studied. The thermodynamic parameters of adsorption were calculated by the following equations (Zhuang et al., 2019):

$$\mathrm{K_L} = q_e/q_c \ (7)$$

$$\mathrm{lnK_L} = \ \Delta S/\mathrm{R} - \Delta \mathrm{H}/\mathrm{RT} \ (8)$$

$$\Delta G = \Delta H - T\,\Delta S^{\circ} \quad (9)$$

where q_e (mg g^{-1}) indicates the equilibrium adsorption capacity, C_e (mg L^{-1}) is the equilibrium concentration of PIR or KET in the solution, K_L is the distribution coefficient, ΔG is the Gibbs free energy, ΔH is the enthalpy and ΔS is the standard entropy. R (= 8.314 J mol^{-1} K^{-1}) is the ideal gas constant.

The values of ΔS and ΔH can respectively be obtained from the intercept and the negative slope of the plot with 1/T as the abscissa and lnK_L as the ordinate (Figure S8). A higher temperature is found to promote the removal of both PIR and KET, indicating that the adsorption process is endothermic in nature. As shown in Table S5, ΔG is negative at all temperatures, revealing that the adsorption is thermodynamically favorable and occurs spontaneously.

3.2.3 Effect of ionic strength and adsorption cycles

In real wastewater, there are many salts that will influence the removal of pollutants. Therefore, Na^+ and Mg^{2+} have been selected as representative ions to assess the effect of ionic strength on the adsorption abilities of MIL-126-1AA, MIL-126-5AA and MIL-126-10AA for PIR and KET as shown in Figure S9. The adsorption capacities of the three MIL-126 samples are observed to remain more or less the same as the ionic strength increases, indicating a negligible effect of the ionic strength on the adsorption of PIR and KET by the adsorbents. It is likely that Na^+ and Mg^{2+} might accumulate around the MOF surface, creating an electrostatic shielding effect to prevent the adsorption of the organic drugs (Liu et al., 2014). Moreover, the presence of Na^+ and Mg^{2+} would reduce the pore size and increase the potential resistance effect (Jin et al., 2017). However, these effects are rather insignificant and the adsorption capacities of the modulated MIL-126 samples are not significantly affected by the presence of coexisting ions. Therefore, compared to many other adsorbents whose adsorption performance would rapidly decrease with increased ionic strength, these modulated iron(III) MOFs can be considered as attractive and highly efficient adsorbents that may be potentially be used for the removal of PPCPs in practical scenarios.

Furthermore, the practical application of an adsorbent is determined by its reusability and stability. As illustrated in Figure 6, MIL-126-1AA, MIL-126-5AA and MIL-126-10AA can be reused, after washing with acetone and methanol, for at least 3 cycles with only a slight decrease in the adsorption capacity for KET. This decrease is probably due to the occupation of a minute amount of the MOF pores by KET. For MIL-126-1AA, its reduced q_e in the first cycle is also attributed to the destruction of the pores of the trace amounts of MIL-88D present in the sample. As aforementioned in Section 3.1, the synthesis with a small amount of the acid modulator would give rise to a mixture of MIL-126 and MIL-88D in MIL-126-1AA. While the interpenetrated MIL-126 phase has been reported to exhibit permanent porosity, the non-interpenetrated MIL-88D phase would become non-porous when guest molecules are removed from the pores after adsorption (Dan-Hardi et al., 2012). Nevertheless, MIL-126-1AA is still the most efficient adsorbent when compared to MIL-126-5AA and MIL-126-10AA. The reusability of the MOFs can further be supported by the FTIR spectra of the modulated MOFs, the recycled MOFs and KET as shown in Figure S10.

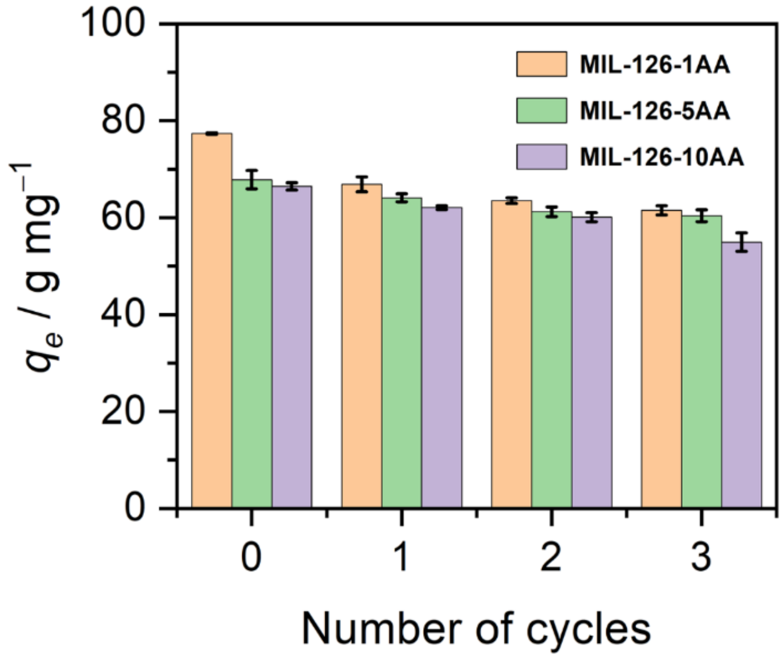

Figure. 6. Recyclability of MIL-126-1AA, MIL-126-5AA and MIL-126-10AA for the adsorption of KET.

3.2.4 XPS Analysis after adsorption

XPS Tests of the modulated MIL-126 samples before and after adsorption further confirm the interactions between the MOFs and the pharmaceutical molecules (Figure 7 and Figure S11). Figure 7(a) and Figure S11(a) show that the binding energy of Fe 2p is slightly decreased after the adsorption of either PIR or KET, indicating a partial increase in the Fe 2p charge density due to the interaction between Fe and the pollutants (Zhang et al., 2021). Moreover, the O 1s high-resolution spectra for the modulated MOFs (Figure 7b and Figure S11b) display the peaks for C=O, C–O and Fe–O after the adsorption of either pharmaceutical. After the adsorption, the O 1s spectra show higher binding energy of C=O for all of MIL-126-1AA, MIL-126-5AA and MIL-126-10AA, suggesting the involvement of the carboxyl groups on the MOF surface in the adsorption of PIR and KET (Du et al., 2014), possibly via hydrogen bonding interactions. The Fe–O bonding energies in all adsorbents shift to lower energy and the relative areas of the Fe–O signals increase after the adsorption.

This indicates the significant participation of the Fe_3O iron oxide clusters in the MOFs during the adsorption of PIR and KET. The appearance of a S=O signal in the O 1s spectra after the adsorption of PIR further confirms the successful adsorption of the pharmaceutical molecules by the MOFs. Further evidence of adsorption can be obtained from the N 1s spectra as depicted in Figure 7c and Figure S11c. Before the adsorption, there is no appreciable signal in the N 1s spectra of the adsorbents. However, the N 1s spectra after the adsorption of PIR show a peak that can be deconvoluted into the signals from Fe–N (Poozhikunnath et al., 2020), as well as the amide N and pyridine N from PIR. The largest contribution from Fe–N suggests the formation of a coordination bond between Fe and the pyridine functional group of PIR, and hence coordination bond might play an additional role in the adsorption of PIR by the iron(III) MOFs.

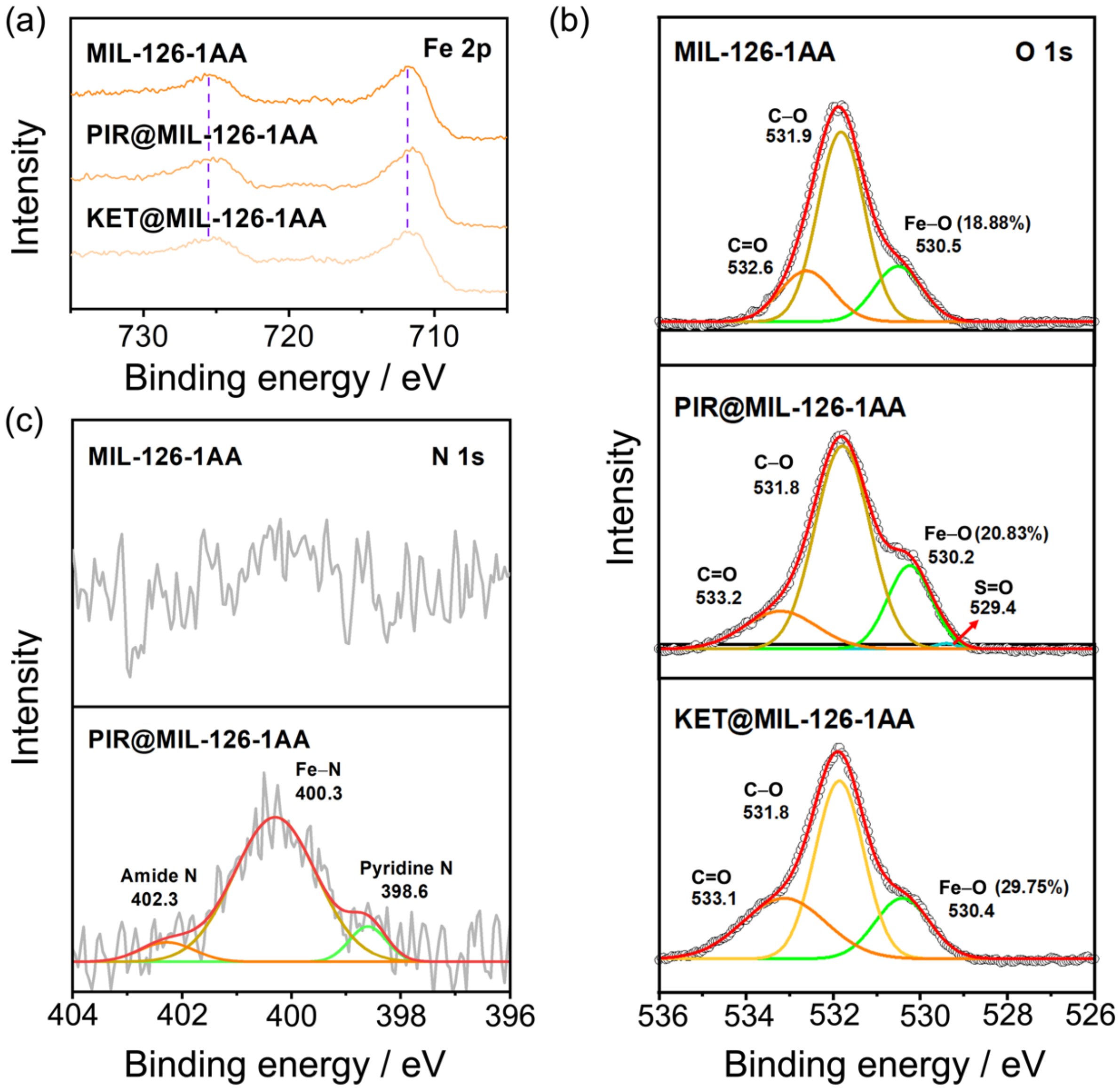

Figure 7. (a) Broad scan Fe 2p spectra of the MIL-126-1AA before and after the adsorption of PIR and KET. (b) O 1s spectra of the modulated MOFs before and after the adsorption of PIR and KET. Dots and full lines represent the raw intensity data and the deconvolution fitting intensities, respectively. (c) N 1s spectra of the modulated MOFs before and after the adsorption of PIR.

3.2.5 Effects of pH

The pH of solutions usually affects the adsorption process in the aqueous phase, as both the adsorbents and the adsorbates can be protonated or deprotonated under different pH conditions. To better understand the adsorption properties of the modulated MOFs, PIR is selected as the representative pharmaceutical for adsorption studies at different pH. As shown in Figure 8, PIR is zwitterionic with two pKa values ($pK_{a1} = 1.86$ and $pK_{a2} = 5.46$). Theoretically, PIR molecules exist as cations at $pH < 1.86$, as zwitterionic forms at $1.86 < pH < 5.46$, and as basic forms at $pH > 5.46$ (Ulrich et al., 2021).

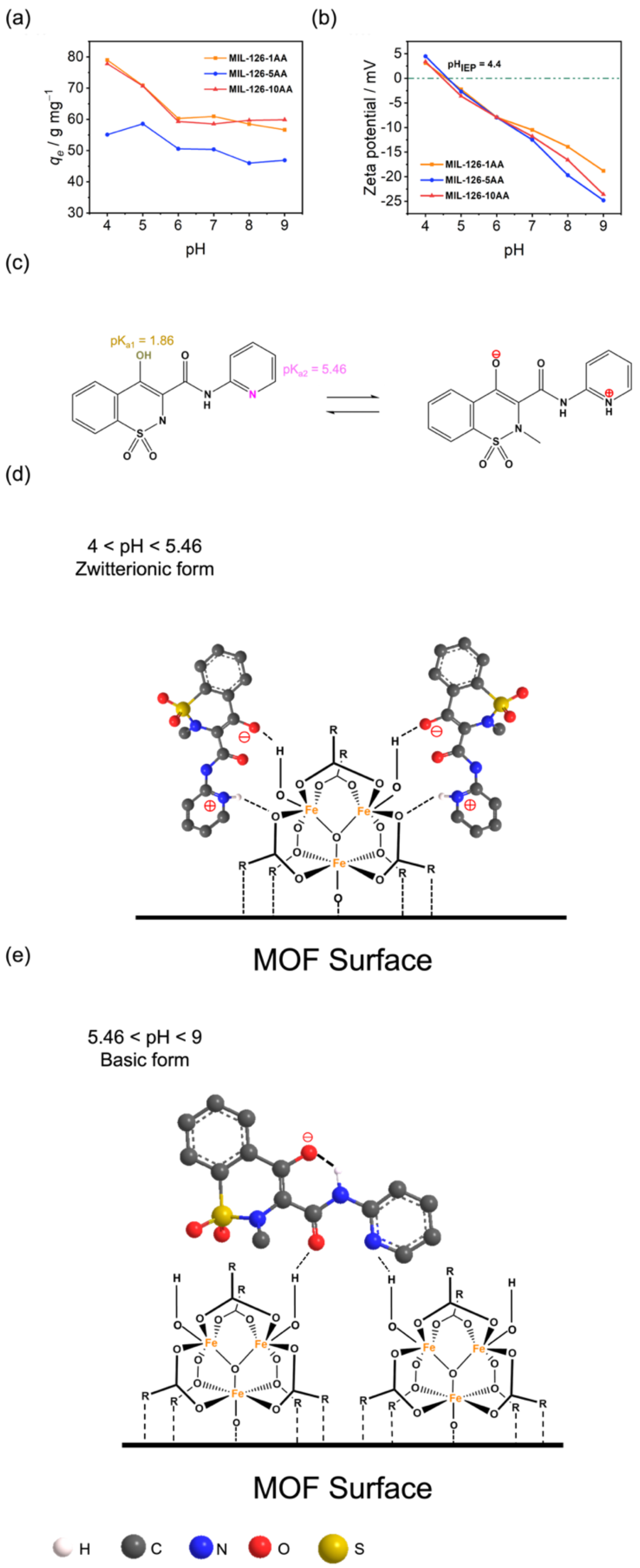

Figure 8. (a) Effect of pH on the adsorption of PIR by MIL-126-1AA, MIL-126-5AA and MIL-126-10AA. (b) Zeta potentials of MIL-126-1AA, MIL-126-5AA and MIL-126-10AA at different pH. (c) Equilibrium between the neutral and zwitterionic forms of PIR, and the

pKa's of the ionizable groups. Schematic diagrams showing the plausible hydrogen bonding interactions between the iron(III) MOF surface and (d) the zwitterionic and (e) the basic form of PIR under different pH conditions.

The modulated MOFs are found to be relatively stable in a wide pH range (pH= 4–9). As shown in Figure 8a, the equilibrium adsorption capacity (q_e) of PIR by the MOFs decreases slightly when pH is increased to 6. This is due to the structural change of PIR from the zwitterionic form to the basic form. The corresponding zeta potentials of the MIL-126 samples have been measured (Figure 8b). When the pH is increased from 4 to 9, the surface charge of the iron(III) MOFs becomes negative, leading to repulsion between PIR and the adsorbents. However, the adsorption capacity does not show a significant decrease when the pH value is further increased from 6 to 9. This suggests that the electrostatic effect is not the dominant factor in the adsorption process.

In addition, defective MOFs obtained by modulation exhibit a larger amount of hydrophilic functional groups, such as terminal $-OH$ and $-OH_2$ groups (Xian et al. 2019) and these functional groups can readily interact with adsorbents via hydrogen bonding. Figure 8c shows the equilibrium between the neutral and zwitterionic forms of PIR and the pKa's of the ionizable groups. PIR can act as both the H-donor and acceptor to interact with the iron(III) MOF, when the pH is lower than pK_{a2}. The relatively high q_e at pH 4 and 5 can thus be attributed to the hydrogen bonding interactions between PIR and the MOFs (Ahmed et al., 2022). This can be illustrated in Figure 8d which shows the plausible hydrogen bonding interactions between the iron(III) MOF surface and the zwitterionic form. It is expected that extensive hydrogen bonding interactions can be formed around the Fe_3O clusters via $-OH$, $-OH_2$ as well as Fe–O–C units on MIL-126, giving rise to a relatively higher adsorption capacity at $4 < pH < 5.46$. When the pH is greater than the pK_{a2} of PIR at pH > 6, q_e does not show a significant decrease (Figure 8a). This indicates that the role of PIR as a H-donor can be neglected, because if this was the case, the absence of H-donating groups in PIR under basic conditions would have led to very low q_e values. As depicted in Figure 8e, when the pH is higher than 5.46, the pyridine H of PIR will be deprotonated to give the basic form. In this case, PIR can no longer act as a proton donor and thus hydrogen bonding between PIR and MIL-126 should occur via the ‒OH and ‒OH_2 groups on the surface of the modulated MOFs. Fe‒O‒C units on the MOF would not participate in the hydrogen bonding, and it is likely that each PIR molecule would interact with more than one Fe_3O cluster for higher affinity. As a result, the adsorption capacity would become lower when the pH is increased to 6, but remain more or less constant as pH is further increased to 9. Moreover, π‒π stacking may occur between the aromatic units in PIR and the organic linkers of the MOFs (Zhao et al., 2021). As aforementioned in the XPS analysis, the coordination between Fe and the nitrogen donor units in PIR further contributes to the interactions between the MOFs and the adsorbents. A high concentration of Fe_3O clusters is therefore critical to the effective formation of hydrogen bonding and Fe‒N coordination with the pharmaceuticals. In this regard, despite larger surface areas, MIL-126-5AA and MIL-126-10AA with larger amounts of missing cluster defects would show poorer interactions with PIR and KET, and thus lower adsorption performance. It can thus be concluded that the adsorption of PIR and KET is governed by an interplay of non-covalent interactions, especially hydrogen bonding around the Fe_3O clusters.

4. Conclusions

In summary, a series of modulated MIL-126 samples has been synthesized in the presence of acetic acid as the modulator in carefully-controlled amounts. The modulated MOFs have been utilized for the adsorption of two representative NSAIDs, namely PIR and KET. Among the modulated MOFs studied, MIL-126-1AA shows the best performance due to an optimal amount of defects and a high density of the Fe_3O cluster active sites. The kinetics, thermodynamics and mechanisms of the adsorption process have been investigated in detail. Although defects can increase the surface area of MOFs, this does not necessarily imply better performance in adsorption. With the support of XPS studies, it is proposed that the Fe_3O clusters and hydrogen bonding play major roles in the adsorption process, and hence MIL-126-1AA with less missing cluster defects would perform better than the more defective MIL-126-5AA MIL-126-10AA with larger pores and surface areas. We therefore successfully demonstrated that a fine control in the amount of defects is critical for the host-guest interactions in MOFs and thus the adsorption kinetics and capacities. All of the modulated MOFs are readily reused after washing with organic solvents, rendering them attractive recyclable adsorbents for the removal of PPCPs from water. In addition to the development of new adsorbents for the adsorptive removal of organic pollutants in the environment, this work has provided further insights on the use of modulated synthesis for defect engineering in MOFs to enhance the adsorption efficiency of MOF-based materials for environmental remediation as well as other functions.

5. Supplementary Data of article 2

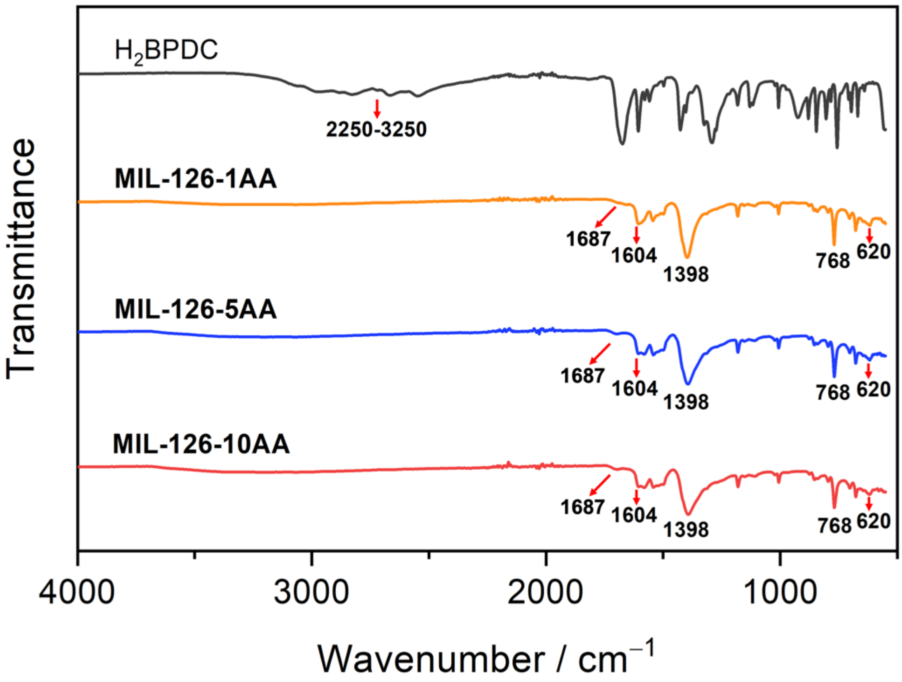

Figure. S1. FTIR spectra of H_2BPDC, MIL-126-1AA, MIL-126-5AA and MIL-126-10AA.

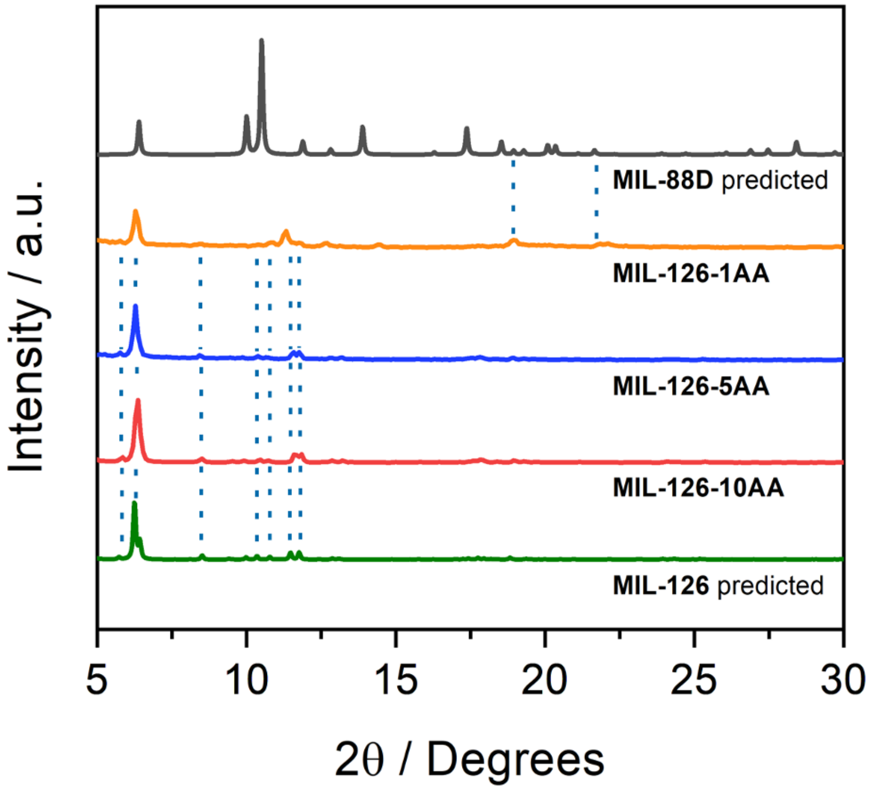

Figure. S2. From top to bottom: The predicted PXRD pattern of MIL-88D; the experimental PXRD patterns of as-synthesized MIL-126-1AA, MIL-126-5AA and MIL-126-10AA; and the predicted PXRD pattern of MIL-126. (The predicted patterns are obtained from the Cambridge Structural Database.)

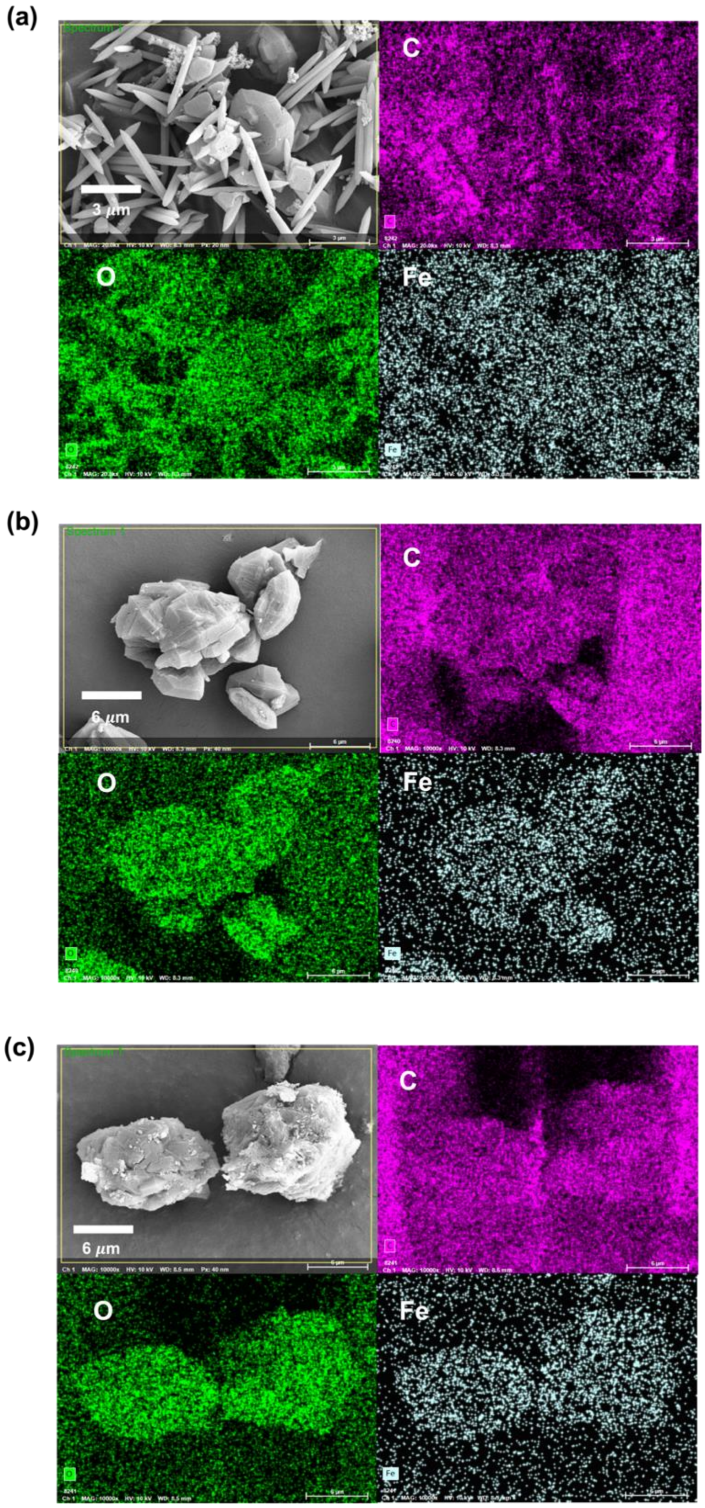

Figure. S3. Scanning electron microscopy (SEM) images and energy dispersive X-ray (EDX) mapping analysis of (a) MIL-126-1AA, (b) MIL-126-5AA and (c) MIL-126-10AA.

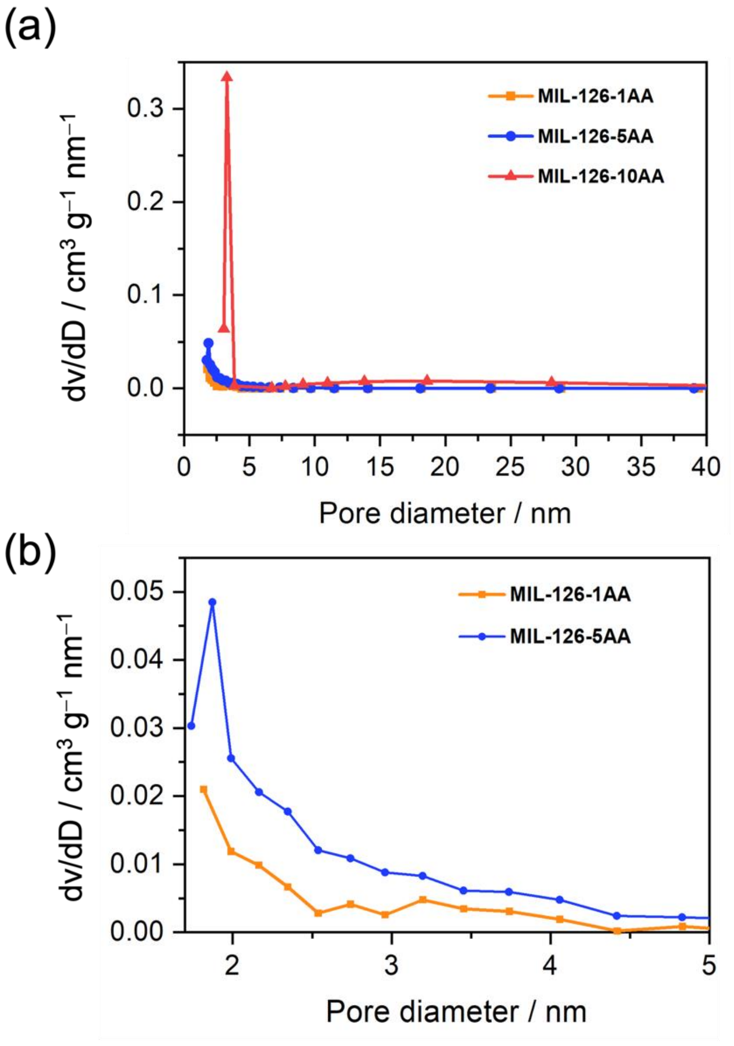

Figure. S4. (a) Pore size distributions calculated by the Barrett–Joyner–Halenda (BJH) method of the as-synthesized MIL-126 samples. (b) A magnified version of the pore size distribution for MIL-126-1AA and MIL-126-5AA.

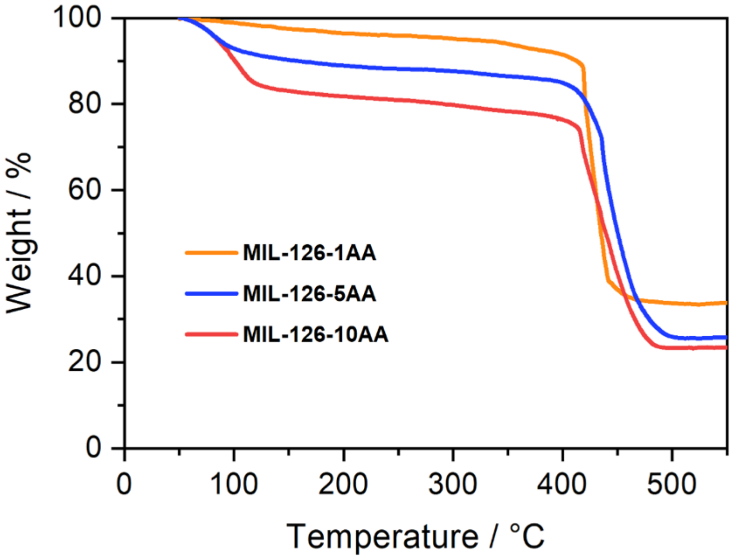

Figure. S5. Thermogravimetric analysis profiles of MIL-126-1AA, MIL-126-5AA and MIL-126-10AA.

PIR Concentration = 20 ppm

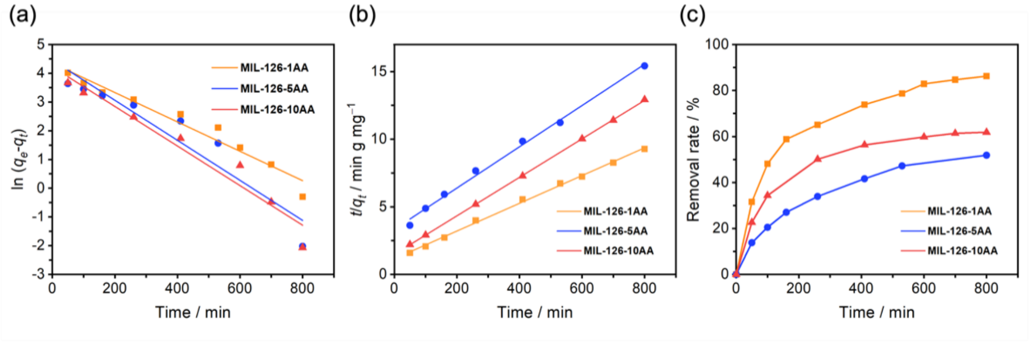

PIR Concentration = 10 ppm

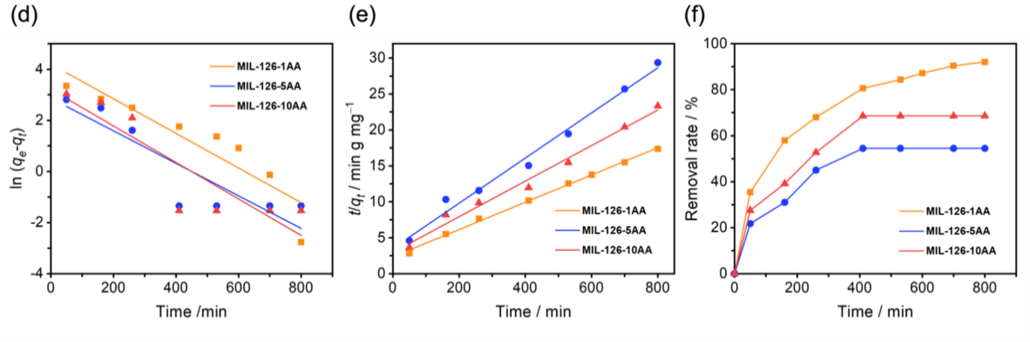

PIR Concentration = 5 ppm

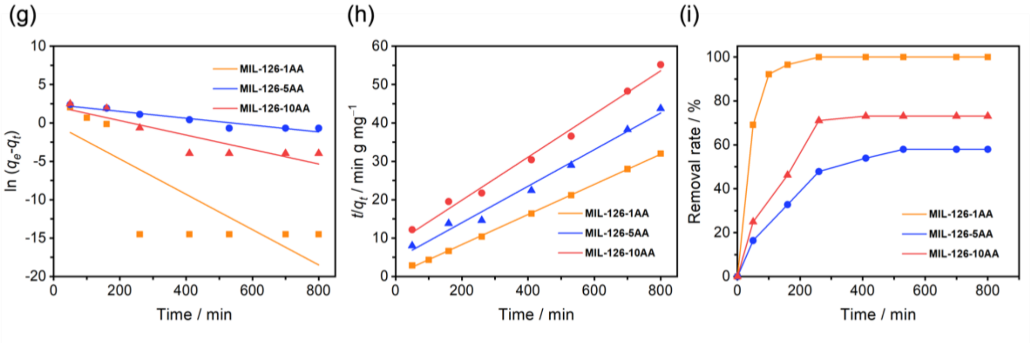

Figure. S6. (a,d,g) Pseudo-first-order model fitting curves; (b,e,h) pseudo-second-order model fitting curves; (c,f,i) changes in the removal rates with time for the adsorption of PIR by MIL-126-1AA, MIL-126-5AA and MIL-126-10AA at three different initial concentrations of PIR (20, 10 and 5 ppm).

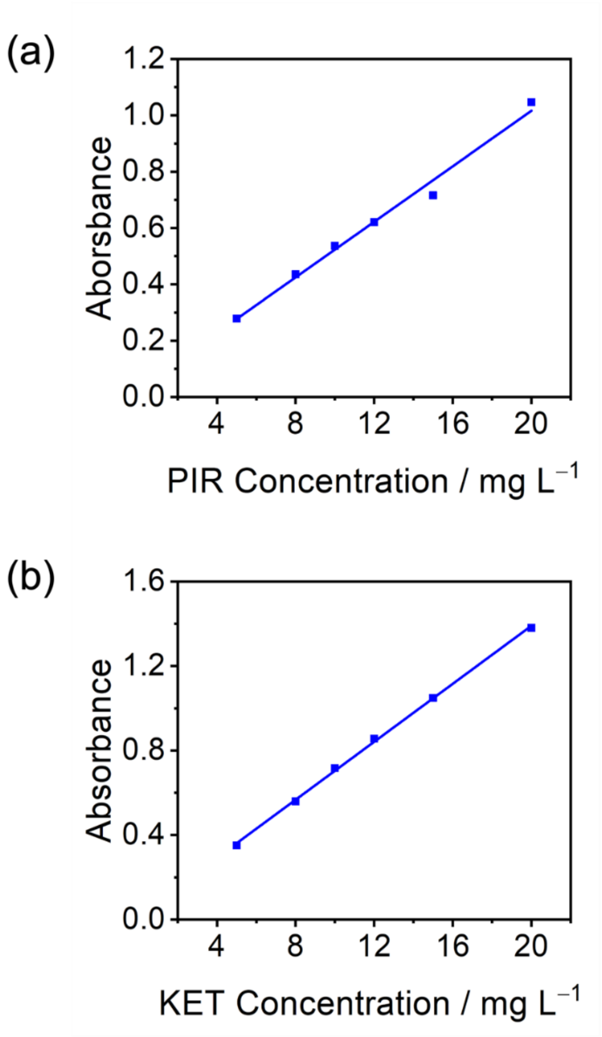

Figure. S7. The linear relationships between the concentration of (a) PIR (R^2 = 0.9880), (b) KET (R^2 = 0.9991) and the absorbance in the UV-vis absorption measurements.

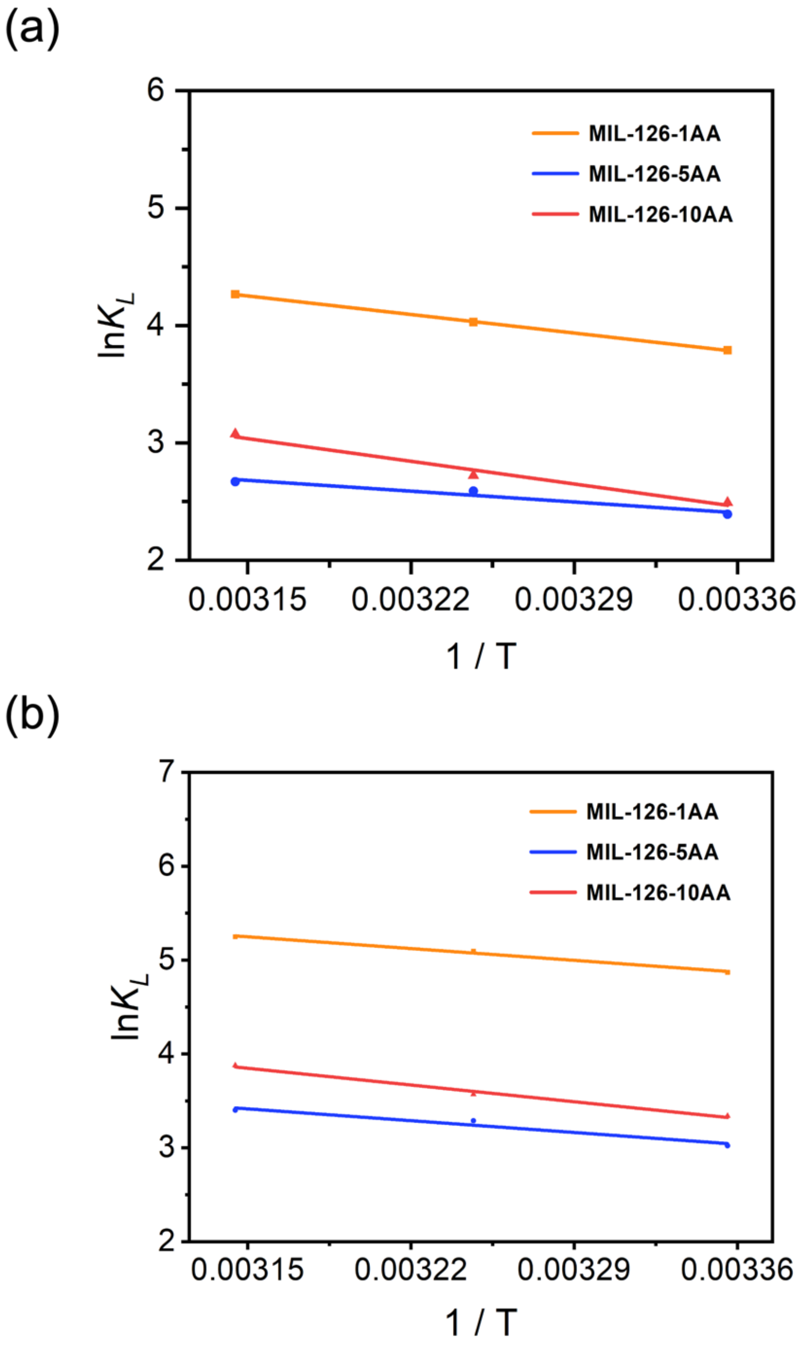

Figure. S8. The thermodynamic plots for the adsorption of (a) PIR and (b) KET by MIL-126-1AA, MIL-126-5AA and MIL-126-10AA.

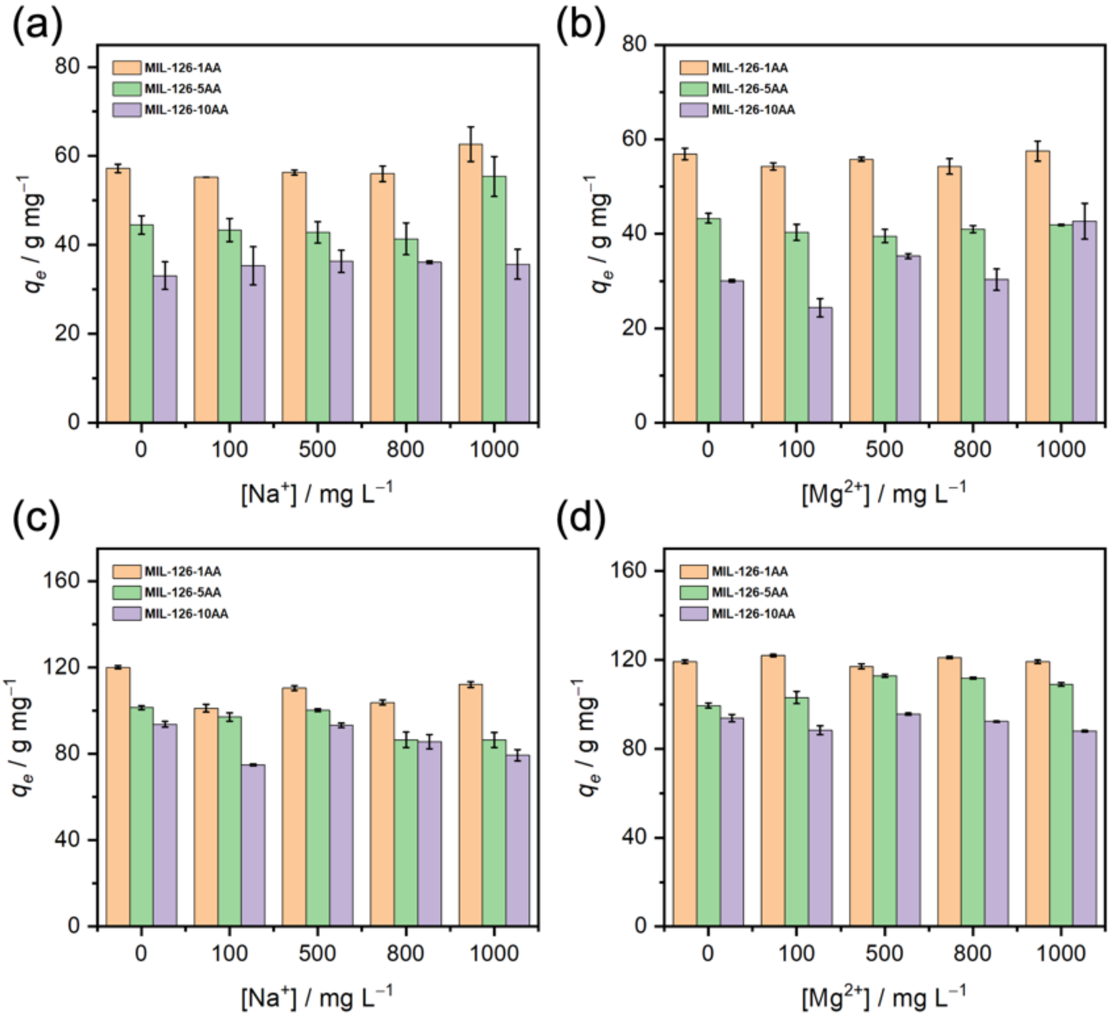

Figure S9. Effects of coexisting ions on the removal efficiency of (a,b) PIR and (c,d) KET by MIL-126-1AA, MIL-126-5AA and MIL-126-10AA.

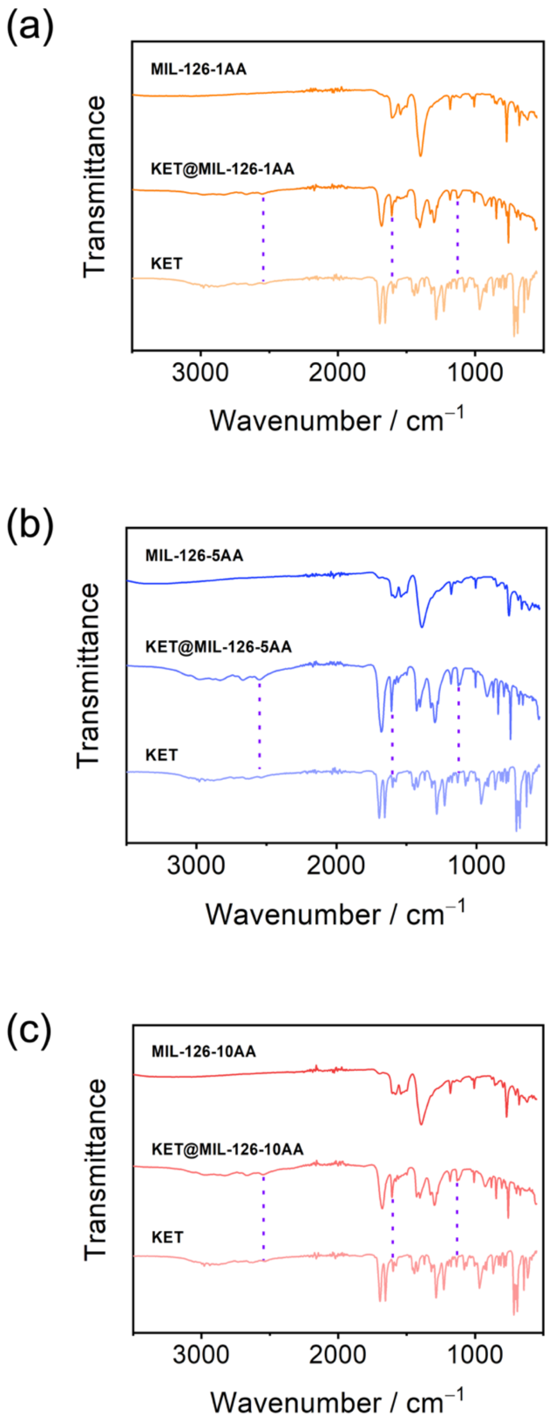

Figure S10. The FTIR spectra of (a) MIL-126-1AA, (b) MIL-126-5AA and (c) MIL-126-10AA before and after recycling from the adsorption of KET. The FTIR spectrum of KET is also included for comparison.

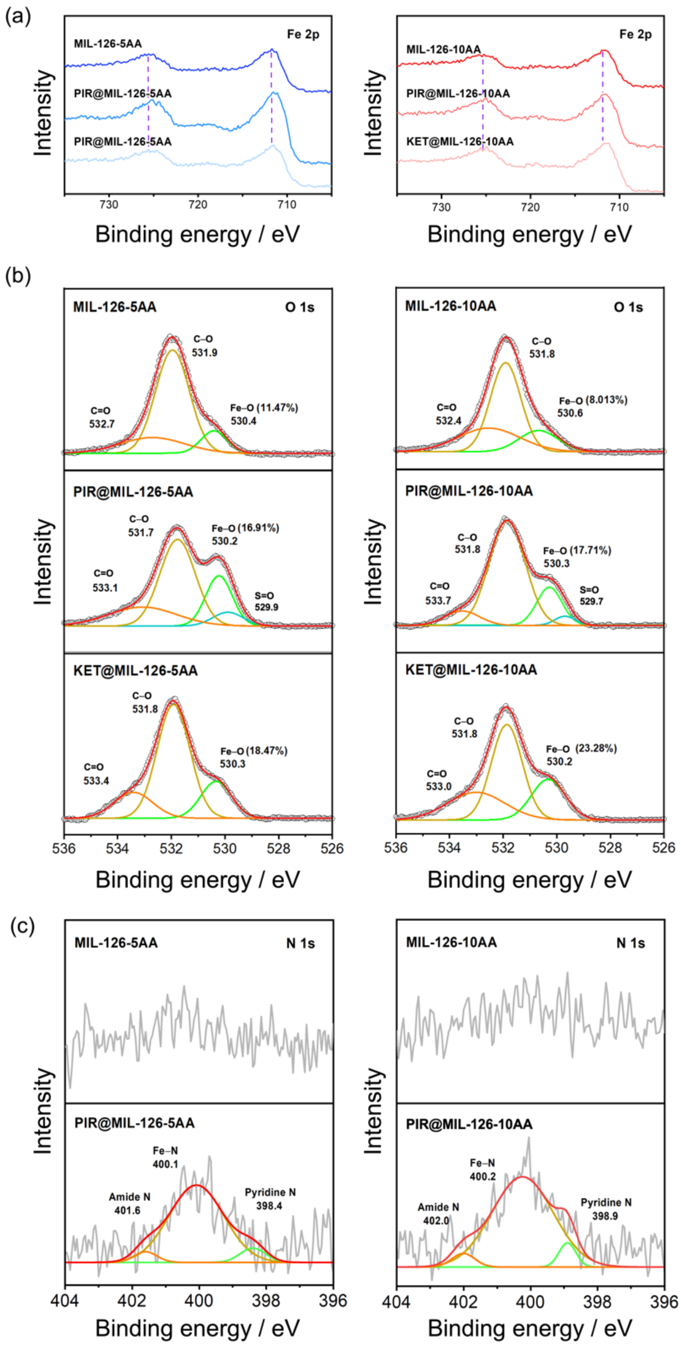

Figure S11. (a) Broad scan Fe 2p spectra of the MIL-126-5AA (left) and MIL-126-10AA (right) before and after the adsorption of PIR and KET. (b) O 1s spectra of the modulated MOFs before and after the adsorption of PIR and KET. Dots and full lines represent the raw intensity data and the deconvolution fitting intensities, respectively. (c) N 1s spectra of the modulated MOFs before and after the adsorption of PIR.

Table S1. Adsorption kinetic constants for the adsorption of PIR by MIL-126-1AA, MIL-126-5AA and MIL-126-10AA at different initial concentrations (C_i) of PIR.

	MIL-126-1AA			MIL-126-5AA			MIL-126-10AA		
				Pseudo-first-order kinetic model					
C_i (mg g^{-1})	q_e (mg g^{-1})	K_1 (min^{-1})	R^2	q_e (mg g^{-1})	K_1 (min^{-1})	R^2	q_e (mg g^{-1})	K_1 (min^{-1})	R^2
20	77.70	5.110×10^{-3}	0.9550	86.16	6.970×10^{-3}	0.8973	68.46	6.890×10^{-3}	0.9494
10	66.67	6.770×10^{-3}	0.8440	110.2	6.420×10^{-3}	0.9765	66.86	5.070×10^{-3}	0.9731
5	0.9082	0.02299	0.6562	10.98	4.460×10^{-3}	0.9121	8.907	9.410×10^{-3}	0.7902
				Pseudo-second-order kinetic model					
C_i (mg g^{-1})	q_e (mg g^{-1})	K_2 (g mg^{-1} min^{-1})	R^2	q_e (mg g^{-1})	K_2 (g mg^{-1} min^{-1})	R^2	q_e (mg g^{-1})	K_2 (g mg^{-1} min^{-1})	R^2
20	97.47	1.214×10^{-4}	0.9990	65.53	7.765×10^{-4}	0.9951	70.22	3.007×10^{-4}	0.9999
10	52.69	8.438×10^{-4}	0.9975	31.82	3.470×10^{-3}	0.9865	40.39	1.820×10^{-3}	0.9856
5	27.43	6.357×10^{-4}	0.9996	17.81	0.02727	0.9965	21.01	0.01020	0.9869

Table S2. Adsorption kinetic constants for the adsorption of KET by MIL-126-1AA, MIL-126-5AA and MIL-126-10AA at different initial concentrations (C_i) of KET.

	MIL-126-1AA			MIL-126-5AA			MIL-126-10AA		
	Pseudo-first-order kinetic model								
C_i (mg g^{-1})	q_e (mg g^{-1})	K_1 (min^{-1})	R^2	q_e (mg g^{-1})	K_1 (min^{-1})	R^2	q_e (mg g^{-1})	K_1 (min^{-1})	R^2
35	45.79	4.580×10^{-3}	0.7566	3.890×10^{-3}	98.22	0.9765	110.1	4.200×10^{-3}	0.9731
15	14.59	3.050×10^{-3}	0.6088	64.07	2.090×10^{-3}	0.9251	53.50	3.110×10^{-3}	0.9344
5	4.236	2.880×10^{-3}	0.5643	28.06	4.270×10^{-3}	0.9788	3.339	5.410×10^{-3}	0.9807
	Pseudo-second-order kinetic model								
C_i (mg g^{-1})	q_e (mg g^{-1})	K_2 (g mg^{-1} min^{-1})	R^2	q_e (mg g^{-1})	K_2 (g mg^{-1} min^{-1})	R^2	q_e (mg g^{-1})	K_2 (g mg^{-1} min^{-1})	R^2
35	166.7	1.780×10^{-6}	0.9998	132.9	2.518×10^{-5}	0.9908	150.6	1.739×10^{-5}	0.9919
15	78.50	9.870×10^{-6}	0.9995	76.63	3.411×10^{-4}	0.9993	76.10	1.524×10^{-4}	0.9969
5	26.55	4.030×10^{-4}	0.9991	34.92	8.401×10^{-3}	0.9941	30.97	6.957×10^{-3}	0.9981

Table S3. Adsorption isotherm constants for the adsorption of PIR and KET by MIL-126-1AA, MIL-126-5AA and MIL-126-10AA.

	Ketoprofen (KET)			Piroxicam (PIR)		
Adsorbent	MIL-126-1AA	MIL-126-5AA	MIL-126-10AA	MIL-126-1AA	MIL-126-5AA	MIL-126-10AA
			Langmuir model			
q_{max} (mg g^{-1})	452.5	219.8	229.4	209.7	104.6	127.9
K_L (mg^{-1})	0.2110	0.3020	0.1360	0.2820	0.5680	0.1520
R^2	0.9970	0.9907	0.9658	0.9961	0.9958	0.9755
			Freundlich model			
K_F (mg g^{-1})	73.12	31.97	47.57	51.81	15.97	30.27
n	1.460	1.820	1.990	1.660	1.520	2.160
R^2	0.9662	0.8608	0.9393	0.9485	0.9552	0.9592

Table S4. Maximum adsorption capacities of various adsorbents for PIR and KET in the literature.

Pollutant	Adsorbent	Maximum adsorption capacity (mg g^{-1})	Reference
PIR	Activated carbon, PBFG4	138	Calisto et al., 2015
	Primary paper mill sludge, PS800-150	5.82	Samghouli et al., 2022
	Treated artichoke waste	20.33	Chenthamara et al., 2022
	Zinc chloride activated carbon	6.08	Feng et al., 2019
	MIL-126-1AA	209.7	This work
	MIL-126-5AA	104.6	This work
	MIL-126-10AA	127.9	This work
KET	Zirconium-based MOF, UiO-66-NH_2	186	Feng et al., 2019
	Multi-walled carbon nanotube (MWCNT)/UiO-66-NH_2 composite	233	Han et al., 2023
	MOF/Graphite oxide composite, HKUST-1@15%GO	76.98	2018 et al., 2018
	Carbon nanotubes modified with ionic liquids, CNT-IL1	207.65	Lawal et al., 2018
	MOF/Graphene oxide composite, MIL-101_GnO (3%)	140	Sarker et al., 2018
	$NiFe_2O_4$/Activated carbon composite	97.75	Fröhlich et al., 2019
	Activated carbon prepared from winery wastes	146.4	Sellaoui et al., 2021
	Chitosan/MOF composite foams, CSF@UiO-66	209.7	Chen et al., 2022

MOF/Layered double hydroxide composite, ZIF-8@NiAl-LDHs	30.3	Wang et al., 2020
Chromium-based MOF, PCN-333 (Cr)	387.6	Zhang et al., 2022
MIL-126-1AA	452.5	This work
MIL-126-5AA	219.8	This work
MIL-126-10AA	229.4	This work

Table S5. The results of the thermodynamic experiments for the adsorption of PIR and KET by MIL-126-1AA, MIL-126-5AA and MIL-126-10AA.

Pollutants	Adsorbents	T (°C)	Parameters		
			ΔG (kJ mol^{-1})	ΔH (kJ mol^{-1})	ΔS (J mol^{-1} k^{-1})
PIR	MIL-126-1AA	25	–9.383	18.78	94.50
		35	–10.33		
		45	–11.27		
	MIL-126-5AA	25	–5.966	10.97	56.83
		35	–6.534		
		45	–7.102		
	MIL-126-10AA	25	–6.114	22.96	97.55
		35	–7.089		
		45	–8.065		
KET	MIL-126-1AA	25	–26.85	1.310	215.5
		35	–65.06		
		45	–67.22		
	MIL-126-5AA	25	–63.11	1.092	215.4
		35	–65.26		
		45	–67.41		
	MIL-126-10AA	25	–89.87	1.428	306.4
		35	–92.94		
		45	–96.00		

Chapter 4 Paper 3-Tunning bismuth metal-organic framework topology for enhanced photocatalytic NO oxidation

Chen Wu, Min Zhou, Jincheng Mu, Yu Huang, Xueying Wang, Pui-Yu Ho, Can Yang, Chi-Fai Leung, Wing-Kei Ho

Abstract

Precise topological-structural control over bismuth-based metal–organic frameworks (Bi-MOFs) is hampered by the challenge of balancing thermodynamics and kinetics. We achieved such balance in three well-defined Bi-MOFs with crystalline, semi-crystalline, and amorphous topologies *via* a straightforward secondary building unit approach in bismuth-2-aminoterephthalic acid (Bi-BDC-NH_2). The structure of Bi-BDC-NH_2 was confirmed by single-crystal X-ray diffraction (XRD) to consist of BiO_9 nodes. The amount of 2-aminoterephthalic acid was varied to modulate the topology *via* competitive complexation and thus control the thermodynamic and kinetic nucleation products. Through regulating the ligand-to-metal ratio of H_2BDC-NH_2 to Bi, an appropriate balance of the thermodynamic-vs-kinetic structural 'trade-off' was achieved. The fine topologies of Bi-MOFs were determined by single-crystal XRD, high-resolution transmission electron microscopy, X-ray photoelectron spectroscopy, and X-ray absorption fine structure. Further photocatalytic NO oxidation experiments based on different topological-structural Bi-MOFs demonstrate that the amorphization improves the photogenerated charge separation efficiency and adsorption and activation of O_2. This work offers a guide in complex topological-structural control, which is conducive for those to develop highly efficient MOFs-based photocatalysts.

1. Introduction

Metal–organic frameworks (MOFs) are porous nanostructures formed through the self-assembly of metal ions and organic ligands (Bara et al., 2019; Long et al., 2009; Yaghi et al., 2003 and Zhou et al., 2012). The diversity in their lattice structures, elemental compositions, and organic linkers presents opportunities for numerous material applications (Shi et al., 2023; Lin et al., 2022; Liang et al., 2023; Zelepukin et al., 2022 and Marimuthu et al., 2022). Despite the accessibility of diverse MOF architectures, their synthesis with precise topological control is hampered by the complexities of phase formation (Xing et al., 2019; Wu and Au, 2024 and Liu et al., 2005). MOFs can be stabilised by pairing hard acids with hard bases or soft acids with soft bases, while borderline acids, with intermediate charge densities, can interact with various Lewis bases following the hard and soft acids and bases principle (Liu et al., 2005; Wang et al., 2020 and Huang et al., 2024). Bi-HHTP (HHTP = 2,3,6,7,10,11-hexahydroxytriphenylene), a highly conductive Bi-based MOF (Zhao et al., 2024), is predominantly constructed from bridging HHTP ligands and distorted BiO_4 nodes, with Bi–O bond lengths of ~2.05 Å, exemplifying the borderline acid–soft base interaction. Despite the potential of Bi^{3+} cations in MOF synthesis, few frameworks exhibiting varying topologies have been developed using Bi^{3+}. This limitation is attributable to the variable coordination numbers of Bi, from 3 to 10, and its susceptibility to hydrolysis and polarisation (Tregnago et al., 2024; Hu et al., 2023; Yang et al., 2024 and Inge et al., 2016), which complicate synthesis and the predictable formation of desired structures (Sadler et al., 1999). Therefore, the manufacture and utilisation of Bi-MOFs with tuneable topology depends on balancing a structural ‘trade-off’ by controlling the ratio between the metal ion and ligand.

The secondary building unit (SBU) approach can potentially resolve this trade-off in the design of stable Bi-MOFs with controlled topology. In the SBU model of nucleation and growth, metal nodes and organic linkers serve as vertices and edges, respectively, connecting and stabilising the metal nodes within a defined geometry, promoting a rigid framework (Inge et al., 2016). SBUs are formed through coordination chemistry between metal nodes and organic linkers, subsequently aggregating into a critical nucleus *via* coordination linkages. This aggregation is influenced by thermodynamic and kinetic factors, which determine the robustness of the metal–ligand bonds (Eddaoudi et al., 2001). Key influences include the nature of the coordination bonds, the structural features of the framework, interactions between frameworks, and the coordination environment (Férey et al., 2000; Carpenter et al., 2023; Usman et al., 2020; Liu et al., 2021 and Van Vleet et al., 2018). The ligand-to-metal (L/M) ratio modulates both the nucleation kinetics and the species distribution (Giri et al., 2022; Lutsko et al., 2020; Shaw et al., 2024 and Wu et al., 2019), underscoring the significance of precise control in Bi-MOF synthesis. For instance, in synthesising zeolitic imidazolate frameworks (ZIFs), increasing the L/M ratio from 1 to 40 significantly accelerates the formation of ZIF-67 (Lv et al., 2022). This results in the generation of more oligomeric nuclei, and consequently smaller average particle sizes of ZIF-67, due to the finite concentration of Co^{2+} in the solution. The formation of stable oligomeric nuclei necessitates the bridging of individual monomeric complexes through 2-methylimidazole-rich complexes, which accelerates oligomerisation. Higher L/M ratios inhibit the formation of the 2-methylimidazole-rich complex $Co(2\text{-mlm})_3OR$ despite an increased contribution from $Co(2\text{-mlm})_4$, hindering further nucleus and particle formation. Consequently, the nucleation rate increases with initial increases in the L/M ratio until reaching a saturation point, where the rate stabilises.

These observations suggest a promising method for synthesising topologically diverse Bi-MOFs by regulating the L/M ratio. However, the underlying mechanisms remain uncertain and no standardised synthesis protocol exists. Herein, we synthesise three chemically stable Bi-MOFs with distinct topologies by varying the L/M ratio, following a straightforward SBU approach. All three Bi-MOFs are composed of Bi-BDC-NH_2 but exhibit different crystalline, semi-crystalline, and amorphous phases, characterised using single-crystal X-ray diffraction (XRD) and high-resolution transmission electron microscopy (HRTEM), marking the systematic synthesis of Bi-MOFs with varying topologies to the best of our knowledge. X-ray photoelectron spectroscopy (XPS) and X-ray absorption fine structure (XAFS) provide further chemical-structure information, showing that the crystalline Bi-MOF (C-MOF) has Bi–O bonding features, whereas the semi-crystalline Bi-MOF (S-MOF) has Bi–O and partial Bi–N bonding, and the amorphous phase (A-MOF) exhibits numerous unique structural features with Bi–O and Bi–N bonding. The rich variety of active $Bi^{(3-x)+}$ sites and amorphisation shall endow the Bi-MOFs with superior photocatalytic performance for nitric oxide (NO) oxidation under ambient conditions. This reaction, driven by the stringent environmental regulations, has received considerable attention given its potential for efficient dilute NO removal (Guo et al., 2023). Well-designed catalytic A-MOF improves the photogenerated charge SEPARATION efficiency and adsorption and activation of O_2, showing enhanced efficiency and stability in air purification.

2. Results and Discussion

The fine structure of MOFs synthesised using a Bi^{3+} metal source and 2-aminoterephthalic acid (H_2BDC-NH_2) ligand was first analysed using Single-crystal XRD. As shown in Table S1, the Bi-BDC-NH_2 crystalises in space group P-1 with a non-interpenetrated structure constructed from binuclear, ligand-bridged $\{Bi_1$-$Bi_2\}$ centres. The bismuth centre is coordinated to nine oxygens to form a BiO_9 unit, and a pair of BiO_9 units bridged *via* oxygens and Bi^{3+} possesses a holodirected coordination environment Figure S1a (Thirumurugan et al., 2010). Each bismuth is overall coordinated to three H_2BDC-NH_2 linkers in bidentate mode, one H_2BDC-NH_2 linker in monodentate mode, and two water molecules, respectively, to form an irregular dodecahedron configuration (Figure S1c). TEA promotes the deprotonation process of the $H_2BDC\text{-}NH_2$ ligands. The strong base TEA (pKa = 11.01) can completely deprotonate the $H_2BDC\text{-}NH_2$ ligands to form $BDC\text{-}NH_2^{2-}$. The metal ions exhibit a poor binding affinity for TEA. The fully "activated" $BDC\text{-}NH_2^{2-}$ ligands can coordinate with Bi ions, while TEA does not form coordination with the metal clusters but remains free in the voids of the crystal. It results in a three-dimensional porous structure, which is very similar to that of MOF-31 (Kim et al., 2001 and Zhang et al., 2024). Crystallographically, the $H_2BDC\text{-}NH_2$ linker is coordinated to a bismuth centre as a bidentate ligand *via* two oxygens, one of which coordinates to another bismuth centre to form an SBU (Figure S1d).

Bi-MOFs with different topologies are synthesised solvothermally with a mixed solvent of dimethylformamide (DMF) and ethanol, adjusting the L/M ratio to control the nucleation rate, at 120 °C for 24 h (Figure 1a). In the reaction medium, higher ligand concentration increases the viscosity *via* π-π stacking interactions, promoting a crystalline topology (Liu et al., 2024). The increased viscosity hinders Bi^{3+} diffusion, favouring the coordination of –COOH and Bi^{3+}, whereas the $–NH_2$ groups remain non-coordinated. This is because the protons in solution resulting from increased ligand concentration protonate $–NH_2$ groups into $–NH_3^+$, hindering their coordination with metal ions (Zhu et al., 2024). Furthermore, the pK_a of –COOH is lower than that of $–NH_2$, facilitating deprotonation of –COOH to form $–COO^–$, which coordinates with Bi^{3+} to create polynuclear clusters acting as SBUs (Wang et al., 2021). Therefore, increasing the $H_2BDC\text{-}NH_2$ concentration promotes the formation of thermodynamically stable products (with the lowest Gibbs free energy), corresponding to the crystalline topology (Zhu et al., 2017). When the L/M ratio is reduced, the coordination reactions simultaneously involve both terminal and bridging modes, providing versatility in the ligand's interaction with metal ions (Rao et al., 2004). Borderline Lewis-acidic Bi^{3+} exhibits an affinity for $-NH_2$ according to the principle of hard and soft (Lewis) acids and bases theory (HSAB) (Sharifzadeh et al., 2023), thus providing coordination sites. This interaction allows oxygen from –COOH to bond with Bi^{3+}, forming O–Bi–N bonds and increasing the complexity of the coordination network. This unusual phenomenon was also observed in other borderline Lewis acids that coordinate with $-NH_2$ in the metal-$H_2BDC-NH_2$ system, such as Zn(II) (Saha et al., 2017) and Mn(II) (Zhang et al., 2008) based on the principle that carboxylate groups, as ligands, can adopt terminal (monodentate and bidentate) and bridging (mainly anti–anti, anti–syn, and syn–syn) coordination modes. Therefore, the excess Bi^{3+} resulting from a decreased L/M ratio disrupts the long-range order of the coordination network, resulting in irregular coordination patterns and kinetic amorphous products.

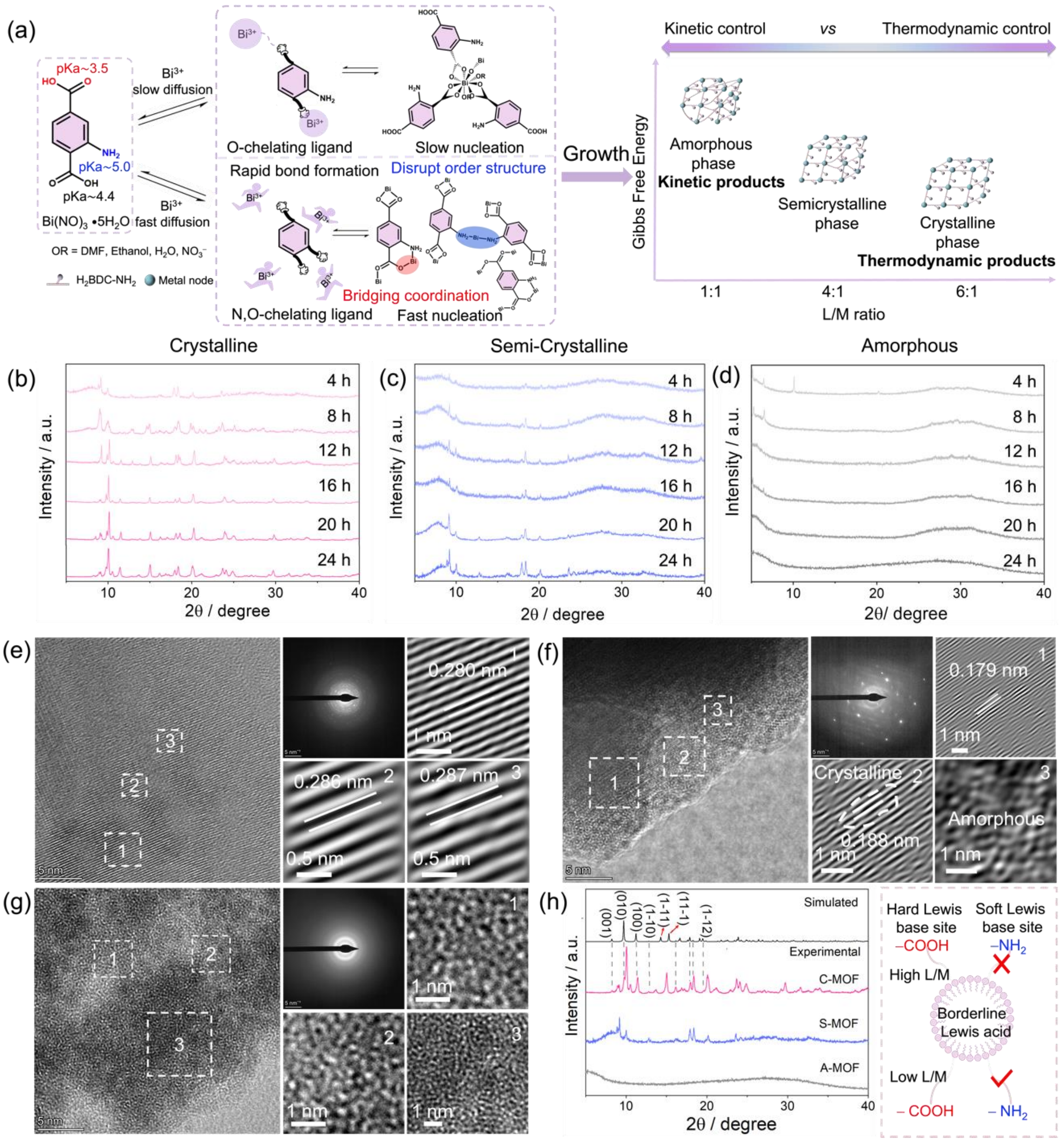

Figure 1. (a) Possible nucleation mechanisms of Bi-MOF at high and low L/M ratios and Gibbs free energy of formation products. Experimental XRD patterns at different times for (b) C-MOF, (c) S-MOF, and (d) A-MOF. Left: HRTEM images; right: SAED pattern, followed by three enlarged HRTEM images of the white dashed boxes of (e) C-MOF, (f) S-MOF, and (g) A-MOF. (h) Top to bottom: predicted PXRD pattern of Bi-BDC-NH_2; experimental PXRD patterns of as-synthesised C-MOF, S-MOF, and A-MOF.

Time-resolved XRD (Figures 1b-d) shows that at high ligand concentrations, S-MOF is produced within 4 h, whereas the crystallinity increases after 12 h. At medium ligand concentrations, the Bi-MOFs exhibit primarily amorphous peaks within the first 8 h, with sharp peaks emerging at 12 h and remaining stable thereafter. Conversely, at low precursor concentrations, the Bi-MOF shows very low crystallinity at 4 h, but three sharp peaks of A-MOF at 2θ = 5.3° and 6.3° indicate the presence of certain crystalline phases, while the peak at 11° is likely associated with hydrated bismuth oxide nitrate hydroxide ($Bi_6O_6(OH)_2(NO_3)_4 \cdot 2H_2O$), a member of the basic bismuth nitrate compounds (Ma et al., 2018). At this stage, the nitrate (NO_3^-) ions and water (H_2O) from the bismuth source still coordinate with Bi^{3+}, which is crucial for maintaining the structural integrity of the MOF. The $H_2BDC\text{-}NH_2$ gradually replace the H_2O and NO_3^- as the reaction progresses due to their stronger coordination ability with the metal ions. After 20 h, all the sharp peaks disappear, forming a completely amorphous phase. To test the hypothesis that high L/M ratios result in diverse topologies, we investigated the morphological and phase differences of the as-synthesised materials using scanning electron microscopy (SEM), TEM, and XRD. The Bi-MOFs synthesised at high L/M ratios exhibit a bulk morphology, with a crystallite size of approximately 900 nm. The slower nucleation rate allows for more extended crystal growth periods, leading to well-defined structures (Wu et al., 2024). While those produced at low L/M ratios demonstrate spherical and densely packed growth structures with a crystallite size of about 50 nm. In this case, the quick formation of numerous nucleation sites restricts the time available for crystal growth (Figure S2) (Cravillon et al., 2009). At intermediate L/M ratios, spherical structures associated with low-L/M products and bulk structures linked to high-L/M products coexist, consistent with the TEM results (Figures S3 and S4). The lattice fringes of the high-L/M product exhibit an ordered alignment, indicating high crystallinity (Figure 1e). Selected-area electron diffraction (SAED) and XRD patterns (Figure 1h) exhibit sharp, well-defined diffraction peaks, confirming the high crystallinity of the L/M product. The XRD peaks of C-MOF at 2θ = 8.2°, 9.7°, 11.2°, 12.8°, 16.1°, 17.8°, 18.2°, and 19.5°

correspond closely to the simulated peaks. Slight discrepancies might be attributable to solvent evaporation from the C-MOF powder and symmetry breaking, as the powder XRD (PXRD) studies utilised dried powder, whereas the single-crystal sample was solvated (Wu et al., 2023).

Additionally, C-MOF may have mixed with the starting materials and/or other byproducts, potentially explaining the additional minor peaks. In Figure 1, the magnified HRTEM images in the white box indicate that the crystalline structure has lattice spacings averaging ~0.284 nm, according to fast Fourier transform image analysis. Three magnified HRTEM images (Figure 1f) illustrate that the crystalline regions (areas 1 and 2) are highly ordered, while the amorphous region (area 3) lacks long-range order, with entangled chains indicative of disorder. This suggests that the synthesised Bi-MOFs possess a semi-crystalline character, being partially crystalline and partially amorphous. This is consistent with the XRD results, showing broader peaks due to weak crystallinity, namely S-MOF. In contrast, the HRTEM image of the low-L/M product (Figure 1g) reveals no crystallinity whatsoever. SAED patterns corroborate this observation, showing no distinct diffraction rings, indicating that the low-L/M product lacks long-range order, characterising it as A-MOF. These findings are consistent with the XRD patterns, with broad, diffuse peaks due to the non-periodic atomic arrangement, resulting in scattering manifesting as wide ‘humps’. Such broad peaks typically suggest an amorphous region of the sample, indicating that the structure lacks a regular lattice arrangement, corroborating the amorphousness of A-MOF.

The chemical structure and composition of the as-obtained Bi-MOFs with different topologies were analysed by Fourier-transform infrared (FTIR) spectroscopy and XPS (Figures S5, S6, and 2a-c). For $H_2BDC\text{-}NH_2$, the peaks at 3507 and 3394 cm^{-1} are attributed to the stretching of N–H bonds in NH_2, while the large peak at 2900 cm^{-1} corresponds to –OH group stretching. Two clear sharp peaks at 3463 and 3333 cm^{-1} are assigned to asymmetric and symmetric vibrations of NH_2 in C-MOF, confirming that NH_2 is not coordinated with Bi^{3+}. Unlike in C-MOF, the broadened and weakened characteristic peak of $–NH_2$ in S-MOF may indicate multiple overlapping absorptions for complex mixtures or compounds, suggesting a lower concentration of $–NH_2$ in S-MOF. In A-MOF, the sharp peaks of $–NH_2$ are weak and become broader, indicating that $–NH_2$ bonds with Bi^{3+} *via* Bi–N bonds. The stretching vibration peak of $–NH_2$ in H_2BDC-NH_2 disappears in the as-synthesised Bi-MOFs, suggesting the formation of coordination bonds between Bi^{3+} and $–NH_2$. The characteristic absorption peaks at 1664, 1620, and 1359 cm^{-1} correspond to the C=O stretching vibrations, asymmetric, and symmetric vibrations of C–O bonds, respectively. These vibrations mainly originate from the H_2BDC-NH_2 linkers.

The survey spectrum (Figure S6) indicates the presence of Bi, C, N, and O in the as-synthesised Bi-MOFs, which is consistent with the result of energy-dispersive X-ray (EDX) spectroscopy (Figure S7). For C-MOF, Bi 4f displays two contributions, corresponding to Bi $4f_{5/2}$ and Bi $4f_{7/2}$, with binding energies of 165.0 and 159.6 eV, respectively (Figures 2a and S8). For S-MOF, primary peaks at 164.8 and 159.4 eV are attributed to Bi^{3+}, while the additional peaks at lower binding energies of 163.4 and 158.2 eV are associated with a lower valence state, $Bi^{(3-x)+}$, indicating oxygen vacancies (Wang et al., 2022). A-MOF has a significantly higher concentration of $Bi^{(3-x)+}$, with binding energies at 163.9 and 158.5 eV. For C-MOF, the N 1s spectrum is divided into three peaks at 398.6 eV (C–N), 399.4 eV ($–NH_2$), and 401.9 eV ($–NH_3^+$), indicating that $–NH_2$ is not bonded to Bi ions (Figure 2b). For A-MOF, the characteristic peak for $–NH_2$ disappears and only two peaks corresponding to Bi–N and C–N interactions are observed. The N 1s spectrum of S-MOF displays a complex coordination environment, reflecting the combined features of A-MOF and C-MOF. The O 1s spectrum for the as-synthesised Bi-MOFs contains peaks of C–O, O–C=O, and Bi–O bonds

(Figure 2c). The content of Bi–O bonds increases as the degree of crystallinity decreases, consistent with the thermogravimetric analysis (TGA; Figure S9).

The coordination environment in Bi-MOFs was analysed by X-ray absorption spectroscopy. In the X-ray absorption near-edge structure (XANES) spectrum of the Bi L_3-edge, the absorption edge of the Bi-MOFs is located near that of Bi_2O_3, slightly shifted toward the Bi foil (Figure 2d). This suggests that the average valence state of Bi in the Bi-MOFs is $(3-x)^+$, indicating mixed valence states. This is consistent with the Bi 4f XPS spectrum. Fourier-transform EXAFS (FT-EXAFS) spectra of Bi-MOFs and the reference Bi_2O_3 and Bi foil were plotted to obtain structural information. The EXAFS of the R space in Bi_2O_3 shows the main peak located at ~1.66 Å, whereas the main peak in A-MOF is slightly shifted to ~1.63 Å, suggesting the presence of Bi–O and Bi–N bonds in Bi-MOFs (Wang et al., 2023). In contrast, no oscillations related to Bi–Bi coordination are observed near 3.0 Å, suggesting no Bi^0 formation. Wavelet transform EXAFS (WT-EXAFS) was performed with high resolution in k space (Figure 2f). Compared with Bi_2O_3, the distinct bicentric characteristic of Bi-MOFs can be ascribed to the Bi–N and Bi–O bond signals (Wang et al., 2024). No Bi–Bi bonds are observed in the Bi-MOFs, revealing that Bi^{3+} remains coordinated with the ligands and does not aggregate into particles.

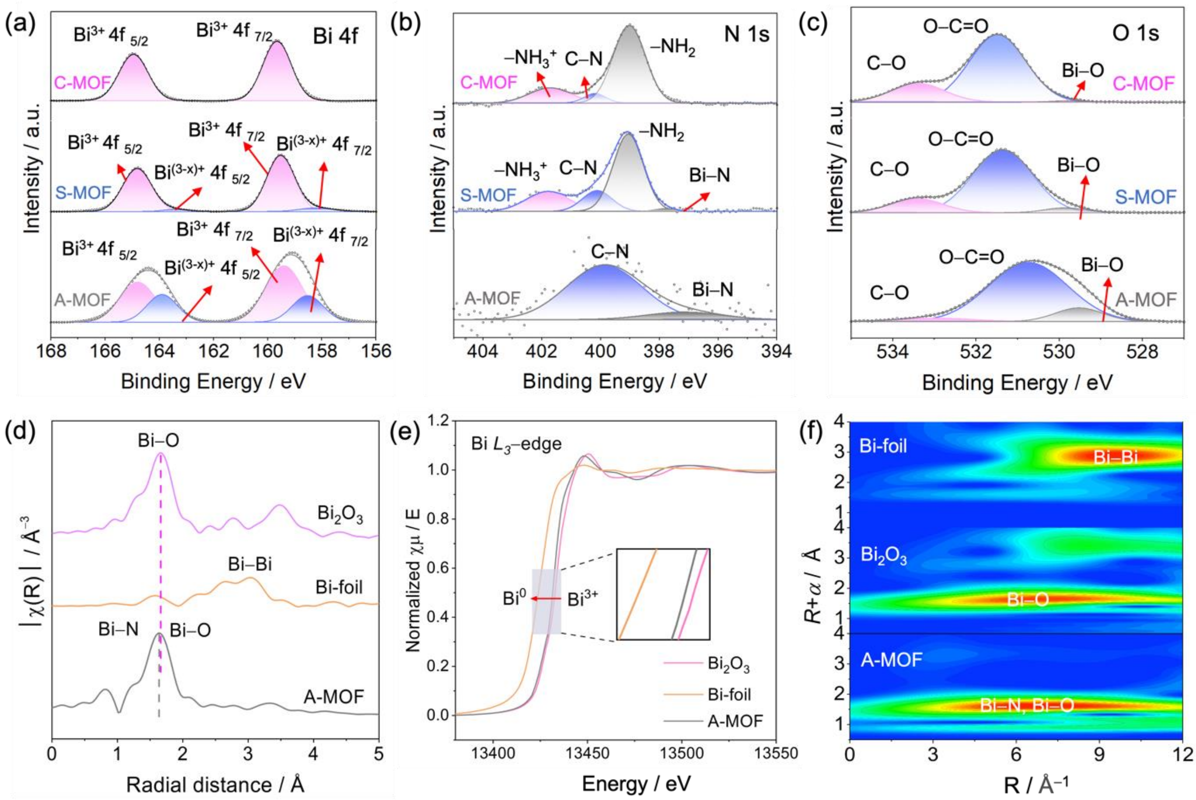

Figure 2. High-resolution XPS spectra of Bi 4f (a), N 1s (b), and O 1s (c) for C-MOF, S-MOF, and A-MOF. Dots and full lines represent the raw intensity data and the deconvolution fitting intensities, respectively. Bi L_3-edge XANES (d), EXAFS spectra (e), and WT-EXAFS (f) of Bi-MOFs (A-MOF) and reference samples of Bi foil and Bi_2O_3.

The optical absorption properties and electronic structure of the as-synthesised Bi-MOFs were measured by UV–visible diffuse reflectance spectroscopy (UV–vis DRS). The absorption edge of C-MOF is located at 460 nm, with an absorption tail extending to 750 nm (Figure 3a). The S-MOF and A-MOF absorption edges are at 525 nm and 650 nm, respectively, indicating significantly enhanced visible-light absorption than C-MOF. This enhancement corresponds well with the observed colour change of the as-synthesised Bi-MOFs from light yellow to deep orange. Two prominent peaks at 265 nm and 350 nm are attributed to Bi-oxo clusters and $–NH_2$ groups grafted onto the BDC linkers (Liu et al., 2023). For A-MOF, the broadened peaks attributed to the Bi-oxo clusters and $–NH_2$ groups reflect the irregular arrangement of Bi-oxo and ligands characteristic of the amorphous structure.

The shoulder peak at 480 nm is attributed to electron transfer from the $–NH_2$ ligands to the metal centre on the linker, illustrating the electronic interactions within the as-synthesised Bi-MOFs. The calculated bandgaps for C-MOF, S-MOF, and A-MOF are approximately 2.78, 2.35, and 2.05 eV, respectively (Figure 3b). To investigate the electronic structure, Mott–Schottky plots were used to analyse the conduction band (CB) and valence band (VB) positions of the as-synthesised MOFs (Figure 3c). The CB potentials for C-MOF, S-MOF, and A-MOF are −0.17, −0.25, and −0.36 V (vs. NHE), respectively. Based on the bandgaps obtained from UV–vis DRS, the VB positions for C-MOF, S-MOF, and A-MOF are approximately 2.61, 2.15, and 1.69 V (vs. NHE), respectively (Figure S10).

The kinetic properties of the as-obtained Bi-MOFs were investigated using photoelectrochemical tests. The photocurrent response of A-MOF is significantly higher than those of S-MOF and C-MOF, suggesting that the photogenerated carriers are more efficiently separated over A-MOF than S-MOF or C-MOF (Figure 3d). A-MOF has the smallest radius among the electrochemical impedance spectroscopy (EIS) plots (Figure 3e), which usually implies lower electron-transfer resistance, suggesting better electron mobility. In the steady-state photoluminescence (PL) spectrum (Figure 3f), the PL intensity of A-MOF under excitation at 380 nm is significantly lower than those of S-MOF and C-MOF. This indicates the recombination suppression of photogenerated carriers in A-MOF, consistent with the photocurrent measurements. Time-resolved photoluminescence (TRPL) was conducted to determine the average fluorescence lifetimes (τ). As shown in Figure 3g, for A-MOF (τ = 1.14 ns), which is longer than for S-MOF (0.79 ns) and C-MOF (0.55 ns), suggesting the superior charge-carrier properties of A-MOF. O_2-temperature-programmed desorption (O_2-TPD) was conducted to evaluate the affinity between O_2 and Bi-MOFs. All the as-synthesised samples exhibit desorption peaks in both the mid- and high-temperature range, suggesting the presence of surface-adsorbed oxygen and lattice oxygen in the Bi-MOFs (Figure 3h). A-MOF releases surface-adsorbed oxygen at 255 °C, significantly lower than S-MOF (285 °C) and C-MOF (330 °C), indicating higher surface-oxygen affinity. In addition, the linear scanning voltammetry (LSV) curves of oxygen reduction reaction (ORR) (Figure 3i) for A-MOF exhibit a stronger positive half-wave potential. The LSV curves of Bi-MOFs measured at different rotational speeds show that A-MOF has higher rotating speed plots than C-MOF and S-MOF (Figure S11), implying the reductive ability of A-MOF. Based on the above-mentioned result and discussion, the differences in charge-separation and transport properties among the Bi-MOFs result from the electronic structure differences and may influence the photocatalytic performance.

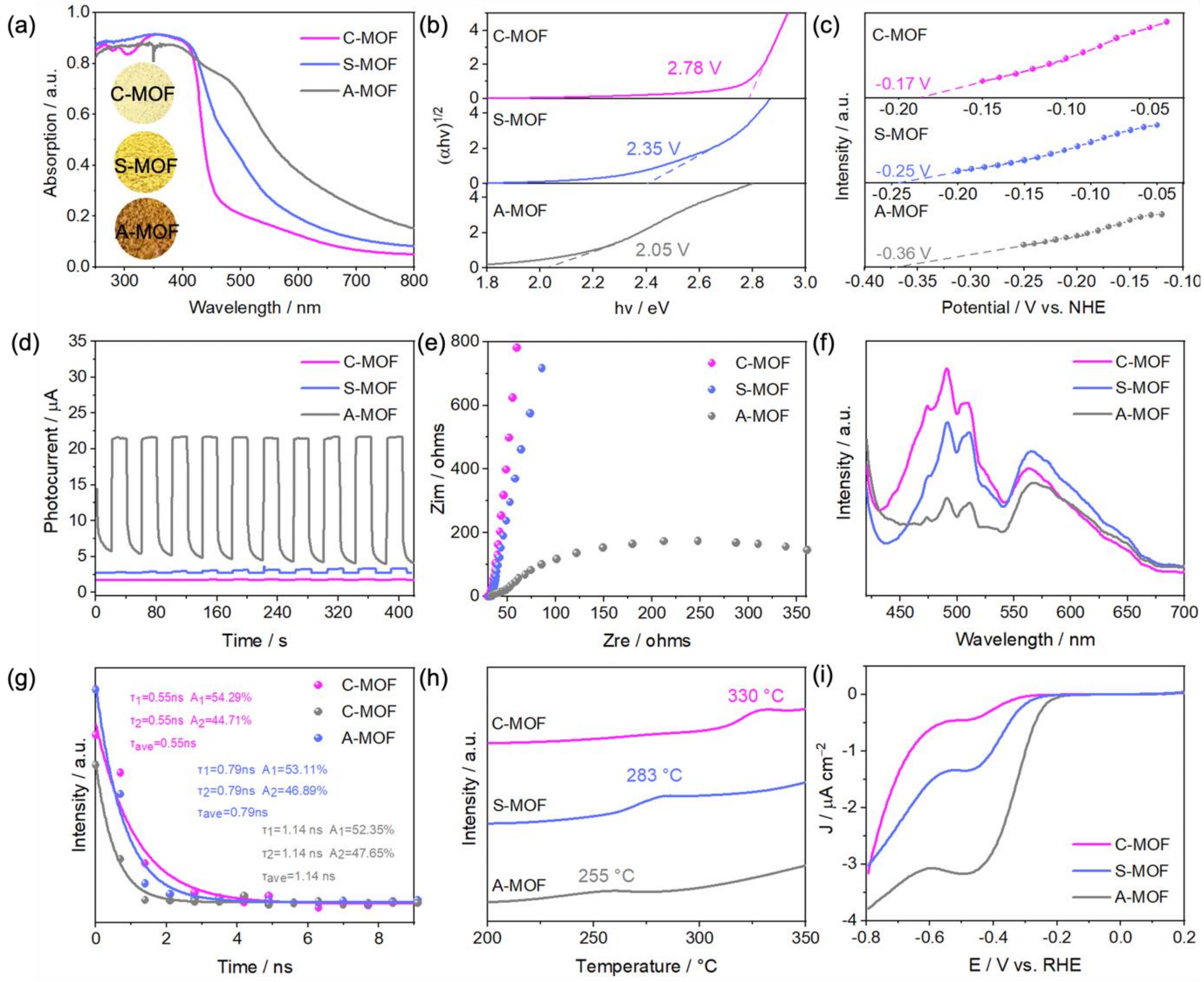

Figure 3. (a) UV–Vis DRS, (b) electronic band structures, (c) Mott–Schottky plot, (d) transient photocurrent density, (e) EIS spectra, (f) PL emission spectra, (g) emission decay

time, (h) O_2-TPD spectra, and (i) ORR tests of C-MOF, S-MOF, and A-MOF at a scanning rate of 5 mV s^{-1} and rotating speeds keep at 1600 rpm.

To elucidate the topology–catalytic performance relationship, photocatalytic NO oxidation was used as a probe reaction to evaluate the effect of electronic structure regulation over Bi-MOFs. Both S-MOF and A-MOF reached their maximum NO removal rates within 10 min under visible-light irradiation, after which the rates stabilised (Figure 4a). Except for C-MOF, A-MOF exhibits the highest NO removal rate of 73.7%, followed by S-MOF at 32.0%, likely due to concentration differences in the Bi–N active sites among the three phases. In contrast, C-MOF as the main phase typically exhibits non-smooth edge boundaries between the different crystal phases, resulting in strong scattering losses. A-MOF as an amorphous phase has also been proven to display higher electrical conductivity compared to its crystalline counterparts due to the presence of abundant defects and has demonstrated better performance in the fields of photocatalysis (Zhang et al., 2024). The fitted first-order rate constants (Figure 4b) indicate that the reaction rate of A-MOF is 5.8-fold higher than that of S-MOF. Cycle testing was conducted to estimate the stability of the optimised A-MOF photocatalyst. No obvious decrease in the NO removal rate is observed after seven cycles, and the emitted NO_2 concentration remained below 35 ppb, indicating that A-MOF is a stable photocatalyst for NO removal (Figures 4c, d, S12 and Table S2). This NO_2 concentration is significantly lower than the threshold set by the national ambient air quality standards (EPA-456/F-99-006a), i.e., 53 ppb. The active species, including e^-, h^+, $\cdot OH$, and $\cdot O_2^-$, involved in NO photooxidation were identified using $K_2Cr_2O_7$, $K_2C_2O_4$, *tert*-butyl alcohol (TBA), and *p*-benzoquinone (PBQ) as scavengers, respectively. The NO removal efficiency decreased significantly upon adding PBQ and $K_2Cr_2O_7$ to the reaction mixture, indicating that $\cdot O_2^-$ and e^- are the main active species (Figure 4e). This was corroborated by electron paramagnetic resonance (EPR; Figures 4g and S13). 5,5-Dimethyl-1-pyrroline-*N*-oxide (DMPO) was used as a spin-trapping agent for EPR detection of $\cdot O_2^-$. Under visible-light irradiation, the as-synthesised A-MOF shows a higher characteristic peak intensity of $\cdot O_2^-$ than C-MOF and S-MOF. In-situ FTIR spectroscopy was used to probe the reaction intermediates and pathway of NO photooxidation over A-MOF (Figure 4h). Nitrate species gradually accumulate on the surface of A-MOF, as revealed by peak intensities of major bidentate NO_3^- (1481, 1516, 1533, and 1549 cm^{-1}), monodentate NO_3^- (1315 cm^{-1}), bidentate NO_2^- (1407 cm^{-1}), and $\cdot O_2^-$ (1076 cm^{-1}).[35] Based on the preceding experiments, a possible photocatalytic removal pathway of NO in the A-MOF system was proposed (Figure S14). These results confirm the effectiveness of balancing thermodynamic and kinetic processes in regulating Bi-MOF topology *via* the L/M ratio, allowing modulation of the fundamental electronic structure.

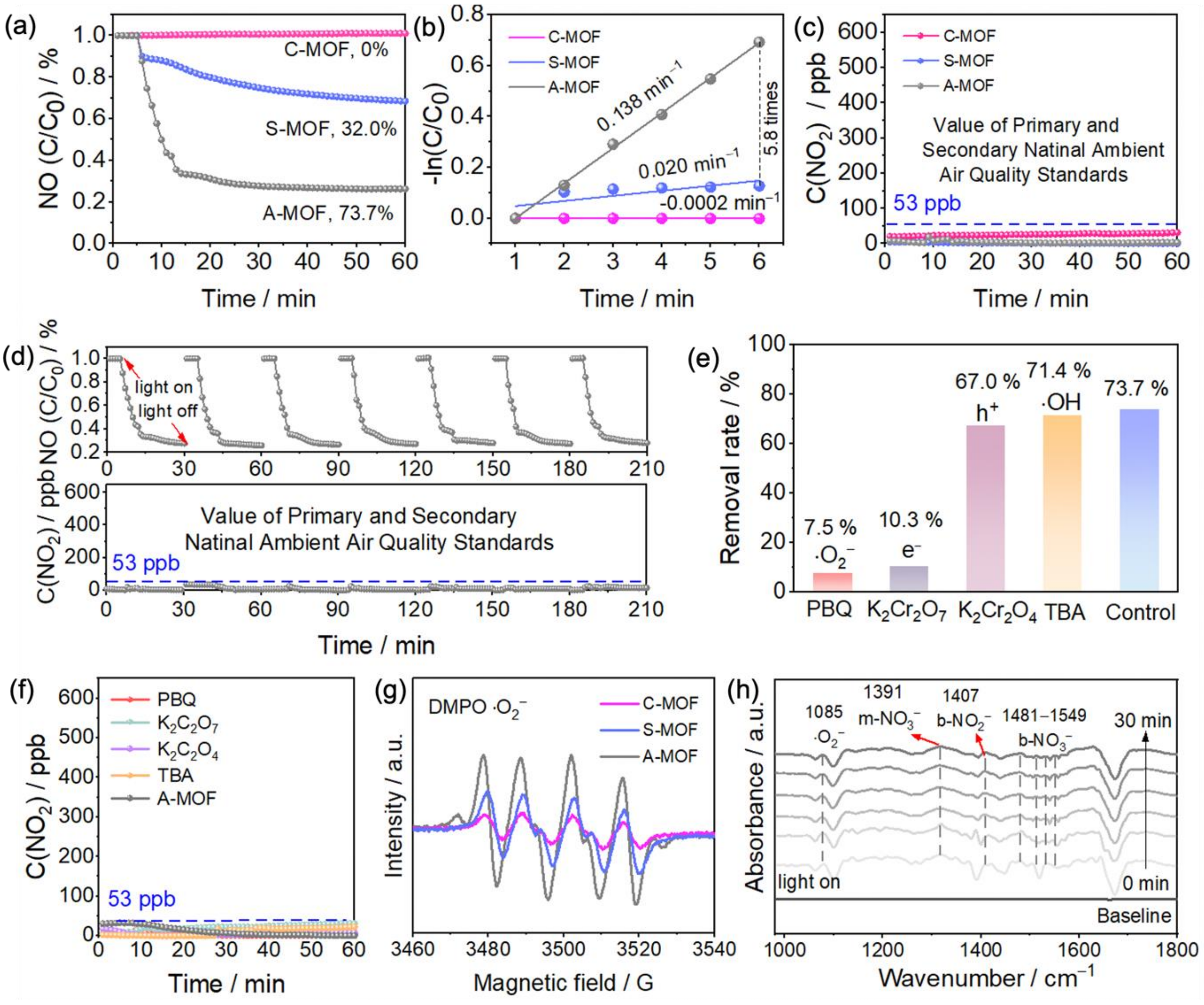

Figure 4. (a) Photocatalytic NO removal activity, (b) first-order rate constants, (c) NO_2 concentration during photocatalysis by as-synthesised C-MOF, S-MOF, and A-MOF. (d) NO removal stability tests and changes in NO_2 concentration emitted by A-MOF during seven consecutive cycles. (e) Effects of various scavengers on NO removal by A-MOF, (f) generated NO_2 intermediate in the presence of different scavengers, (g) DMPO ESR spectrum of $\cdot O_2^-$ in dimethyl sulfoxide dispersions under visible-light irradiation, (h) FTIR band distributions for NO adsorption over A-MOF.

3. Conclusion

We propose a facile SBU approach to regulate Bi-MOF topology by balancing the thermodynamic and kinetic factors affecting nucleation. Through adjusting the L/M ratio, C-MOF, S-MOF, and A-MOF with different topologies are obtained for photocatalytic NO oxidation. The L/M ratio has been identified as one of the most important criteria for topology modulation and catalytic properties. An L/M of 6/1 results in the thermodynamic product, namely the crystalline phase, whereas an L/M of 1/1 appears to generate the kinetic product, namely the amorphous phase. In addition, a coordination interaction occurs between the borderline Lewis acid Bi^{3+} and soft Lewis basic functional groups on the $H_2BDC\text{-}NH_2$ ligands. The obtained A-MOF and S-MOF with different topologies exhibit NO removal efficiencies of 74% and 32%, while C-MOF shows negligible efficiency, possibly attributable to the amorphization and different concentrations of Bi–N active sites among the three phases. This study offers guidance in designing Bi-MOF topologies by regulating the thermodynamic–kinetic trade-off, and underscores their potential in solar energy conversion for different applications.

4. Experimental section

Material: Bismuth nitrate pentahydrate (99%) and 2-aminoterephthalic acid (99%) were purchased from Oriental Chemicals and Lab. Supplies Ltd. Dimethylformamide (99.8%) was obtained from TCI, and TEA was obtained from Acros. All other reagents and solvents were commercially available and used as received.

Synthesis of single-crystal Bi-BDC-NH$_2$: Bismuth trinitrate pentahydrate (8 mg, 1.0 mmol) and 2-aminoterephthalic acid (18 mg, 1.0 mmol) were mixed in DMF (400 μL), then the mixture was sonicated for 5 min and subsequently 1 μL of TEA was added. The resulting mixture was heated at 115°C for 24 h in a long glass tube. After cooling to room temperature, yellow crystals were obtained.

Synthesis of a series of Bi-BDC-NH$_2$ with different crystallinities: Bi^{3+} (484 mg, 1.0 mmol) and ligand, with L/M ratios of 6:1, 4:1, and 1:1, were dissolved in a mixed solution of 60 mL DMF and 10 mL ethanol. The resulting mixture was heated at 120°C for 24 h. After cooling to room temperature, the products were washed with DMF, dichloromethane, and methanol, and then dried overnight under vacuum.

Characterisations: PXRD data were collected on a Bruker D8 ADVANCE powder X-ray diffractometer in Bragg–Brentano (θ/2θ) reflection mode with graphite monochromatised Cu-Kα radiation. XPS was performed using a Thermo ESCALA 250Xi X-ray photoelectron spectrometer microprobe. FTIR spectra were obtained on a PerkinElmer Frontier FTIR spectrometer (4000–530 cm^{-1}) with a universal attenuated total reflection accessory. Brunauer–Emmett–Teller nitrogen adsorption-desorption isotherm tests were performed on a Micromeritics 3Flex adsorption analyser. TGA was conducted on a PerkinElmer TGA 4000. SEM was performed on a Sigma 500 scanning electron microscope and EDX spectroscopy was performed with a Bruker XFlash 6130 detector at 10 kV. UV–Vis DRS was performed on a Varian Cary 100 Scan UV-Vis system. Bi *L*-edge analysis was performed with Si(311) crystal monochromators at the BL11B beamlines at the Shanghai Synchrotron Radiation Facility (Shanghai, China). Before the analysis at the beamline, samples were pressed into thin sheets of 1 cm diameter and sealed using Kapton tape film. XAFS spectra were recorded at room temperature using a 4-channel silicon drift detector (Bruker 5040). The XAFS spectra of the standard samples (Bi foil and Bi_2O_3) were recorded in transmission mode (fluorescence mode). The spectra were processed and analysed using Athena and Artemis software. EPR spectra were obtained from an ELEXSYS E500 spectrometer (Bruker, Germany) at room temperature. DMPO was used to capture superoxide ($\cdot O_2^-$) signals in methanol.

Crystal structure determination: Crystals suitable for XRD were mounted on a MiTeGen dual-thickness micro-mount and placed under a cold stream of nitrogen (Oxford). Single-crystal XRD measurements were recorded on a Bruker D8 VENTURE Duo FIXED-CHI X-ray diffractometer using IμS micro-focus Mo-Kα radiation ($\lambda = 0.71073$ Å) with Quazar multilayer optics. The structure was solved using *XT* 2014/5 in the APEX3 suite and refined with *SHELXL2018/3* by weighted least squares refinement on F^2 to convergence. All estimated standard deviation (e.s.d.) values (except the e.s.d. for the dihedral angle between two least-square planes) were estimated using the full covariance matrix. The X-ray crystallographic data of Bi-BDC-NH_2 have been deposited at the Cambridge Crystallographic Data Centre (CCDC), under deposition number CCDC 2358956. The data can be obtained free of charge from the CCDC (https://www.ccdc.cam.ac.uk/structures/).

Assessment of photocatalytic performance: The photocatalytic efficiencies of the prepared photocatalysts were assessed by subjecting them to a continuous-flow rectangular reactor at ambient temperature, where the photodegradation of NO was carried out at the parts per billion (ppb) level. The light source utilised in this experiment was a lamp powered by a light-emitting diode. Positioned vertically above the reactor, the lamp was approximately 6.5 cm away from the surface of the sample. To prepare the photocatalyst, approximately 0.2 g of the material was added to 20 mL of still water and subjected to ultrasonication for 30 min. Following this, the resulting suspension was transferred to a glass dish with a diameter of 11.5 cm and heated at 60°C on a heater until the water evaporated. The starting level of NO was reduced to around 650 ppb by introducing an air stream from a zero-air generator located in a compressed gas cylinder. This air stream was regulated by mass flow controllers. The NO and air streams were mixed thoroughly using a gas blender, and the overall flow rate was maintained at 500 mL min^{-1} by another mass flow controller. Once the adsorption-desorption equilibrium was established, the LED lamp (30 W) was activated for a single-cycle reaction lasting 1 h before being switched off. The removal efficiency was calculated as follows: η_{NO} (%) = $(C_0 - C)/C_0 \times 100\%$, where C_0 and C refer to the NO concentration determined before and after the reaction.

Acknowledgements

This work was supported by the General Research Fund (18300920) of the Research Grants Council, Hong Kong, Dean's Research Fund (04638 and C3688), FLASS, EdUHK and Multi-disciplinary Research Capacity Building Scheme (04A29), EdUHK, Scientific Research Startup Foundation of Jiangsu University (No. 22JDG020), and Open Project Program of the State Key Laboratory of Photocatalysis on Energy and Environment (SKLPEE-KF202310), Fuzhou University.

Supplementary Data of article 3

Table S1. Selected crystallographic data and structural refinement summary for as-synthesised Bi-BDC-NH_2.

Parameter	Bi-BDC-NH_2
Crystal system	Triclinic
Space group	*P-1*
a / Å	8.2043(10)
b / Å	10.2283(11)
c / Å	11.9378(15)
V / Å^3	883.85(18)
Z	1
Density (calcd) / g cm^{-3}	2.137
μ / mm^{-1}	10.022
Radiation type	Mo-Kα
Radiation wavelength / Å	0.71073
Temperature / K	296
F (000)	542
Restrained goodness-of-fit	1.017
Reflections collected	19299
Independent reflections	3085
R_1 [$F^2 > 2\sigma(F^2)$]	0.0331
wR_2 [F^2]	0.0767

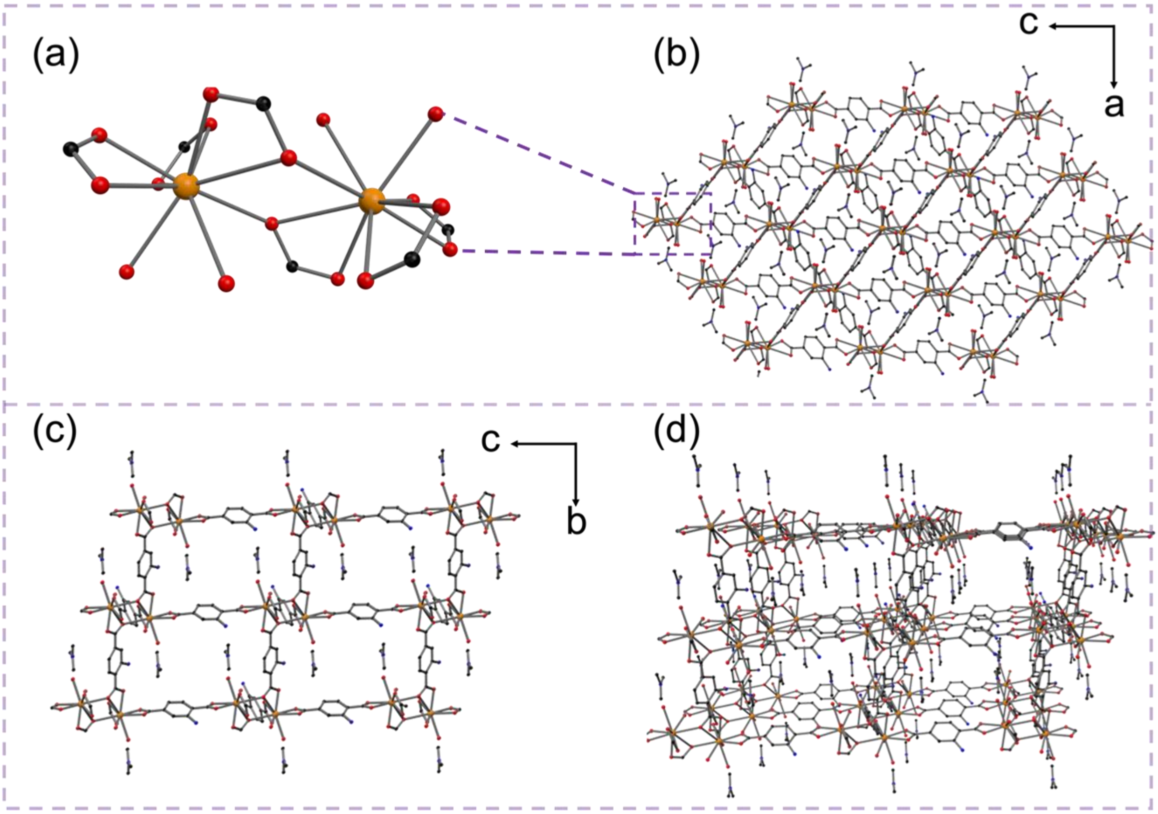

Figure S1. Single crystal structure of Bi-BDC-NH_2: Ball-and-stick models showing (a) a pair of coordinated bismuth centres forming the BiO_9 core and (b) the secondary building unit (SBU) of Bi-BDC-NH_2 viewed along the *b* axis and along the (c) *an* axis, and (d) the three-dimensional packing of Bi-BDC-NH_2. Bismuth atoms are shown in orange, carbon in grey, nitrogen in blue, and oxygen in red. Hydrogen atoms are omitted and only one of the disordered positions of the TEA molecules is shown for clarity.

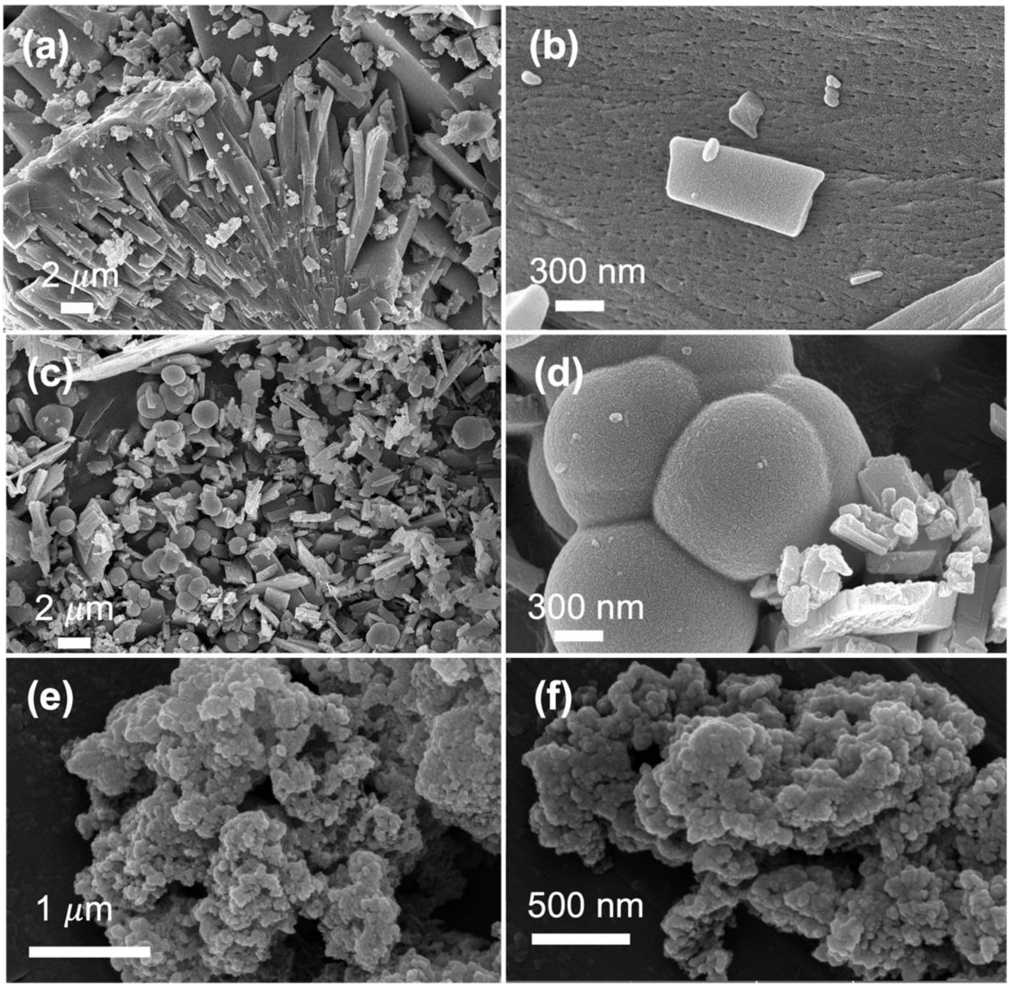

Figure S2. Scanning electron microscopy (SEM) images of (a, b) C-MOF (c, d) S-MOF, and (e, f) A-MOF at different magnifications.

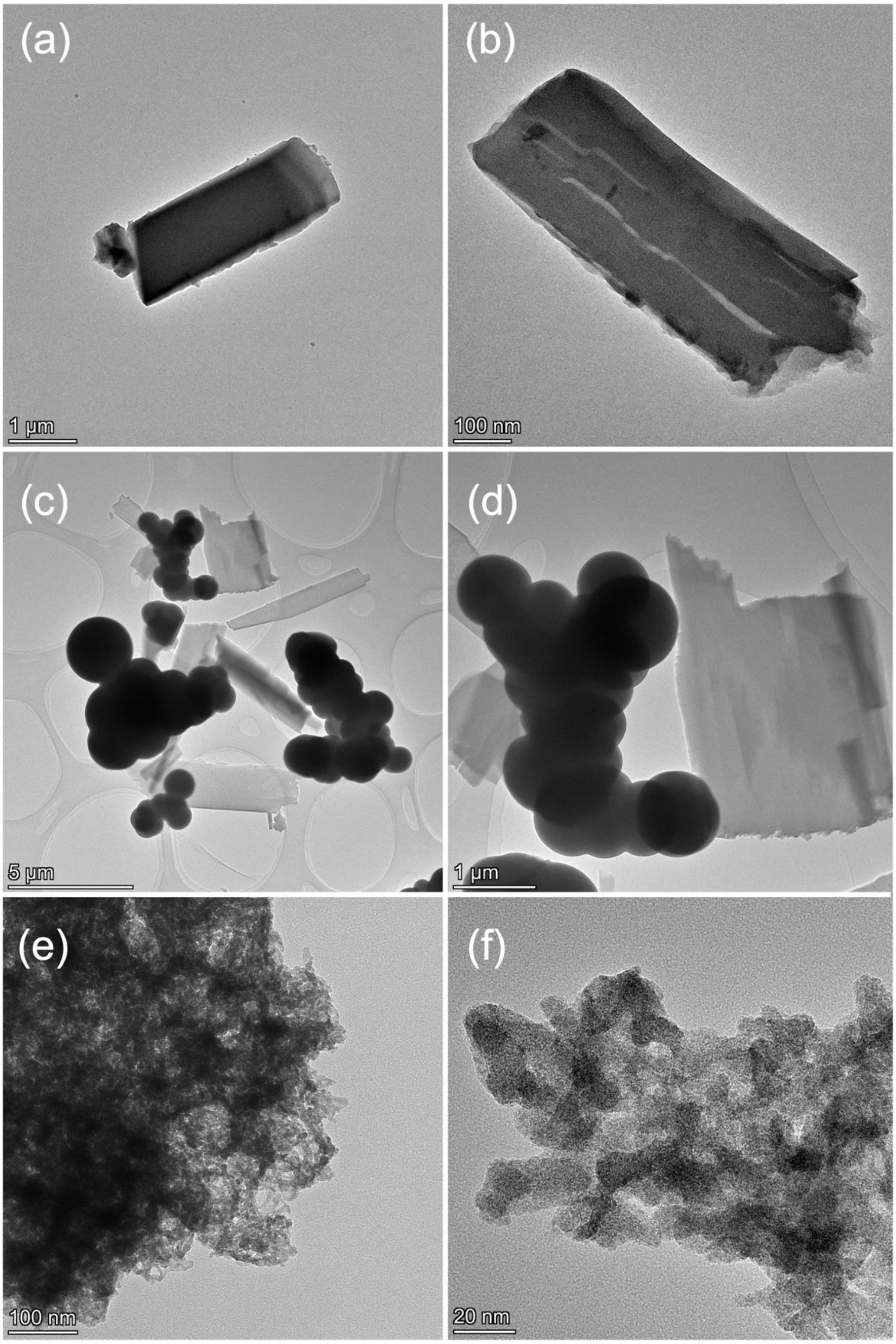

Figure S3. TEM images of (a, b) C-MOF, (c, d) S-MOF, and (e, f) A-MOF with different scales.

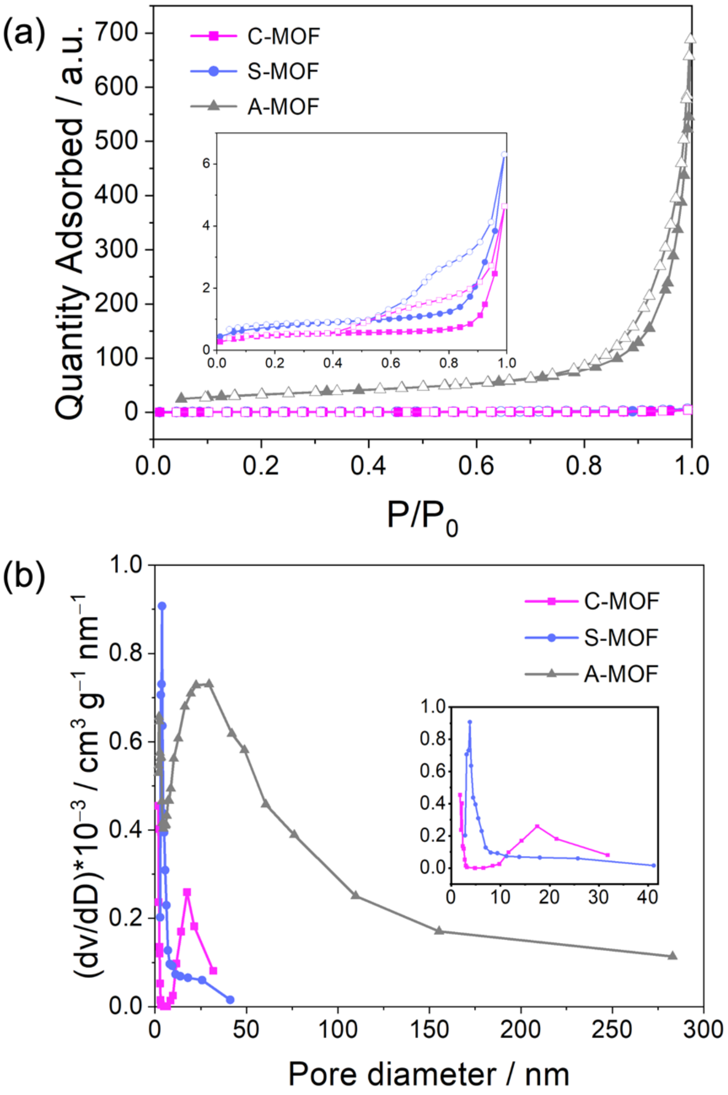

Figure S4. (a) Nitrogen sorption isotherms of C-MOF, S-MOF, and A-MOF at 77 K. Closed and open circles represent adsorption and desorption branches, respectively. A magnified version of the nitrogen sorption isotherms for C-MOF and S-MOF. (b) Pore size distributions (calculated by the Barrett–Joyner–Halenda method) of the as-synthesised C-MOF, S-MOF, and A-MOF. (b) A magnified version of the pore size distribution for C-MOF and S-MOF.

The nitrogen adsorption isotherms of C-MOF (S_{BET} = 1.66 m^2 g^{-1}) and S-MOF (S_{BET} = 2.64 m^2 g^{-1}) display Type IV behaviour. The hysteresis loops at a relatively high pressure, between 0.7 and 1.0, can be assigned as the H_2 type. A-MOF (S_{BET} = 117.1 m^2 g^{-1}) displays

Type III behaviour (Fig. S7). The smaller surface area of C-MOF and S-MOF can be attributed to their highly ordered structures, which are known to collapse into a non-porous form upon drying, and this lower surface area also agrees with the result in the formation of larger particles. This phenomenon also matches previously reported observations for Bi-BDC. In contrast, A-MOF exhibits a significantly different pore size distribution, revealing the presence of larger pores with diameters ranging from 6 to 280 nm. This increased pore size is a result of the higher degree of disconnection in A-MOF and also agrees with the smaller particle size as shown in the result of SEM.

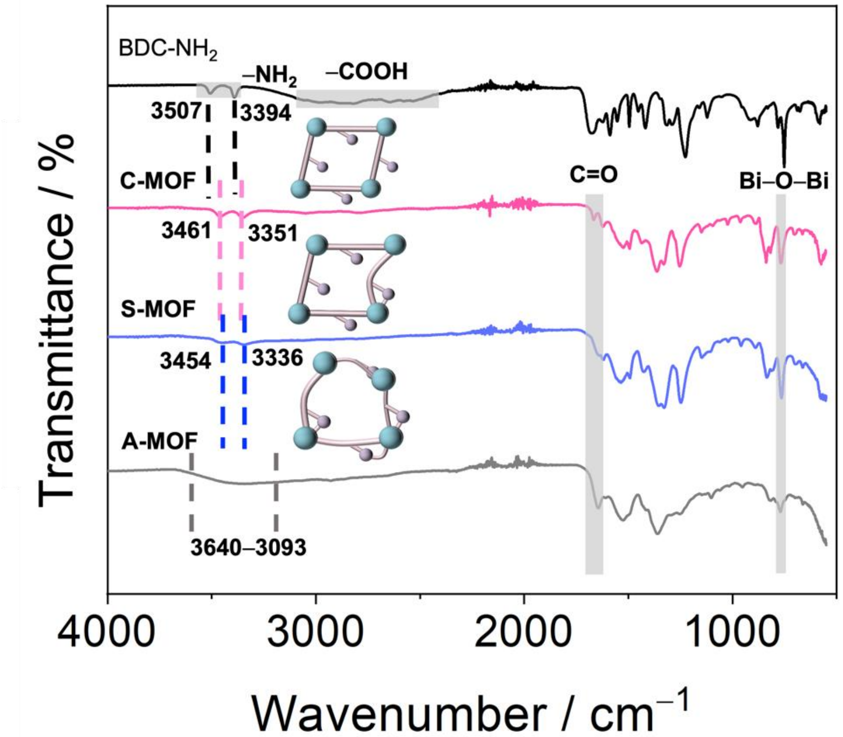

Figure S5. FTIR spectra of $H_2BDC\text{-}NH_2$ and a series of as-synthesised Bi-MOFs with different crystallinity.

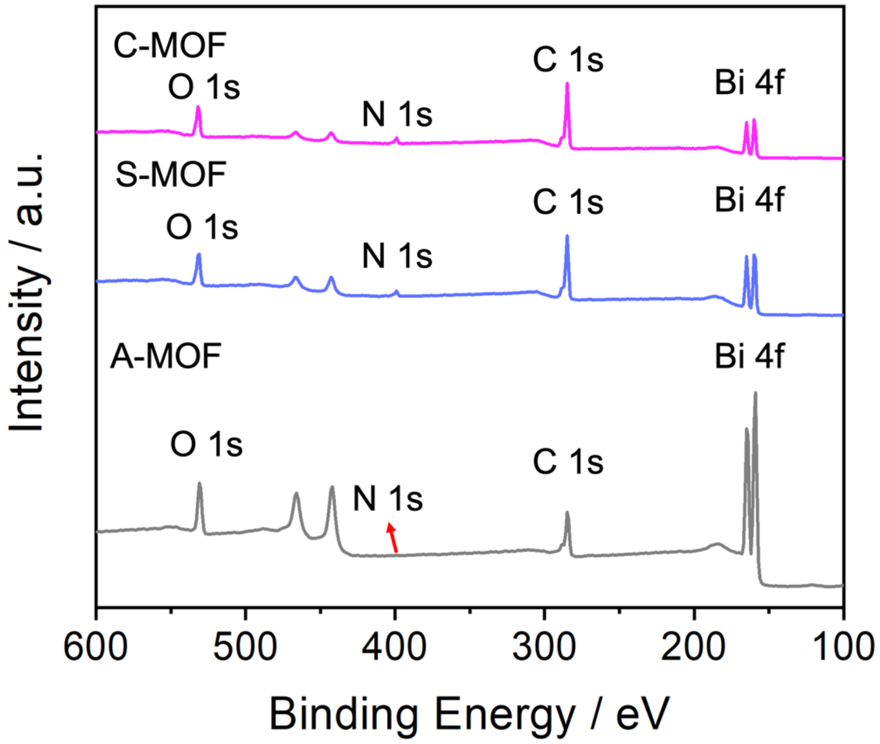

Figure S6. XPS survey spectrum of C-MOF, S-MOF, and A-MOF.

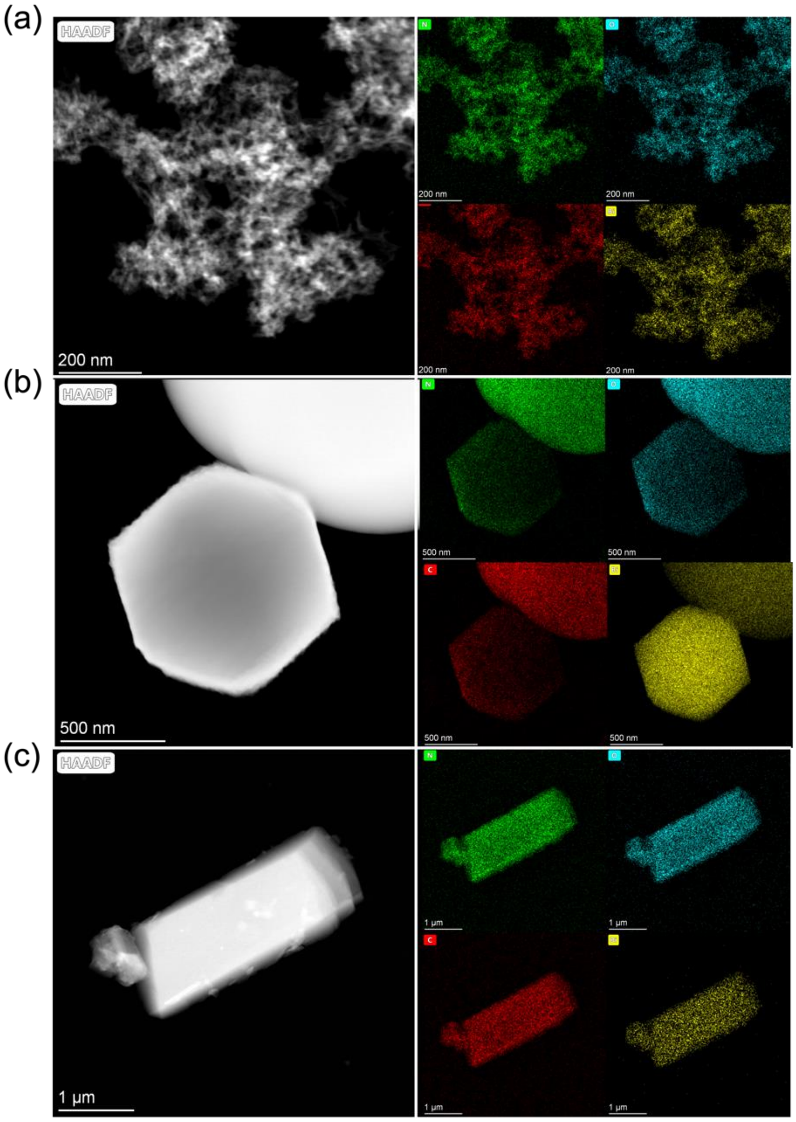

Figure S7. TEM images and energy-dispersive X-ray (EDX) spectroscopy mapping analysis of (a) A-MOF, (b) S-MOF, and (c) C-MOF.

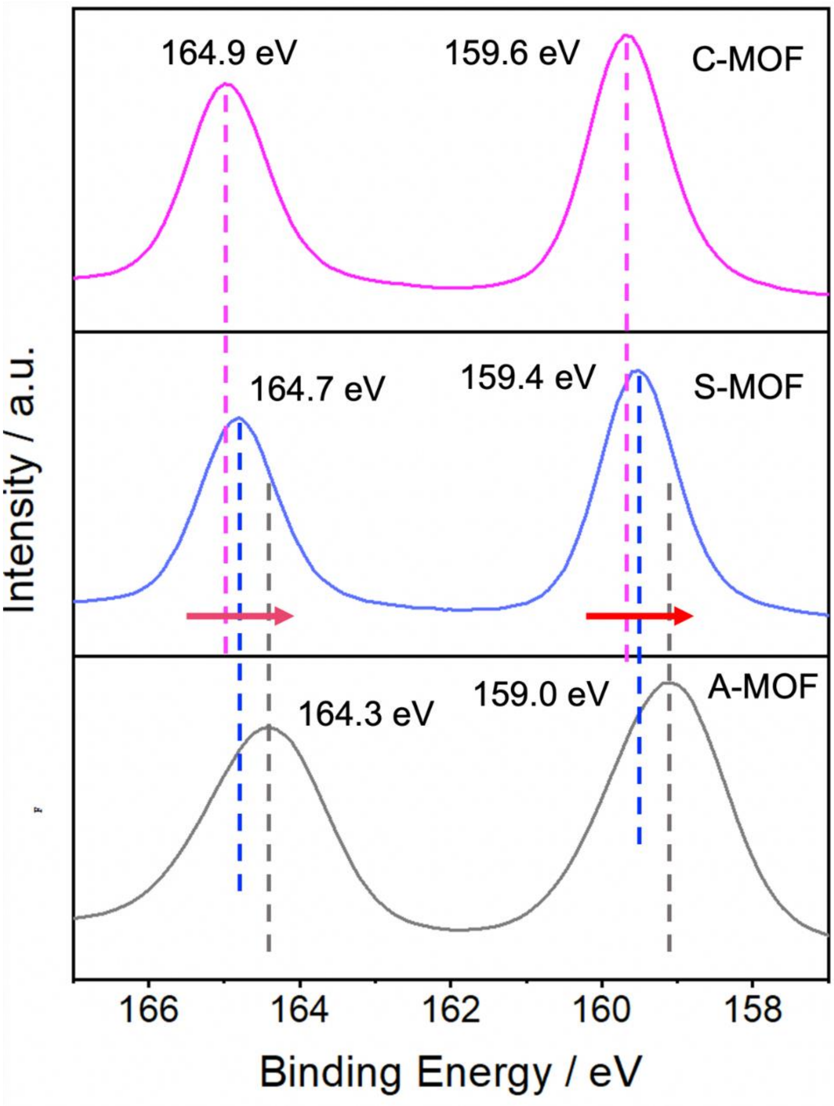

Figure S8. High-resolution XPS spectra of Bi 4f for C-MOF, S-MOF, and A-MOF.

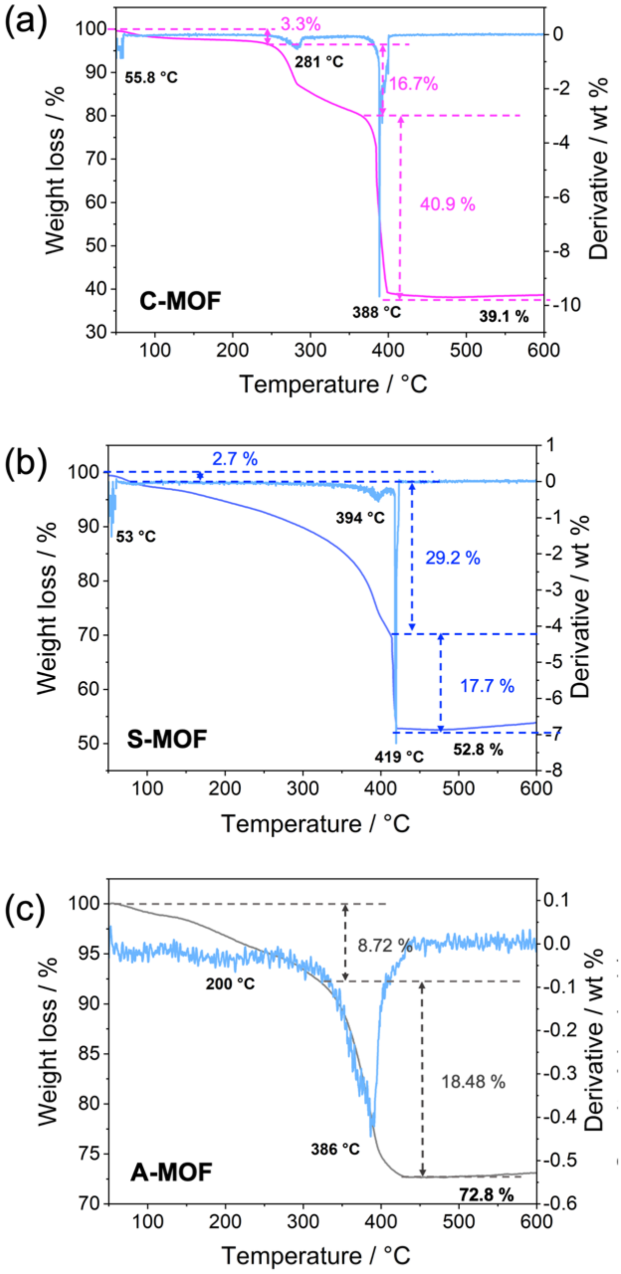

Figure S9. Thermogravimetric analysis (TGA) profiles of (a) C-MOF, (b) S-MOF, and (c) A-MOF.

TGA (Figure S9) was conducted to investigate the thermal stability of Bi-MOFs with different topologies and varying content of metal oxides after high-temperature decomposition. Figure S9c shows that A-MOF retained a significantly higher percentage of residual metal oxides after heat treatment, measuring 72.8%, compared with C-MOF (Figure S9a), which exhibited a residual weight of 39.1%. S-MOF (Figure S9b) had an intermediate residual weight of 52.8%. This variation can be attributed to the structural differences among these materials. In A-MOF, more Bi^{3+}–ligand bonds formed, resulting in an irregular and disordered structure. This disorder allowed for more metal content to remain after thermal decomposition. In contrast, the Bi^{3+} ions in C-MOF are arranged regularly and well-defined, facilitating a more predictable and stepwise decomposition pathway. Meanwhile, the three different topological structures of Bi-MOFs exhibit similar decomposition temperatures. Even though A-MOF contains unusual Bi-N coordination, this does not lower the decomposition temperature, demonstrating that the Bi–N bonds formed in A-MOF are also quite strong. Therefore, the chemical stability of the Bi-MOFs shall be affected by the synergetic effects on crystallinity and metal-ligand bond.

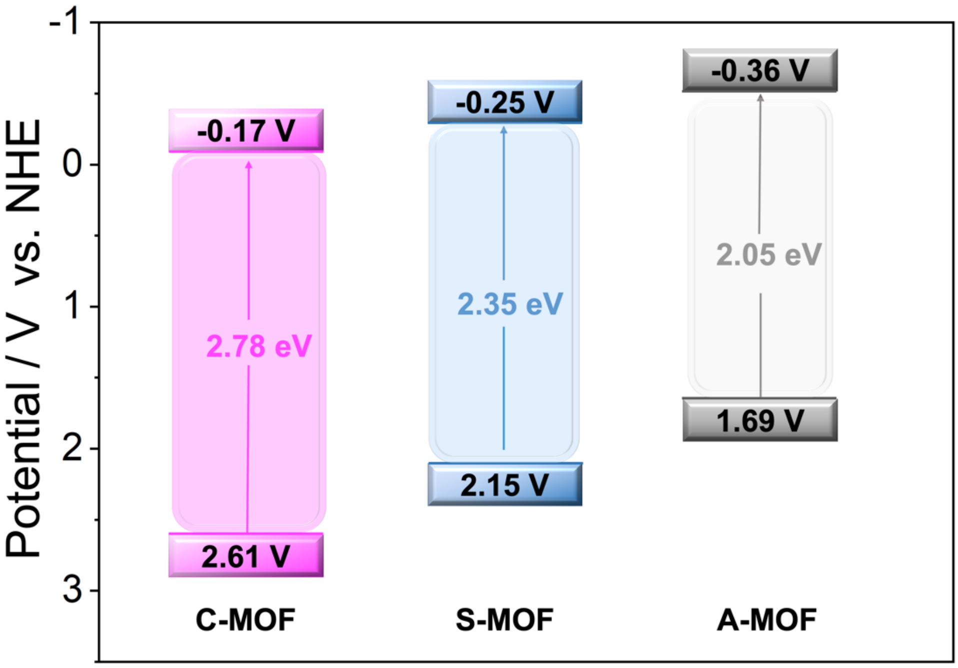

Figure S10. Band structure alignment of C-MOF, S-MOF, and A-MOF.

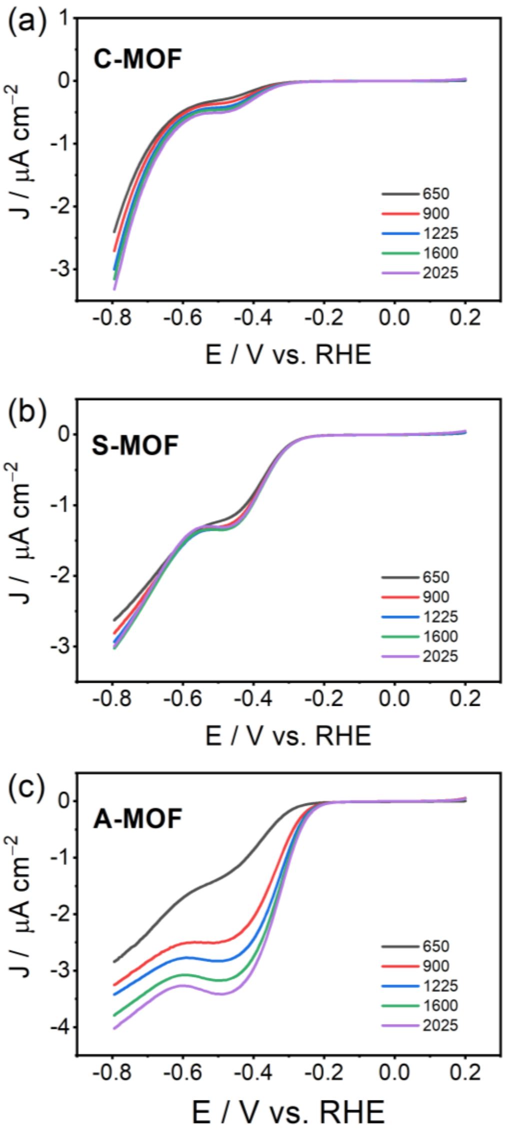

Figure S11. LSV curves at different rotation speeds, recorded at 5 mV s^{-1} scan rate, for C-MOF, S-MOF, and A-MOF.

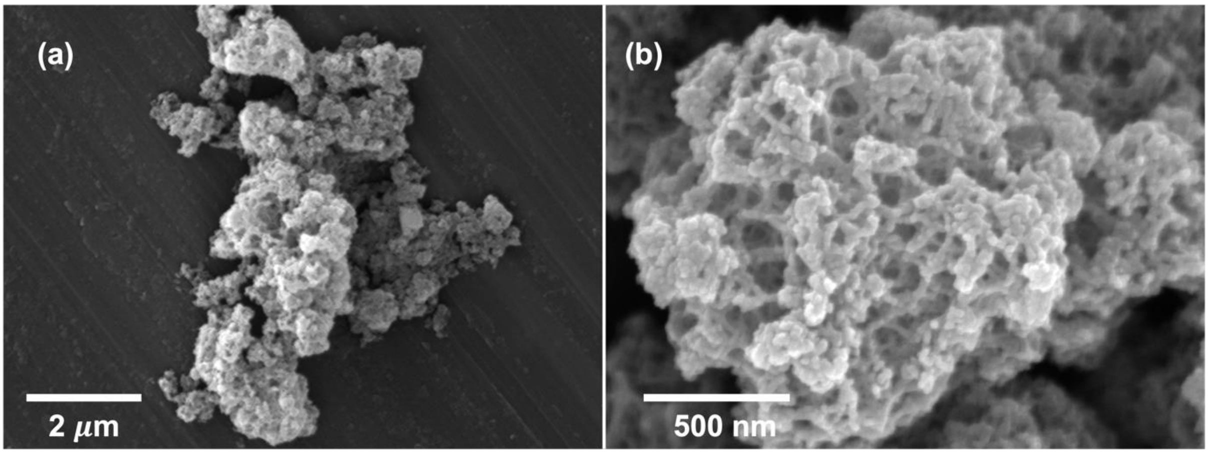

Figure S12. SEM images of A-MOF at different magnifications after photocatalytic NO oxidation.

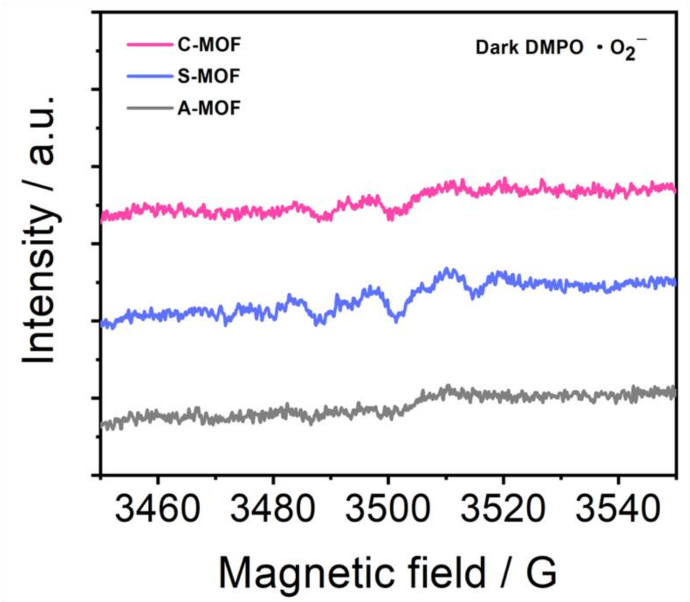

Figure S13. EPR spectra in the dark in aqueous dispersion for C-MOF, S-MOF, and A-MOF.

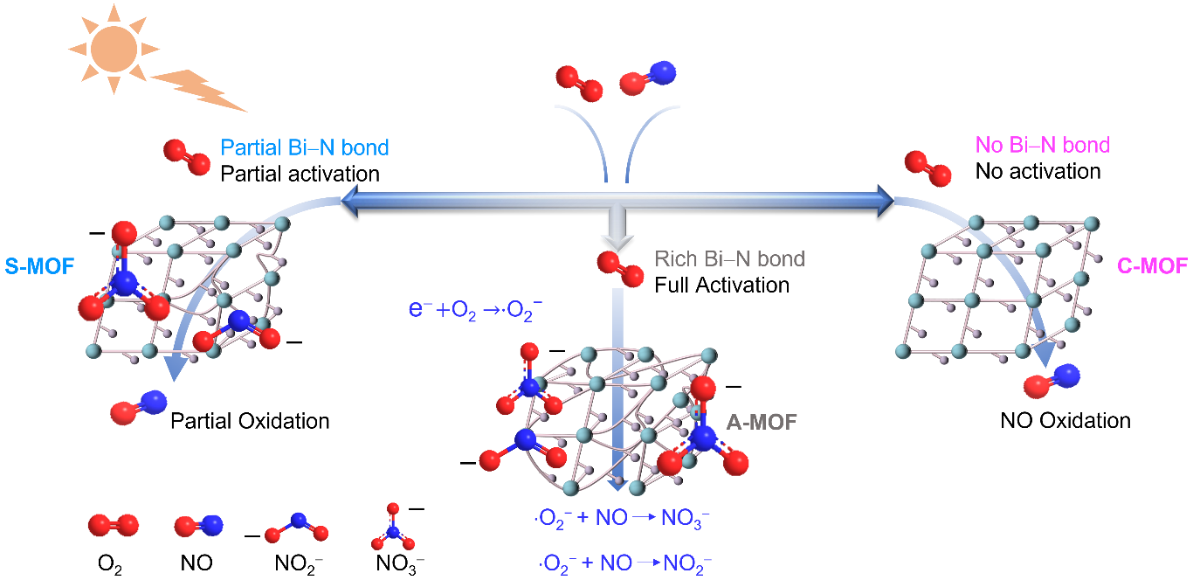

Figure S14. Photocatalytic removal pathway of NO in the Bi-MOFs with different topologies.

Table S2. The Comparison is based on metal-organic frameworks-based photocatalysts for the NO removal.

Entry	Samples	Light source	Initial NO concentration	Removal rate	Decline in recycling test	Reference
1	2CN/NU6-rGO-80	Xenon lamp (300 W)	600 ppb	65.8%	4	Sing et al., 2024
2	65-NMIL	Xenon lamp (300 W)	520 ppb	65.49%	2	Huang et a., 2023
3	D-NM-125/EY	Halogen lamp (150 W)	500 ppb	62.05%	5	Yang et al., 2028
4	NTM-2	Halogen lamp (150 W)	500 ppb	68.07%	5	Xu et al., 2024
5	CDs@NH_2-MIL-125(Ti)	LED lamp (12 W)	520 ppb	53.0%	5	He et al., 2021
6	Au@NML-(Cu/Ti)	LED lamp (12 W)	100 ppm	43 %	5	He et al., 2022
7	Zr-MOF-s(Pt)(Zr/Ti)-R)	LED lamp (12 W)	520 ppb	46.4 %	2	Li et al., 2023
8	A-MOF	LED lamp (30 W)	650 ppb	73.4 %	7	This work

Chapter 5 - Discussion and Conclusions

5.1 Brief discussion about three articles

The first alkaline earth metal-based metal-organic frameworks (MOFs) demonstrate significant potential for the efficient removal and sensing of copper(II) ions. Their unique structural properties, high surface area, and tunable pore sizes facilitate effective adsorption and selective binding of Cu^{2+} ions, making them suitable for environmental remediation applications. acid-modulated iron(III) metal-organic frameworks (MOFs) exhibit remarkable efficiency in the removal of piroxicam and ketoprofen from aqueous solutions. The modification of these frameworks enhances their adsorption capacity and selectivity, making them effective for the removal of pharmaceutical contaminants. The unique structural characteristics of iron(III) MOFs, combined with acid modulation, improve their interaction with the targeted drugs, facilitating a higher uptake. This study highlights the potential of using tailored MOFs for environmental applications, particularly in addressing the challenges posed by pharmaceutical pollutants in water systems. The, third tuning the topology of bismuth metal-organic frameworks (MOFs) significantly enhances their photocatalytic activity for nitrogen oxide (NO) oxidation. The strategic modification of framework structures improves light absorption and increases the availability of active sites, leading to more efficient photocatalytic performance. This research underscores the importance of structural design in optimizing photocatalytic materials, paving the way for the development of advanced MOFs that can effectively address air pollution challenges.

Comparing the results of the three publications

5.2 Comparing the results of the three articles

Metal-organic frameworks (MOFs) have gained significant attention in water treatment applications due to their unique properties, including high surface area, tunable porosity, and chemical stability. Alkaline MOFs, such as those based on calcium, have shown promise as effective adsorbents for removing copper ions from aqueous solutions. Their alkaline nature allows for enhanced ion exchange processes, where positively charged copper ions can easily interact with the negatively charged sites within the MOF structure. This interaction not only facilitates the adsorption of copper but also improves the selectivity and capacity of these materials for heavy metal ions. Additionally, alkaline MOFs can be synthesized from inexpensive and abundant materials, making them a cost-effective option for large-scale applications in water treatment.

On the other hand, iron MOFs, particularly when modified with acids as modulators, demonstrate a robust capacity for adsorbing pharmaceutical and personal care products (PPCPs) from contaminated water. The addition of acid can refine the crystallinity and pore structure of iron MOFs, enhancing their adsorption performance. The acidic conditions can facilitate better coordination between the iron centers and organic pollutants, leading to increased removal efficiency. Moreover, the iron within the MOF can also engage in redox reactions, further contributing to the degradation of PPCPs. This dual functionality—adsorption coupled with potential catalytic activity—positions iron MOFs as a valuable tool in addressing complex wastewater challenges, particularly in treating effluents that contain a mixture of organic contaminants.

In contrast, bismuth MOFs are predominantly studied for their photocatalytic properties, especially for removing nitrogen oxides (NO_x) from air. Controlling the crystallinity of bismuth MOFs is crucial for optimizing their photocatalytic performance. Well-structured MOFs exhibit improved charge separation and transfer, which are essential for efficient photocatalysis. When exposed to light, these bismuth-based frameworks can effectively degrade NO into less harmful species through oxidation processes. Unlike alkaline and iron MOFs, which primarily function as adsorbents, bismuth MOFs harness light energy to drive chemical reactions, thus targeting gaseous pollutants. This distinct mechanism of action highlights the complementary roles that different MOFs can play in environmental remediation, addressing both aqueous and gaseous contaminants in a holistic water treatment strategy. Overall, the choice between alkaline MOFs, iron MOFs with acid modulation, and bismuth MOFs for specific applications depends on the type of pollutant, the desired removal mechanism, and the operational conditions.

5.3 Directions for future research

The future directions for metal-organic frameworks (MOFs) as both adsorbents and photocatalysts are rich with potential innovations that can enhance their performance and broaden their application spectrum. One promising area of research is the development of MOF-on-MOF constructs. By synthesizing layered or core-shell MOF structures, researchers can create active sites that leverage the unique properties of different frameworks. For instance, a core of an iron MOF could be enveloped in an alkaline MOF shell, allowing for both effective heavy metal adsorption and catalytic degradation of organic pollutants. This approach can maximize the synergistic effects of different MOFs, leading to improved efficiency in pollutant removal.

Another significant direction involves manipulating the phase composition of MOFs to optimize their functional properties. By selectively altering the ratios of the metal ions or organic linkers during synthesis, researchers can fine-tune the structural characteristics, such as pore size and surface chemistry. These modifications can enhance the interaction between MOFs and target pollutants, improving adsorption capacities and kinetics. Additionally, transitioning between different phases—such as from a crystalline to an amorphous state—may unlock new pathways for catalysis, as amorphous materials often exhibit high activity due to their increased surface area and defect sites.

Moreover, the incorporation of dopants or co-catalysts into MOFs presents another exciting avenue for enhancing photocatalytic activity. Doping with metals such as titanium or zinc can facilitate charge separation and enhance light absorption, which are critical for effective photocatalysis. Similarly, coupling MOFs with other nanomaterials, such as graphene or carbon nanotubes, can create hybrid systems that exhibit improved charge transfer properties. These advanced materials can offer enhanced photocatalytic performance for the degradation of nitrogen oxides and other gaseous pollutants, making them highly suitable for air purification applications.

Finally, the applications of wastewater treatment and photocatalytic degradation of nitrogen monoxide, there are significant differences in the material design and performance requirements of MOFs. For wastewater treatment, MOFs must possess high selectivity and stability to effectively adsorb dissolved pollutants, while also considering the material's regeneration capacity and water resistance. In contrast, for gas-phase photocatalysis, MOFs need to optimize their light absorption capability and charge separation efficiency to enhance catalytic activity at specific wavelengths, while also maintaining stability under varying humidity and temperature conditions.

The feasibility of developing a simple MOF that effectively couples the functionalities of wastewater treatment and photocatalytic degradation of nitrogen monoxide hinges on strategic material design. By tailoring the structural and chemical properties of MOFs, it is possible to create a hybrid system that addresses the requirements of both applications.

Incorporating functional groups that enhance hydrophilicity can improve the adsorption capacity of MOFs for dissolved pollutants in aqueous environments. This can be achieved through the introduction of polar ligands or metal centers that interact favorably with water molecules, thus facilitating efficient pollutant capture. Additionally, optimizing pore size and surface area is crucial; larger pores can accommodate the steric demands of various contaminants while maintaining high surface area to promote adsorption.

Simultaneously, for photocatalytic activity, the MOF's light absorption characteristics must be engineered to ensure effective use of solar energy. This can involve doping the framework with metal or non-metal elements to shift the absorption spectrum into the visible range, thereby enhancing photocatalytic efficiency. Furthermore, the design must consider the charge separation mechanisms, which can be improved through the incorporation of electron acceptors within the MOF structure, promoting faster reaction kinetics for gas-phase nitrogen monoxide degradation.

In current reports, MIL-125-NH_2 and UIO-66-NH_2 have been widely applied as photocatalysts for the removal of NO. Both materials feature light-harvesting amine groups (-NH_2). In wastewater treatment, numerous experimental results have demonstrated that metal-organic frameworks containing -NH_2 groups can effectively couple with various types of heavy metal ions and organic pollutants.

Although the mechanisms of the two experiments are completely different, there are materials in both fields that have demonstrated the ability to function as adsorbents for pollutants while also serving as photocatalysts for NO removal. Therefore, developing a simple biocompatible metal-organic framework is feasible.

In summary, the future of MOFs as adsorbents and photocatalysts lies in innovative structural designs, phase composition adjustments, and the integration of responsive elements. These advancements promise to enhance the efficiency and applicability of MOFs in addressing pressing environmental challenges, paving the way for more sustainable water treatment and air purification technologies.

Reference

Abbasi, A., Moradpour, T., & Van Hecke, K. (2015). A new 3D cobalt (II) metal–organic framework nanostructure for heavy metal adsorption. *Inorganica Chimica Acta*, *430*, 261–267. https://doi.org/10.1016/j.ica.2015.03.019.

Ahmed, I., Hasan, Z., Lee, G., Lee, H. J., & Jhung, S. H. (2021). Contribution of hydrogen bonding to liquid-phase adsorptive removal of hazardous organics with metal-organic framework-based materials. *Chemical Engineering Journal*, *430*, 132596. https://doi.org/10.1016/j.cej.2021.132596.

Ahmed, I., Mondol, M. M. H., Jung, M., Lee, G. H., & Jhung, S. H. (2022). MOFs with bridging or terminal hydroxo ligands: Applications in adsorption, catalysis, and functionalization. *Coordination Chemistry Reviews*, *475*, 214912. https://doi.org/10.1016/j.ccr.2022.214912.

Ai, Z., Ho, W., Lee, S., & Zhang, L. (2009). Efficient Photocatalytic Removal of NO in Indoor Air with Hierarchical Bismuth Oxybromide Nanoplate Microspheres under Visible Light. *Environmental Science & Technology*, *43*(11), 4143–4150. https://doi.org/10.1021/es9004366.

Araya, T., Jia, M., Yang, J., Zhao, P., Cai, K., Ma, W., & Huang, Y. (2017). Resin modified MIL-53 (Fe) MOF for improvement of photocatalytic performance. *Applied Catalysis. B, Environmental*, *203*, 768–777. https://doi.org/10.1016/j.apcatb.2016.10.072.

Ashling, C. W., Johnstone, D. N., Widmer, R. N., Hou, J., Collins, S. M., Sapnik, A. F., Bumstead, A. M., Midgley, P. A., Chater, P. A., Keen, D. A., & Bennett, T. D. (2019). Synthesis and Properties of a Compositional Series of MIL-53(Al) Metal–Organic Framework Crystal-Glass Composites. *Journal of the American Chemical Society*, *141*(39), 15641–15648. https://doi.org/10.1021/jacs.9b07557.

Au, V. K. (2020). Recent advances in the use of Metal-Organic frameworks for dye adsorption. *Frontiers in Chemistry, 8*. https://doi.org/10.3389/fchem.2020.00708.

Au, V. K., Kwan, S. Y., Lai, M. N., & Low, K. (2021). Dual-Functional mesoporous Copper(II) Metal-Organic frameworks for the remediation of organic dyes. *Chemistry - a European Journal*, *27*(35), 9174–9179. https://doi.org/10.1002/chem.202100289.

Au, V. K.-M., Nakayashiki, K., Huang, H., Suginome, S., Sato, H., & Aida, T. (2019). Stepwise Expansion of Layered Metal–Organic Frameworks for Nonstochastic Exfoliation into Porous Nanosheets. *Journal of the American Chemical Society*, *141*(1), 53–57. https://doi.org/10.1021/jacs.8b09987.

Azbell, T. J., Pitt, T. A., Bollmeyer, M. M., Cong, C., Lancaster, K. M., & Milner, P. J. (2023). Ionothermal Synthesis of Metal-Organic Frameworks Using Low-Melting Metal Salt Precursors. *Angewandte Chemie International Edition*, *62*(17), e202218252-n/a. https://doi.org/10.1002/anie.202218252.

Bakhtiari, N., & Azizian, S. (2015). Adsorption of copper ion from aqueous solution by nanoporous MOF-5: A kinetic and equilibrium study. *Journal of Molecular Liquids*, *206*, 114–118. https://doi.org/10.1016/j.molliq.2015.02.009.

Bara, D., Wilson, C., Mörtel, M., Khusniyarov, M. M., Ling, S., Slater, B., Sproules, S., & Forgan, R. S. (2019). Kinetic Control of Interpenetration in Fe–Biphenyl-4,4′-dicarboxylate Metal–Organic Frameworks by Coordination and Oxidation Modulation. *Journal of the American Chemical Society*, *141*(20), 8346–8357. https://doi.org/10.1021/jacs.9b03269.

Bara, D., Wilson, C., Mörtel, M., Khusniyarov, M. M., Ling, S., Slater, B., Sproules, S., & Forgan, R. S. (2019). A universal approach for the synthesis of two-dimensional binary compounds. Journal of the American Chemical Society, *141*, 8346–8357. https://doi.org/10.1021/jacs.9b03172.

Basta, N. T., Ryan, J. A., Chaney, R. L., & Anonymous. (2005). Trace element chemistry in residual-treated soil; key concepts and metal bioavailability. *Journal of Environmental Quality*, *34*(1), 49–63. https://doi.org/10.2134/jeq2005.0049dup.

Bechis, I., Sapnik, A. F., Tarzia, A., Wolpert, E. H., Addicoat, M. A., Keen, D. A., Bennett, T. D., & Jelfs, K. E. (2022). Modeling the Effect of Defects and Disorder in Amorphous Metal–Organic Frameworks. *Chemistry of Materials*, *34*(20), 9042–9054. https://doi.org/10.1021/acs.chemmater.2c01528.

Bennett, T. D., & Cheetham, A. K. (2014). Amorphous Metal–Organic Frameworks. *Accounts of Chemical Research*, *47*(5), 1555–1562. https://doi.org/10.1021/ar5000314.

Bennett, T. D., Cheetham, A. K., Fuchs, A. H., & Coudert, F.-X. (2019). Interplay between Defects, Disorder and Flexibility in Metal-Organic Frameworks. https://doi.org/10.48550/arxiv.1904.09497.

Benoǐt Ferrari, Raphael Mons, Bernard Vollat, Benoǐt Fraysse, Nicklas Paxēaus, Roberto Lo Giudice, Antonino Pollio, Jeanne Garric, Environmental risk assessment of six human pharmaceuticals: Are the current environmental risk assessment procedures sufficient for the protection of the aquatic environment?, *Environmental Toxicology and Chemistry*, *23*(5), 1344–1354, https://doi.org/10.1897/03-246.

Bhunia, M. K., Hughes, J. T., Fettinger, J. C., & Navrotsky, A. (2013). Thermochemistry of Paddle Wheel MOFs: Cu-HKUST-1 and Zn-HKUST-1. *Langmuir*, *29*(25), 8140–8145. https://doi.org/10.1021/la4012839.

Biesinger, M. C. (2017). Advanced analysis of copper X-ray photoelectron spectra. *Surface and Interface Analysis*, *49*(13), 1325–1334. https://doi.org/10.1002/sia.6239.

Bunmahotama, W., Lin, T., & Yang, X. (2020). Prediction of adsorption capacity for pharmaceuticals, personal care products and endocrine disrupting chemicals onto various adsorbent materials. *Chemosphere (Oxford), 238*, 124658. https://doi.org/10.1016/j.chemosphere.2019.124658.

Calisto, V., Ferreira, C. I., Oliveira, J. A., Otero, M., & Esteves, V. I. (2015). Adsorptive removal of pharmaceuticals from water by commercial and waste-based carbons. *Journal of Environmental Management*, *152*, 83–90. https://doi.org/10.1016/j.jenvman.2015.01.019.

Cantu, D. C., McGrail, B. P., & Glezakou, V.-A. (2014). Formation Mechanism of the Secondary Building Unit in a Chromium Terephthalate Metal–Organic Framework. *Chemistry of Materials*, *26*(22), 6401–6409. https://doi.org/10.1021/cm5027859.

Cao, L., Huang, J., Wu, X., Ma, B., Xu, Q., Zhong, Y., Wu, Y., Sun, M., & Yu, L. (2023). Active-site stabilized Bi metal-organic framework-based catalyst for highly active and selective electroreduction of CO2 to formate over a wide potential window. *Nanoscale*, *15*(48), 19522–19532. https://doi.org/10.1039/d3nr04962k.

Cao, Y., Li, X., Yu, G., & Wang, B. (2022). Regulating defective sites for pharmaceuticals selective removal: Structure-dependent adsorption over continuously tunable pores. *Journal of Hazardous Materials, 442*, 130025. https://doi.org/10.1016/j.jhazmat.2022.130025.

Carpenter, B. P., Talosig, A. R., Rose, B., Di Palma, G., & Patterson, J. P. (2023). Understanding and controlling the nucleation and growth of metal-organic frameworks. *Chemical Society Reviews*, *52*(2), 6918–6937. https://doi.org/10.1039/d3cs00312d.

Castellanos, S., Kapteijn, F., & Gascon, J. (2016). Photoswitchable metal organic frameworks: turn on the lights and close the windows. *CrystEngComm*, *18*(22), 46–412. https://doi.org/10.1039/c5ce02543e.

Cheetham, A. K., Kieslich, G., & Yeung, H. H.-M. (2018). Thermodynamic and Kinetic Effects in the Crystallization of Metal–Organic Frameworks. *Accounts of Chemical Research*, *51*(3), 659–667. https://doi.org/10.1021/acs.accounts.7b00497.

Chen, J., Ouyang, J., Chen, W., Zheng, Z., Yang, Z., Liu, Z., & Zhou, L. (2021). Fabrication and adsorption mechanism of chitosan/Zr-MOF (UiO-66) composite foams for efficient removal of ketoprofen from aqueous solution. *Chemical Engineering Journal*, *431*, 134045. https://doi.org/10.1016/j.cej.2021.134045.

Chen, M., Li, X., Huang, Y., Yao, J., Li, Y., Lee, S., Ho, W., Huang, T., & Chen, K. (2020). Synthesis and characterization of Bi-BiPO4 nanocomposites as plasmonic photocatalysts for oxidative NO removal. *Applied Surface Science*, *513*, 145775. https://doi.org/10.1016/j.apsusc.2020.145775

Chen, M., Wei, X., Zhao, L., Huang, Y., Lee, S., Ho, W., & Chen, K. (2020). Novel N/Carbon Quantum Dot Modified MIL-125(Ti) Composite for Enhanced Visible-Light Photocatalytic Removal of NO. *Industrial & Engineering Chemistry Research*, *59*(14), 6470–6478. https://doi.org/10.1021/acs.iecr.9b06816,

Chen, Q., Yin, D., Zhu, S., & Hu, X. (2012). Adsorption of cadmium(II) on humic acid coated titanium dioxide. *Journal of Colloid and Interface Science*, *367*(1), 241–248. https://doi.org/10.1016/j.jcis.2011.10.005.

Chen, S., Shen, W., Yu, F., Hu, W., & Wang, H. (2010). Preparation of amidoximated bacterial cellulose and its adsorption mechanism for Cu2+ and Pb2. Journal of Applied Polymer Science, *117*(1), 8–15. https://doi.org/10.1002/app.31477.

Chen, W. S., Chen, Y. C., & Lee, C. H. (2022). Modified Activated Carbon for Copper Ion Removal from Aqueous Solution. *Processes*, *10*(1), 150. https://doi.org/10.3390/pr10010150.

Chen, X., Cai, Y., Liang, R., Tao, Y., Wang, W., Zhao, J., Chen, X., Li, H., & Zhang, D. (2020). NH2-UiO-66(Zr) with fast electron transfer routes for breaking down nitric oxide via photocatalysis. Applied Catalysis. B, Environmental, *267*, 118687. https://doi.org/10.1016/j.apcatb.2020.118687

Cheng, C., Chen, D., Li, N., Li, H., Xu, Q., He, J., & Lu, J. (2022). NH2-MIL-125(Ti) modified graphitic carbon nitride with carbon vacancy for efficient photocatalytic NO removal. *Chemosphere (Oxford)*, *307*, 135660–135660. https://doi.org/10.1016/j.chemosphere.2022.135660.

Cheng, X., Zhang, A., Hou, K., Liu, M., Wang, Y., Song, C., Zhang, G., & Guo, X. (2013). Size- and morphology-controlled NH2-MIL-53(Al) prepared in DMF-water mixed solvents. *Dalton Transactions : An International Journal of Inorganic Chemistry*, *42*(37), 13698–13705. https://doi.org/10.1039/c3dt51322j.

Chenthamara, D., Ramakrishnan, S. G., Robert, B., Murugan, P., & Subramaniam, S. (2021). Zinc chloride activated carbon from Pleurotus floridanus biomass for piroxicam adsorption. *Journal of Chemical Technology & Biotechnology*, *97*(3), 719–730. https://doi.org/10.1002/jctb.6957

Choi, S. B., Seo, M. J., Cho, M., Kim, Y., Jin, M. K., Jung, D.-Y., Choi, J.-S., Ahn, W.-S., Rowsell, J. L. C., & Kim, J. (2007). A Porous and Interpenetrated Metal–Organic Framework Comprising Tetranuclear IronIII–Oxo Clusters and Tripodal Organic Carboxylates and Its Implications for (3,8)-Coordinated Networks. *Crystal Growth & Design*, *7*(11), 2290–2293. https://doi.org/10.1021/cg070640e.

Collado, N., Rodriguez-Mozaz, S., Gros, M., Rubirola, A., Barceló, D., Comas, J., Rodriguez-Roda, I., & Buttiglieri, G. (2014). Pharmaceuticals occurrence in a WWTP with significant industrial contribution and its input into the river system. *Environmental Pollution (1987)*, *185*, 202–212. https://doi.org/10.1016/j.envpol.2013.10.040.

Cravillon, J., Nayuk, R., Springer, S., Feldhoff, A., Huber, K., & Wiebcke, M. (2011). Controlling Zeolitic Imidazolate Framework Nano- and Microcrystal Formation: Insight into Crystal Growth by Time-Resolved In Situ Static Light Scattering. *Chemistry of Materials*, *23*(8), 2130–2141. https://doi.org/10.1021/cm103571y.

Dan-Hardi, M., Chevreau, H., Devic, T., Horcajada, P., Maurin, G., Férey, G., Popov, D., Riekel, C., Wuttke, S., Lavalley, J.-C., Vimont, A., Boudewijns, T., de Vos, D., & Serre, C. (2012). How Interpenetration Ensures Rigidity and Permanent Porosity in a Highly Flexible Hybrid Solid. *Chemistry of Materials*, *24*(13), 2486–2492. https://doi.org/10.1021/cm300450x.

Dawood, S., Shaji, S., Pathiraja, G., Mo, Y., & Rathnayake, H. (2021). Molecular magnetism in nanodomains of isoreticular MIL-88(Fe)-MOFs. *Physical Chemistry Chemical Physics*, *23*(38), 21677–21689. https://doi.org/10.1039/d1cp03122h.

Di, J., Chen, C., Zhu, C., Song, P., Xiong, J., Ji, M., Zhou, J., Fu, Q., Xu, M., Hao, W., Xia, J., Li, S., Li, H., & Liu, Z. (2019). Bismuth Vacancy-Tuned Bismuth Oxybromide Ultrathin Nanosheets toward Photocatalytic CO2 Reduction. *ACS Applied Materials & Interfaces*, *11*(34), 30786–30792. https://doi.org/10.1021/acsami.9b08109.

Dissegna, S., Epp, K., Heinz, W. R., Kieslich, G., & Fischer, R. A. (2018). Defective Metal-Organic Frameworks. *Advanced Materials (Weinheim)*, *30*(37), e1704501-n/a. https://doi.org/10.1002/adma.201704501.

Dong, Y., Hu, T., Pudukudy, M., Su, H., Jiang, L., Shan, S., & Jia, Q. (2020). Influence of microwave-assisted synthesis on the structural and textural properties of mesoporous MIL-101(Fe) and NH2-MIL-101(Fe) for enhanced tetracycline adsorption. *Materials*

Chemistry and Physics, *251*, 123060. https://doi.org/10.1016/j.matchemphys.2020.123060.

Du, Z., Deng, S., Bei, Y., Huang, Q., Wang, B., Huang, J., & Yu, G. (2014). Adsorption behavior and mechanism of perfluorinated compounds on various adsorbents—A review. *Journal of Hazardous Materials*, *274*, 443–454. https://doi.org/10.1016/j.jhazmat.2014.04.038

Duan, J., Jin, W., & Kitagawa, S. (2017). Water-resistant porous coordination polymers for gas separation. *Coordination Chemistry Reviews*, *332*, 48–74. https://doi.org/10.1016/j.ccr.2016.11.004.

Fang, Y., Powell, J. A., Li, E., Wang, Q., Perry, Z., Kirchon, A., Yang, X., Xiao, Z., Zhu, C., Zhang, L., Huang, F., & Zhou, H.-C. (2019). Catalytic reactions within the cavity of coordination cages. *Chemical Society Reviews*, *48*(17), 477–473. https://doi.org/10.1039/c9cs00091g.

Fang, Z., Bueken, B., De Vos, D. E., & Fischer, R. A. (2015). Defect-Engineered Metal-Organic Frameworks. *Angewandte Chemie International Edition*, *54*(25), 7234–7254. https://doi.org/10.1002/anie.201411540

Feng, S., Sun, J., Feng, S., Zhang, Z., Wang, R., Liu, S., & Hu, J. (2019). Acid-promoted synthesis of MWCNT/UIO-66-NH2 nanocomposite for highly efficient removal of ketoprofen. *Chemistry Letters*, *48*(4), 394–397. https://doi.org/10.1246/cl.180953.

Feng, Y., Wu, L.-H., Zhang, C.-H., Zhou, B.-X., Zheng, S.-R., Zhang, W.-G., Cai, S.-L., & Fan, J. (2023). Porous amorphous metal-organic frameworks based on heterotopic triangular ligands for iodine and high-capacity dye adsorption. *Dalton Transactions : An International Journal of Inorganic Chemistry*, *52*(34), 1287–1297. https://doi.org/10.1039/d3dt01350b.

Fernandes, J. C. (Universidade N. de L., & Henriques, F. S. (1991). Biochemical, physiological, and structural effects of excess copper in plants. *The Botanical Review*, *57*(3), 246–273. https://doi.org/10.1007/bf02858564.

Filez, M., Caratelli, C., Rivera-Torrente, M., Muniz-Miranda, F., Hoek, M., Altelaar, M., Heck, A. J. R., Van Speybroeck, V., & Weckhuysen, B. M. (2021). Elucidation of the pre-nucleation phase directing metal-organic framework formation. *Cell Reports Physical Science*, *2*(12), 100680-. https://doi.org/10.1016/j.xcrp.2021.100680.

Fonseca, J., Gong, T., Jiao, L., & Jiang, H. (2021). Metal–organic frameworks (MOFs) beyond crystallinity: amorphous MOFs, MOF liquids and MOF glasses. *Journal of Materials Chemistry A*, *9*(17), 10562–10611. https://doi.org/10.1039/d1ta01043c.

Forgan, R. S. (2020). Modulated self-assembly of metal-organic frameworks. *Chemical Science (Cambridge)*, *11*(18), 4546–4562. https://doi.org/10.1039/d0sc01356k.

Foroutan, R., Peighambardoust, S. J., Mohammadi, R., Peighambardoust, S. H., & Ramavandi, B. (2022). Development of new magnetic adsorbent of walnut shell ash/starch/Fe3O4 for effective copper ions removal: Treatment of groundwater samples. *Chemosphere (Oxford)*, *296*, 133978–133978. https://doi.org/10.1016/j.chemosphere.2022.133978.

Fröhlich, A. C., Foletto, E. L., & Dotto, G. L. (2019). Preparation and characterization of NiFe2O4/activated carbon composite as potential magnetic adsorbent for removal of ibuprofen and ketoprofen pharmaceuticals from aqueous solutions. *Journal of Cleaner Production*, *229*, 828–837. https://doi.org/10.1016/j.jclepro.2019.05.037.

Gadzikwa, T., Farha, O. K., Mulfort, K. L., Hupp, J. T., & Nguyen, S. T. (2009). A Zn-based, pillared paddlewheel MOF containing free carboxylic acids via covalent post-synthesis elaboration. *Chemical Communications (Cambridge, England)*, *25*, 3720–3722. https://doi.org/10.1039/b823392f.

Gao, R., & Wang, L. (2020). Stable Cocatalyst-Free BiVO4 Photoanodes with Passivated Surface States for Photocorrosion Inhibition. *Angewandte Chemie International Edition*, *59*(51), 23094–23099. https://doi.org/10.1002/anie.202010908.

Gao, W.-Y., Cai, R., Pham, T., Forrest, K. A., Hogan, A., Nugent, P., Williams, K., Wojtas, L., Luebke, R., Weseliński, Ł. J., Zaworotko, M. J., Space, B., Chen, Y.-S., Eddaoudi, M., Shi, X., & Ma, S. (2015). Remote Stabilization of Copper Paddlewheel Based Molecular Building Blocks in Metal–Organic Frameworks. *Chemistry of Materials*, *27*(6), 2144–2151. https://doi.org/10.1021/acs.chemmater.5b00084.

Gao, Z., Xu, B., Fan, Y., Zhang, T., Chen, S., Yang, S., Zhang, W., Sun, X., Wei, Y., Wang, Z., Wang, X., Meng, X., & Zhao, Y. S. (2021). Topological-Distortion-Driven Amorphous Spherical Metal-Organic Frameworks for High-Quality Single-Mode Microlasers. *Angewandte Chemie International Edition*, *60*(12), 6362–6366. https://doi.org/10.1002/anie.202014033.

Georgin, J., Franco, D. S., Da Boit Martinello, K., Lima, E. C., & Silva, L. F. (2022). A review of the toxicology presence and removal of ketoprofen through adsorption technology. *Journal of Environmental Chemical Engineering*, *10*(3), 107798. https://doi.org/10.1016/j.jece.2022.107798.

Ghasempour, H., Wang, K.-Y., Powell, J. A., ZareKarizi, F., Lv, X.-L., Morsali, A., & Zhou, H.-C. (2021). Metal–organic frameworks based on multicarboxylate linkers. *Coordination Chemistry Reviews*, *426*(C), 213542. https://doi.org/10.1016/j.ccr.2020.213542.

Goldberg, S. (2005). Inconsistency in the triple layer model description of ionic strength dependent boron adsorption. *Journal of Colloid and Interface Science*, *285*(2), 509–517. https://doi.org/10.1016/j.jcis.2004.12.002.

Govarthanan, M., Mythili, R., Kim, W., Alfarraj, S., & Alharbi, S. A. (2021). Facile fabrication of (2D/2D) MoS2@MIL-88(Fe) interface-driven catalyst for efficient degradation of organic pollutants under visible light irradiation. *Journal of Hazardous Materials*, *414*, 125522. https://doi.org/10.1016/j.jhazmat.2021.125522.

Guesh, K., Caiuby, C. A. D., Mayoral, A., Díaz-García, M., Díaz, I., & Sanchez-Sanchez, M. (2017). Sustainable Preparation of MIL-100(Fe) and Its Photocatalytic Behavior in the Degradation of Methyl Orange in Water. *Crystal Growth & Design*, *17*(4), 1806–1813. https://doi.org/10.1021/acs.cgd.6b01776.

Guo, H., Zhu, Y., Wang, S., Su, S., Zhou, L., & Zhang, H. (2012). Combining Coordination Modulation with Acid–Base Adjustment for the Control over Size of Metal–Organic Frameworks. *Chemistry of Materials*, *24*(3), 444–450. https://doi.org/10.1021/cm202593h.

Guo, W., Zhang, W., Han, N., Xie, S., Zhou, Z., Monnens, W., Martinez Mora, O., Xue, Z., Zhang, X., Zhang, X., & Fransaer, J. (2023). Electrosynthesis of Metal-Organic Framework Films with Well-Defined Facets. *Chemistry (Weinheim an der Bergstrasse, Germany)*, *29*(62), e202302338. https://doi.org/10.1002/chem.202302338.

Guo, Y., Jia, Z., Shi, Q., Liu, Z., Wang, X., & Li, L. (2019). Zr (IV)-based coordination porous materials for adsorption of Copper(II) from water. *Microporous and Mesoporous Materials*, *285*, 215–222. https://doi.org/10.1016/j.micromeso.2019.05.020.

Gutiérrez, E. L., Montaña, M. P., & Ferrari, G. V. (2019). On Piroxicam degradation by homogeneous Fenton’s reaction and the influence of iron cations complexation. *Journal of Water Process Engineering*, *28*, 82–87. https://doi.org/10.1016/j.jwpe.2019.01.004.

Hameed, B. H., Din, A. T. M., & Ahmad, A. L. (2007). Adsorption of methylene blue onto bamboo-based activated carbon: Kinetics and equilibrium studies. *Journal of Hazardous Materials*, *141*(3), 819–825. https://doi.org/10.1016/j.jhazmat.2006.07.049.

Hamisu, A. M., Ariffin, A., & Wibowo, A. C. (2020). Cation exchange in metal-organic frameworks (MOFs): The hard-soft acid-base (HSAB) principle appraisal. *Inorganica Chimica Acta*, *511*, 119801.

Han, J., Xiao, B., Le, P. K., & Mangwandi, C. (2023). Enhancement of the Solubility of BS Class II Drugs with MOF and MOF/GO Composite Materials: Case Studies of Felodipine, Ketoprofen and Ibuprofen. *Materials*, *16*(4), 1554. https://doi.org/10.3390/ma16041554

Haque, E., Lee, J. E., Jang, I. T., Hwang, Y. K., Chang, J., Jegal, J., & Jhung, S. H. (2010). Adsorptive removal of methyl orange from aqueous solution with metal-organic frameworks, porous chromium-benzenedicarboxylates. *Journal of Hazardous Materials*, *181*(1–3), 535–542. https://doi.org/10.1016/j.jhazmat.2010.05.047.

He, T., Kong, X. J., & Li, J. R. (2021). Chemically stable metal–organic frameworks: rational construction and application expansion. *Accounts of Chemical Research*, *54*(15), 3083-3094.

He, Y., Li, H., Wu, J., Liu, Z., Chen, Y., Guo, W., Wu, Y., Fu, M., & Liu, X. (2022). In-situ formation of Au nanoparticles with surface plasmon resonance confined in the framework of Cu ions doped NH2-MIL-125(Ti) to enhance photocatalytic hydrogen production and NO removal. *Applied Surface Science*, *604*, 154641. https://doi.org/10.1016/j.apsusc.2022.15464.

He, Y., Tan, Y., Song, M., Tu, Q., Fu, M., Long, L., Wu, J., Xu, M., & Liu, X. (2022). Switching on photocatalytic NO oxidation and proton reduction of NH2-MIL-125(Ti) by convenient linker defect engineering. *Journal of Hazardous Materials*, *430*, 128468-. https://doi.org/10.1016/j.jhazmat.2022.128468.

He, Y., Tan, Y., Song, M., Tu, Q., Fu, M., Long, L., Wu, J., Xu, M., & Liu, X. (2022). Switching on photocatalytic NO oxidation and proton reduction of NH2-MIL-125(Ti) by convenient linker defect engineering. *Journal of Hazardous Materials*, *430*, 128468. https://doi.org/10.1016/j.jhazmat.2022.128468.

He, Y., Zhou, W., Qian, G., & Chen, B. (2014). Methane storage in metal-organic frameworks. *Chemical Society Reviews*, *43*(16), 5657–5678. https://doi.org/10.1039/c4cs00032c

Ho, T. (1975). Hard soft acids bases (HSAB) principle and organic chemistry. *Chemical Reviews*, *75*(1), 1–20. https://doi.org/10.1021/cr60293a001.

Horcajada, P., Salles, F., Wuttke, S., Devic, T., Heurtaux, D., Maurin, G., Vimont, A., Daturi, M., David, O., Magnier, E., Stock, N., Filinchuk, Y., Popov, D., Riekel, C., Férey, G., & Serre, C. (2011). How Linker's Modification Controls Swelling Properties of Highly Flexible Iron(III) Dicarboxylates MIL-88. *Journal of the American Chemical Society*, *133*(44), 17839–17847. https://doi.org/10.1021/ja206936e.

Hossain, Md. A., Mondol, Md. M. H., & Jhung, S. H. (2022). Functionalized metal-organic framework-derived carbon: Effective adsorbent to eliminate methylene blue, a small cationic dye from water. *Chemosphere (Oxford)*, *303*(Pt 1), 134890–134890. https://doi.org/10.1016/j.chemosphere.2022.134890.

Howarth, A. J., Liu, Y., Hupp, J. T., & Farha, O. K. (2015). Metal-organic frameworks for applications in remediation of oxyanion/cation-contaminated water. *CrystEngComm*, *17*(38), 7245–7253. https://doi.org/10.1039/c5ce01428j.

Hu, Z., Deibert, B. J., & Li, J. (2014). Luminescent metal-organic frameworks for chemical sensing and explosive detection. *Chemical Society Reviews*, *43*(16), 5815–584. https://doi.org/10.1039/c4cs00010b.

Huang, R., Zhou, Z., Lan, X., Tang, F. K., Cheng, T., Sun, H., Cham-Fai Leung, K., Li, X., & Jin, L. (2023). Rapid synthesis of bismuth-organic frameworks as selective antimicrobial materials against microbial biofilms. *Materials Today Bio*, *18*, 100507. https://doi.org/10.1016/j.mtbio.2022.100507.

Huxford, R. C., Della Rocca, J., & Lin, W. (2010). Metal–organic frameworks as potential drug carriers. *Current Opinion in Chemical Biology*, *14*(2), 262–268. https://doi.org/10.1016/j.cbpa.2009.12.012.

Iacomi, P., Gulcay-Ozcan, E., Pires Conti, P., Biswas, S., Steunou, N., Maurin, G., Rioland, G., & Devautour-Vinot, S. (2022). MIL-101(Cr) MOF as an Effective Siloxane Sensor. *ACS Applied Materials & Interfaces*, *14*(15), 17531–17538. https://doi.org/10.1021/acsami.2c02607.

Imaz, I., Hernando, J., Ruiz-Molina, D., & Maspoch, D. (2009). Metal-Organic Spheres as Functional Systems for Guest Encapsulation. *Angewandte Chemie (International Ed.)*, *48*(13), 2325–2329. https://doi.org/10.1002/anie.200804255.

Jain, P., Deolikar, G. L., Shrivastava, A., & Motghare, R. V. (2024). Synthesis and evaluation of mixed 3d transition metal organic frameworks for energy application. *Materials Today Communications*, *39*, 108748. https://doi.org/10.1016/j.mtcomm.2024.108748.

Jiang, D., Huang, C., Zhu, J., Wang, P., Liu, Z., & Fang, D. (2021). Classification and role of modulators on crystal engineering of metal organic frameworks (MOFs). *Coordination Chemistry Reviews*, *444*, 214064. https://doi.org/10.1016/j.ccr.2021.214064.

Jin, E., Lee, S., Kang, E., Kim, Y., & Choe, W. (2020). Metal-organic frameworks as advanced adsorbents for pharmaceutical and personal care products. *Coordination Chemistry Reviews*, *425*, 213526. https://doi.org/10.1016/j.ccr.2020.213526

Jin, J., Feng, T., Ma, Y., Wang, W., Wang, Y., Zhou, Q., & Li, A. (2017). Novel magnetic carboxyl modified hypercrosslinked resins for effective removal of typical PPCPs. *Chemosphere*, *185*, 563–573. https://doi.org/10.1016/j.chemosphere.2017.07.058

Jin, S., Son, H.-J., Farha, O. K., Wiederrecht, G. P., & Hupp, J. T. (2013). Energy Transfer from Quantum Dots to Metal–Organic Frameworks for Enhanced Light Harvesting. *Journal of the American Chemical Society*, *135*(3), 955–958. https://doi.org/10.1021/ja3097114.

Kalam, S., Abu-Khamsin, S. A., Kamal, M. S., & Patil, S. (2021). Surfactant Adsorption Isotherms: A Review. *ACS Omega*, *6*(48), 32342–32348. https://doi.org/10.1021/acsomega.1c04661

Kaye, S. S., Dailly, A., Yaghi, O. M., & Long, J. R. (2007). Impact of preparation and handling on the hydrogen storage properties of Zn4O (1, 4-benzenedicarboxylate) 3 (MOF-5). *Journal of the American Chemical Society*, *129*(46), 14176-14177. https://doi.org/10.1021/ja076877g.

Kazemi, A., Moghadaskhou, F., Pordsari, M. A., Manteghi, F., Tadjarodi, A., & Ghaemi, A. (2023). Enhanced CO2 capture potential of UiO-66-NH2 synthesized by sonochemical method: experimental findings and performance evaluation. *Scientific Reports*, *13*(1), 19891–19891. https://doi.org/10.1038/s41598-023-47221-6.

Kojima, D., Sanada, T., Wada, N., & Kojima, K. (2018). Synthesis, structure, and fluorescence properties of a calcium-based metal-organic framework. *RSC Advances*, *8*(55), 31588–31593. https://doi.org/10.1039/c8ra06043f.

Kondo, M., Okubo, T., Asami, A., Noro, S., Yoshitomi, T., Kitagawa, S., Ishii, T., Matsuzaka, H., & Seki, K. (1999). Rational Synthesis of Stable Channel-Like Cavities with Methane Gas Adsorption Properties: [{Cu2(pzdc)2(L)}n] (pzdc=pyrazine-2,3-dicarboxylate; L=a Pillar Ligand). *Angewandte Chemie International Edition, 38*(1–2), 140–143. https://doi.org/10.1002/(SICI)1521-3773(19990115)38:1/2<140::AID-ANIE140>3.0.CO;2-9.

Koryakina, I. G., Bachinin, S. V., Gerasimova, E. N., Timofeeva, M. V., Shipilovskikh, S. A., Bukatin, A. S., Sakhatskii, A., Timin, A. S., Milichko, V. A., & Zyuzin, M. V. (2023). Microfluidic synthesis of metal-organic framework crystals with surface defects for enhanced molecular loading. *Chemical Engineering Journal*, *452*(3), 139450. https://doi.org/10.1016/j.cej.2022.139450.

Kreno, L. E., Leong, K., Farha, O. K., Allendorf, M., Van Duyne, R. P., & Hupp, J. T. (2012). Metal–Organic Framework Materials as Chemical Sensors. *Chemical Reviews*, *112*(2), 1105–1125. https://doi.org/10.1021/cr200324t.

Krstic, V., Urosevic, T., & Pesovski, B. (2018). A review on adsorbents for treatment of water and wastewaters containing copper ions. *Chemical Engineering Science*, *192*, 273–287. https://doi.org/10.1016/j.ces.2018.07.022.

Kumar, P., Deep, A., & Kim, K.-H. (2015). Metal organic frameworks for sensing applications. *TrAC, Trends in Analytical Chemistry (Regular Ed.)*, *73*, 39–53. https://doi.org/10.1016/j.trac.2015.04.009.

Kuznicki, A., Lorzing, G. R., & Bloch, E. D. (2021). Tuning water adsorption, stability, and phase in Fe-MIL-101 and Fe-MIL-88 analogs with amide functionalization. *Chemical Communications (Cambridge, England)*, *57*(67), 8312–8315. https://doi.org/10.1039/d1cc02104d.

Larabi, C., & Quadrelli, E. A. (2012). Titration of Zr3(μ-OH) Hydroxy Groups at the Cornerstones of Bulk MOF UiO-67, [Zr6O4(OH)4(biphenyldicarboxylate)6], and Their Reaction with [AuMe(PMe3)]. *European Journal of Inorganic Chemistry*, *2012*(18), 3014–3022. https://doi.org/10.1002/ejic.201200033.

Lawal, I. A., Lawal, M. M., Akpotu, S. O., Azeez, M. A., Ndungu, P., & Moodley, B. (2018). Theoretical and experimental adsorption studies of sulfamethoxazole and ketoprofen on synthesized ionic liquids modified CNTs. *Ecotoxicology and Environmental Safety*, *161*, 542–552. https://doi.org/10.1016/j.ecoenv.2018.06.019.

Lawson, H. D., Walton, S. P., & Chan, C. (2021). Metal–Organic Frameworks for Drug Delivery: A Design Perspective. *ACS Applied Materials & Interfaces*, *13*(6), 7004–7020. https://doi.org/10.1021/acsami.1c01089.

Li, J. R., Kuppler, R. J., & Zhou, H. C. (2009). Selective gas adsorption and separation in metal–organic frameworks. *Chemical Society Reviews*, *38*(5), 1477-1504. https://doi.org/10.1039/B802426J.

Li, J. R., Kuppler, R. J., & Zhou, H. C. (2009). Selective gas adsorption and separation in metal-organic frameworks. *Chemical Society Reviews*, *38*(5), 1477–1504. https://doi.org/10.1039/b802426j.

Li, R., Wu, Z., Chen, Y., Liu, X., Guo, W., Huang, Y., Fu, M., & He, Y. (2023). Boosting the photocatalytic hydrogen evolution and NO removal via synergistic effects of in-situ Pt NPs formation and titanium integration in Zr-Porphyrin MOFs. *Fuel (Guildford), 336,* 126766-. https://doi.org/10.1016/j.fuel.2022.126766

Li, X., Dong, Q., Li, F., Zhu, Q., Tian, Q., Tian, L., Zhu, Y., Pan, B., Padervand, M., & Wang, C. (2024). Defective Bi@BiOBr/C microrods derived from Bi-MOF for efficient photocatalytic NO abatement: Directional regulation of interfacial charge transfer via carbon–loading. *Applied Catalysis. B, Environmental*, *340*, 123238. https://doi.org/10.1016/j.apcatb.2023.123238.

Li, Y., Gu, M., Zhang, M., Zhang, X., Lv, K., Liu, Y., Ho, W., & Dong, F. (2020). C3N4 with engineered three coordinated (N3C) nitrogen vacancy boosts the production of 1O2 for Efficient and stable NO photo-oxidation. *Chemical Engineering Journal* (Lausanne, Switzerland : 1996), *389*, 124421. https://doi.org/10.1016/j.cej.2020.124421.

Li, Z., Liu, X., Jin, W., Hu, Q., & Zhao, Y. (2019). Adsorption behavior of arsenicals on MIL-101(Fe): The role of arsenic chemical structures. *Journal of Colloid and Interface Science*, *554*, 692–704. https://doi.org/10.1016/j.jcis.2019.07.046.

Liang, N., Hu, X., Zhang, X., Li, W., Guo, Z., Huang, X., Li, Z., Zhang, R., Shen, T., Zou, X., & Shi, J. (2023). Alkaline earth metal–organic frameworks with tailorable ion release. Journal of Agricultural and Food Chemistry, *71*, 7584–7592. https://doi.org/10.1021/acs.jafc.3c01234

Liang, Z., Gao, Q., Wu, Z., & Gao, H. (2022). Removal and kinetics of cadmium and copper ion adsorption in aqueous solution by zeolite NaX synthesized from coal gangue. *Environmental Science and Pollution Research International*, *29*(56), 84651–84660. https://doi.org/10.1007/s11356-022-21700-1.

Lin, J., Ho, W., Qin, X., Leung, C., Au, V. K., & Lee, S. (2022). Metal–Organic Frameworks for NOx Adsorption and Their Applications in Separation, Sensing, Catalysis, and Biology. *Small*, *18*(13), e2105484-n/a. https://doi.org/10.1002/smll.202105484.

Lin, J., Ho, W., Qin, X., Leung, C.-F., Au, V. K.-M., & Lee, S.-C. (2022). Metal–organic frameworks for NO_x adsorption and applications in separation, sensing, catalysis, and biology. Small, *18*, 2105484. https://doi.org/10.1002/smll.202105484.

Lin, R.-B., Xiang, S., Xing, H., Zhou, W., & Chen, B. (2019). Exploration of porous metal–organic frameworks for gas separation and purification. *Coordination Chemistry Reviews*, *378*, 87–103. https://doi.org/10.1016/j.ccr.2017.09.027.

Lin, Z., Richardson, J. J., Zhou, J., & Caruso, F. (2023). Direct synthesis of amorphous coordination polymers and metal–organic frameworks. *Nature Reviews. Chemistry*, *7*(4), 273–286. https://doi.org/10.1038/s41570-023-00474-1.

Lionet, Z., Kim, T.-H., Horiuchi, Y., Lee, S. W., & Matsuoka, M. (2019). Linker Engineering of Iron-Based MOFs for Efficient Visible-Light-Driven Water Oxidation Reaction. *The Journal of Physical Chemistry C*, *123*(45), 27501–27508. https://doi.org/10.1021/acs.jpcc.9b06838.

Liu, C., Wang, J., Wan, J., Cheng, Y., Huang, R., Zhang, C., Hu, W., Wei, G., & Yu, C. (2020). Amorphous Metal–Organic Framework-Dominated Nanocomposites with Both Compositional and Structural Heterogeneity for Oxygen Evolution. *Angewandte Chemie International Edition*, *59*(9), 3630–3637. https://doi.org/10.1002/anie.201914587.

Liu, F., Zhao, J., Wang, S., Du, P., & Xing, B. (2014). Effects of solution chemistry on adsorption of selected pharmaceuticals and personal care products (PPCPs) by graphenes and carbon nanotubes. *Environmental Science & Technology*, *48*(22), 13197–13206. https://doi.org/10.1021/es5034684

Liu, H., Zhao, Y., Zhou, C., Mu, B., & Chen, L. (2021). Microwave-assisted synthesis of Zr-based metal–organic framework (Zr-fum-fcu-MOF) for gas adsorption separation. *Chemical Physics Letters*, *780*, 138906. https://doi.org/10.1016/j.cplett.2021.138906

Liu, J., Huang, X., Jia, L., Liu, L., Nie, Q., Tan, Z., & Yu, H. (2023). Microwave-Assisted Rapid Substitution of Ti for Zr to Produce Bimetallic (Zr/Ti)UiO-66-NH2 with

Congenetic “Shell–Core” Structure for Enhancing Photocatalytic Removal of Nitric Oxide. *Small*, *19*(20), e2207198-n/a. https://doi.org/10.1002/smll.202207198

Liu, T., Gou, S., He, Y., Fang, S., Zhou, L., Gou, G., & Liu, L. (2021). N-methylene phosphonic chitosan aerogels for efficient capture of Cu2+ and Pb2+ from aqueous environment. *Carbohydrate Polymers*, *269*, 118355–118355. https://doi.org/10.1016/j.carbpol.2021.118355

Liu, T., Gou, S., He, Y., Fang, S., Zhou, L., Gou, G., & Liu, L. (2021). N-methylene phosphonic chitosan aerogels for efficient capture of Cu2+ and Pb2+ from aqueous environment. *Carbohydrate Polymers*, *269*, 118355–118355. https://doi.org/10.1016/j.carbpol.2021.118355

Liu, X., Shan, Y., Zhang, S., Kong, Q., & Pang, H. (2023). Application of metal organic framework in wastewater treatment. *Green Energy & Environment*, *8*(3), 698–721. https://doi.org/10.1016/j.gee.2022.03.005

Liu, Y., Zhou, Y., Tang, Q., Li, Q., Chen, S., Sun, Z., & Wang, H. (2020). A direct Z -scheme Bi 2 WO 6 /NH 2 -UiO-66 nanocomposite as an efficient visible-light-driven photocatalyst for NO removal. *RSC Advances*, *10*(3), 1757–1768. https://doi.org/10.1039/c9ra09270f.

Long, J. R., & Yaghi, O. M. (2009). The pervasive chemistry of metal-organic frameworks. Chemical Society Reviews, *38*, 1213–1214. https://doi.org/10.1039/B903811F.

Long, R., Yu, Z., Shan, M., Feng, X., Zhu, X., Li, X., & Wang, P. (2022). The easy-recoverable 3D Ni/Fe-LDH-SA gel ball encapsulated by sodium alginate is used to remove Ni2+ and Cu2+ in water samples. Colloids and Surfaces. *A, Physicochemical and Engineering Aspects*, *634*, 127942. https://doi.org/10.1016/j.colsurfa.2021.127942

Lu, Y., Huang, Y., Cao, J., Li, H., Ho, W., & Lee, S. C. (2019). Constructing Z-scheme SnO2/N-doped carbon quantum dots/ZnSn(OH)6 nanohybrids with high redox ability for NOx removal under VIS-NIR light. *Journal of Materials Chemistry A*, *7*(26), 15782–15793. https://doi.org/10.1039/c9ta03504d.

Łuczak, J., Kroczewska, M., Baluk, M., Sowik, J., Mazierski, P., & Zaleska-Medynska, A. (2023). Morphology control through the synthesis of metal-organic frameworks. *Advances in Colloid and Interface Science*, *314*, 102864–102864. https://doi.org/10.1016/j.cis.2023.102864.

Luo, S., Zhang, C., Liu, X., Li, Y., Tang, L., Fu, M., Wang, S., Wu, J., Xu, M., Wang, X., & He, Y. (2022). Protonated NH2-MIL-125 via HCl vapor to introduce the moiety with charge and ample hydrogen as a novel bifunctional photocatalyst: Enhanced photocatalytic H2 production and NO purification. *Chemical Engineering Journal*, *432*, 134244. https://doi.org/10.1016/j.cej.2021.134244.

Lv, S.-W., Liu, J.-M., Li, C.-Y., Zhao, N., Wang, Z.-H., & Wang, S. (2019). A novel and universal metal-organic frameworks sensing platform for selective detection and efficient removal of heavy metal ions. *Chemical Engineering Journal (Lausanne, Switzerland : 1996)*, *375*, 122111. https://doi.org/10.1016/j.cej.2019.122111

Lyu, J., Zhang, X., Chen, Z., Anderson, R., Wang, X., Wasson, M. C., Bai, P., Guo, X., Islamoglu, T., Gómez-Gualdrón, D. A., & Farha, O. K. (2019). Modular Synthesis of Highly Porous Zr-MOFs Assembled from Simple Building Blocks for Oxygen Storage. *ACS Applied Materials & Interfaces*, *11*(45), 42179–42185. https://doi.org/10.1021/acsami.9b14439.

Ma, X., Wang, L., Zhang, Q., & Jiang, H. (2019). Switching on the Photocatalysis of Metal–Organic Frameworks by Engineering Structural Defects. *Angewandte Chemie International Edition*, *58*(35), 12175–12179. https://doi.org/10.1002/anie.201907074

Margariti, S. Rapti, A. Katsenis, T. Friši, Y. Georgiou, M. Manos, G. S. Papaefstathiou, Cu2+ sorption from aqueous media by a recyclable Ca2+ framework, *Inorg. Chem. Front*. *4* (2017) 773-781. https://doi.org/10.1039/C6QI00542J.

Marimuthu, M., Arumugam, S. S., Sabarinathan, D., Li, H., & Chen, Q. (2021). Metal-organic frameworks in food safety. Trends in Food Science & Technology, *116*, 1002–1028. https://doi.org/10.1016/j.tifs.2021.08.015.

Marshall, R. J., Lennon, C. T., Tao, A., Senn, H. M., Wilson, C., Fairen-Jimenez, D., & Forgan, R. S. (2017). Controlling interpenetration through linker conformation in the modulated synthesis of Sc metal–organic frameworks. *Journal of Materials Chemistry A, 6*(3), 1181–1187. https://doi.org/10.1039/c7ta09699b.

Martinez, V., Stolar, T., Karadeniz, B., Brekalo, I., & Užarević, K. (2023). Advancing mechanochemical synthesis by combining milling with different energy sources. *Nature Reviews. Chemistry*, *7*(1), 51–65. https://doi.org/10.1038/s41570-022-00442-1

Matlinska, M. A., Ha, M., Hughton, B., Oliynyk, A. O., Iyer, A. K., Bernard, G. M., Lambkin, G., Lawrence, M. C., Katz, M. J., Mar, A., & Michaelis, V. K. (2019). Alkaline Earth Metal–Organic Frameworks with Tailorable Ion Release: A Path for Supporting Biomineralization. *ACS Applied Materials & Interfaces*, *11*(36), 32739–32745. https://doi.org/10.1021/acsami.9b11004

Mazumder, A., Sebastian, E., & Hariharan, M. (2022). Solvent dielectric delimited nitro-nitrito photorearrangement in a perylenediimide derivative. *Chemical Science (Cambridge), 13*(3), 886–887. https://doi.org/10.1039/d2sc02979k.

Murray, L. J., Dinc, M., & Long, J. R. (2009). Hydrogen storage in metal-organic frameworks. *Chemical Society Reviews*, *38*(5), 1294–1314. https://doi.org/10.1039/b802256a

Mustapha, S., Shuaib, D. T., Ndamitso, M. M., Etsuyankpa, M. B., Sumaila, A., Mohammed, U. M., & Nasirudeen, M. B. (2019). Adsorption isotherm, kinetic and thermodynamic studies for the removal of Pb(II), Cd(II), Zn(II) and Cu(II) ions from aqueous solutions using Albizia lebbeck pods. *Applied Water Science*, *9*(6), 1–11. https://doi.org/10.1007/s13201-019-1021-x.

Navarathna, C. M., Dewage, N. B., Karunanayake, A. G., Farmer, E. L., Perez, F., Hassan, E. B., Mlsna, T. E., & Pittman, C. U. (2020). Rhodamine B Adsorptive Removal and Photocatalytic Degradation on MIL-53-Fe MOF/Magnetic Magnetite/Biochar Composites. *Journal of Inorganic and Organometallic Polymers and Materials*, *30*(1), 214–229. https://doi.org/10.1007/s10904-019-01322-w

Øien-ØDegaard, S., Shearer, G. C., Wragg, D. S., & Lillerud, K. P. (2017). Pitfalls in metal-organic framework crystallography: Towards more accurate crystal structures. *Chemical Society Reviews*, *46*(16), 4867–4876. https://doi.org/10.1039/c6cs00533k

Phan, A., Czaja, A. U., Gándara, F., Knobler, C. B., & Yaghi, O. M. (2011). Metal–Organic Frameworks of Vanadium as Catalysts for Conversion of Methane to Acetic Acid. *Inorganic Chemistry*, *50*(16), 7388–7390. https://doi.org/10.1021/ic201396m.

Poozhikunnath, A., Yu, H., Bonville, L., Myles, T., & Maric, R. (2019). Characterization and evaluation of Fe–N–C electrocatalysts for oxygen reduction directly synthesized by reactive spray deposition technology. *Journal of Materials Science*, *55*(4), 1673–1691. https://doi.org/10.1007/s10853-019-04124-0.

Qin, X., Tan, H., Zhao, Y., Cheng, S., Zhou, M., Lin, J., Ho, W.-K., Li, H., & Lee, S.-C. (2023). Light-Emitting Diode Visible-Light-Driven Photocatalytic Redox Reactions in Nitrogen Oxide Removal Using β-Bi2O3/Bi/g-C3N4 Prepared by One-Step In Situ Thermal Reduction Synthesis. *Advanced Energy and Sustainability Research*, *4*(1). https://doi.org/10.1002/aesr.202200157

Radha, R., Kulangara, R. V., Elaiyappillai, E., Sridevi, J., & Balakumar, S. (2019). Modulation in the Band Dispersion of Bi2WO6 Nanocrsytals Using the Electronegativity of Transition Elements for Enhanced Visible Light Photocatalysis. *Crystal Growth & Design*, *19*(11), 6224–6238. https://doi.org/10.1021/acs.cgd.9b00707

Raji, Z., Karim, A., Karam, A., & Khalloufi, S. (2023). Adsorption of Heavy Metals: Mechanisms, Kinetics, and Applications of Various Adsorbents in Wastewater Remediation—A Review. *Waste*, *1*(3), 775–805. https://doi.org/10.3390/waste1030046

Rao, P. C., Asha, K. S., & Mandal, S. (2014). Synthesis, structure and band gap energy of a series of thermostable alkaline earth metal based metal-organic frameworks. *CrystEngComm*, *16*(39), 9320–9325. https://doi.org/10.1039/c4ce01505c

Rao, Z., Feng, K., Tang, B., & Wu, P. (2017). Surface Decoration of Amino-Functionalized Metal–Organic Framework/Graphene Oxide Composite onto Polydopamine-Coated Membrane Substrate for Highly Efficient Heavy Metal Removal. *ACS Applied Materials & Interfaces*, *9*(3), 2594–2605. https://doi.org/10.1021/acsami.6b15873

Rao, Z., Feng, K., Tang, B., & Wu, P. (2017). Surface Decoration of Amino-Functionalized Metal–Organic Framework/Graphene Oxide Composite onto Polydopamine-Coated Membrane Substrate for Highly Efficient Heavy Metal Removal. *ACS Applied Materials & Interfaces*, *9*(3), 2594–2605. https://doi.org/10.1021/acsami.6b15873

Rastogi, A., Tiwari, M. K., & Ghangrekar, M. M. (2021). A review on environmental occurrence, toxicity and microbial degradation of Non-Steroidal Anti-Inflammatory Drugs (NSAIDs). *Journal of Environmental Management*, *300*, 113694–113694. https://doi.org/10.1016/j.jenvman.2021.113694

Saadi, R., Saadi, Z., Fazaeli, R., & Fard, N. E. (2015). Monolayer and multilayer adsorption isotherm models for sorption from aqueous media. *The Korean Journal of Chemical Engineering*, *32*(5), 787–799. https://doi.org/10.1007/s11814-015-0053-7.

Sadler, P. J., Li, H., & Sun, H. (1999). Medicinal inorganic chemistry: Perspectives and challenges. Coordination Chemistry Reviews, *185*, 689–709. https://doi.org/10.1016/S0010-8545(99)00018-1.

Samghouli, N., Regraguy, B., Abahdou, F., Azoulay, K., Bencheikh, I., Mabrouki, J., & Hajjaji, S. E. (2022). Removal of a non-steroidal anti-inflammatory drug (Piroxicam) in an aqueous medium by an agricultural by-product. *E3S Web of Conferences*, *337*, 05001. https://doi.org/10.1051/e3sconf/202233705001.

Sanselme, M., Grenèche, J.-M., Riou-Cavellec, M., & Férey, G. (2004). The first ferric carboxylate with a three-dimensional hydrid open-framework (MIL-82): its synthesis, structure, magnetic behavior and study of its dehydration by Mössbauer spectroscopy. *Solid State Sciences*, *6*(8), 853–858. https://doi.org/10.1016/j.solidstatesciences.2004.04.001

Santhamoorthy, M., Thirupathi, K., Periyasamy, T., Thirumalai, D., Ramkumar, V., Asrafali, S., & Kim, S.-C. (2022). Synthesis of bifunctional groups-integrated mesoporous silica hybrid adsorbent for simultaneous removal of Hg2+ and Cu2+ ions from aqueous solution. *Surfaces and Interfaces*, *29*, 101808. https://doi.org/10.1016/j.surfin.2022.101808

Sarker, M., Song, J. Y., & Jhung, S. H. (2017). Adsorptive removal of anti-inflammatory drugs from water using graphene oxide/metal-organic framework composites. *Chemical Engineering Journal*, *335*, 74–81. https://doi.org/10.1016/j.cej.2017.10.13.

Schaate, A., Roy, P., Godt, A., Lippke, J., Waltz, F., Wiebcke, M., & Behrens, P. (2018). Modulated synthesis of ZR-based metal-organic frameworks: From nano to single crystals. *Chemistry*. https://pub.uni-bielefeld.de/record/2307277.

Schejn, A., Balan, L., Falk, V., Aranda, L., Medjahdi, G., & Schneider, R. (2014). Controlling ZIF-8 nano- and microcrystal formation and reactivity through zinc salt variations. *CrystEngComm*, *16*(21), 4493–4500. https://doi.org/10.1039/c3ce42485e

Sellaoui, L., Silva, L. F., Badawi, M., Ali, J., Favarin, N., Dotto, G. L., Erto, A., & Chen, Z. (2021). Adsorption of ketoprofen and 2- nitrophenol on activated carbon prepared from winery wastes: A combined experimental and theoretical study. *Journal of Molecular Liquids, 333,* 115906. https://doi.org/10.1016/j.molliq.2021.115906.

Seo, P. W., Bhadra, B. N., Ahmed, I., Khan, N. A., & Jhung, S. H. (2016). Adsorptive Removal of Pharmaceuticals and Personal Care Products from Water with Functionalized Metal-organic Frameworks: Remarkable Adsorbents with Hydrogen-bonding Abilities. *Scientific Reports*, *6*(1), 34462-. https://doi.org/10.1038/srep34462

Seo, Y. S., Khan, N. A., & Jhung, S. H. (2015). Adsorptive removal of methylchlorophenoxypropionic acid from water with a metal-organic framework. *Chemical Engineering Journal*, *270*, 22–27. https://doi.org/10.1016/j.cej.2015.02.007

Shao, J., Shao, P., Peng, M., Li, M., Yao, Z., Xiong, X., Qiu, C., Zheng, Y., Yang, L., & Luo, X. (2023). A pyrazine based metal-organic framework for selective removal of copper from strongly acidic solutions. *Frontiers of Environmental Science & Engineering*, *17*(3), 33. https://doi.org/10.1007/s11783-023-1633-0.

Sheldrick, G. M. (2015). Crystal structure refinement with SHELXL. *Acta Crystallographica. Section C, Crystal Structure Communications*, *71*(1), 3–8. https://doi.org/10.1107/S2053229614024218.

Sheldrick, G. M. (2015). SHELXT– Integrated space-group and crystal-structure determination. *Acta Crystallographica. Section A, Foundations and Advances*, *71*(1), 3–8. https://doi.org/10.1107/S2053273314026370.

Shen, W., Guo, X., & Pang, H. (2022). Effect of Solvothermal Temperature on Morphology and Supercapacitor Performance of Ni-MOF. *Molecules (Basel, Switzerland)*, *27*(23), 8226. https://doi.org/10.3390/molecules27238226.

Shi, B., Zhang, X., Li, W., Liang, N., Hu, X., Xiao, J., Wang, D., Zou, X., & Shi, J. (2023). Metal-organic frameworks for food safety. Food Chemistry, *400*, 133995. https://doi.org/10.1016/j.foodchem.2023.133995.

Sholl, D. S., & Lively, R. P. (2015). Defects in Metal–Organic Frameworks: Challenge or Opportunity? *The Journal of Physical Chemistry Letters*, *6*(17), 3437–3444. https://doi.org/10.1021/acs.jpclett.5b01135

Sing, K. S. W. (1985). Reporting physisorption data for gas/solid systems with special reference to the determination of surface area and porosity (Recommendations 1984). *Pure and Applied Chemistry*, *57*(4), 603–619. https://doi.org/10.1351/pac198557040603.

Sing, K. S., & Williams, R. T. (2004b). Physisorption hysteresis loops and the characterization of nanoporous materials. *Adsorption Science & Technology*, *22*(10), 773–782. https://doi.org/10.1260/0263617053499032.

Singh, S., Sahoo, R. K., Shinde, N. M., Yun, J. M., Mane, R. S., Chung, W., & Kim, K. H. (2019). Asymmetric faradaic assembly of Bi 2 O 3 and MnO 2 for a high-performance hybrid electrochemical energy storage device. *RSC Advances*, *9*(55), 32154–32164. https://doi.org/10.1039/c9ra06331e.

Soni, A., Sharma, R., Rana, D. S., Singh, D., & Gupta, N. (2023). Structural designs of functional metal organic frameworks for the detection of mercury in contaminated water sources. *Coordination Chemistry Reviews*, *494*, 215343. https://doi.org/10.1016/j.ccr.2023.215343

Stock, N., & Biswas, S. (2012). Synthesis of Metal-Organic Frameworks (MOFs): Routes to Various MOF Topologies, Morphologies, and Composites. *Chemical Reviews*, *112*(2), 933–969. https://doi.org/10.1021/cr200304e.

Subramaniyam, V., Thangadurai, T. D., & Lee, Y. I. (2022). Zirconium based metal-organic framework for the adsorption of Cu (II) ions in real water samples. *Cleaner Engineering and Technology*, *9*, 100526. https://doi.org/10.1016/j.clet.2022.100526.

Sun, D., Liu, W., Qiu, M., Zhang, Y., & Li, Z. (2015). Introduction of a mediator for enhancing photocatalytic performance via post-synthetic metal exchange in metal-organic frameworks (MOFs). *Chemical Communications (Cambridge, England)*, *51*(11), 2056–2059. https://doi.org/10.1039/c4cc09407g.

Sun, J., Wan, J., Wang, Y., Yan, Z., Ma, Y., Ding, S., Tang, M., & Xie, Y. (2022). Modulated construction of Fe-based MOF via formic acid modulator for enhanced degradation of sulfamethoxazole：Design, degradation pathways, and mechanism. *Journal of Hazardous Materials*, *429*, 128299–128299. https://doi.org/10.1016/j.jhazmat.2022.128299.

Sun, K., & Jiang, H.-L. (2024). A dynamic metal–organic framework photocatalyst. *Nature Chemistry*, *16*(10), 1580–1581. https://doi.org/10.1038/s41557-024-01607-9.

Sun, X.-F., Xie, Y., Shan, S., Li, W., & Sun, L. (2022). Chemically-Crosslinked Xylan/Graphene Oxide Composite Hydrogel for Copper Ions Removal. *Journal of Polymers and the Environment*, *30*(9), 3999–4013. https://doi.org/10.1007/s10924-022-02475-5.

Tan, B. J., Klabunde, K. J., & Sherwood, P. M. A. (1990). X-ray Photoelectron Spectroscopy Studies of Solvated Metal Atom Dispersed Catalysts. Monometallic Iron and

Bimetallic Iron-Cobalt Particles on Alumina. *Chemistry of Materials*, *2*(2), 186–191. https://doi.org/10.1021/cm00008a021.

Thelusmond, J.-R., Kawka, E., Strathmann, T. J., & Cupples, A. M. (2018). Diclofenac, carbamazepine and triclocarban biodegradation in agricultural soils and the microorganisms and metabolic pathways affected. *The Science of the Total Environment*, *640–641*, 1393–1410. https://doi.org/10.1016/j.scitotenv.2018.05.403.

Thirumurugan, A., & Cheetham, A. K. (2010). Anionic Metal-Organic Frameworks of Bismuth Benzenedicarboxylates: Synthesis, Structure and Ligand-Sensitized Photoluminescence. *European Journal of Inorganic Chemistry*, *2010*(24), 3823–3828. https://doi.org/10.1002/ejic.201000535.

Tian, H., Araya, T., Li, R., Fang, Y., & Huang, Y. (2019). Removal of MC-LR using the stable and efficient MIL-100/MIL-53 (Fe) photocatalyst: The effect of coordinate immobilized layers. *Applied Catalysis. B, Environmental*, *254*, 371–379. https://doi.org/10.1016/j.apcatb.2019.04.086.

Ulrich, N., Goss, K., & Ebert, A. (2021). Exploring the octanol–water partition coefficient dataset using deep learning techniques and data augmentation. *Communications Chemistry*, *4*(1). https://doi.org/10.1038/s42004-021-00528-9.

Van Vleet, M. J., Weng, T., Li, X., & Schmidt, J. R. (2018). In Situ, Time-Resolved, and Mechanistic Studies of Metal–Organic Framework Nucleation and Growth. *Chemical Reviews*, *118*(7), 3681–3721. https://doi.org/10.1021/acs.chemrev.7b00582.

Wang, B., Chen, D., Li, N., Xu, Q., Li, H., He, J., & Lu, J. (2021). Enhanced photocatalytic oxidation of nitric oxide to MOF-derived hollow bimetallic oxide microcubes supported on g-C3N4 nanosheets via p–n heterojunction. *Industrial & Engineering Chemistry Research*, *60*(7), 2921-2930. https://doi.org/10.1021/acs.iecr.0c05834.

Wang, G., Sun, Q., Liu, Y., Huang, B., Dai, Y., Zhang, X., & Qin, X. (2014). A Bismuth-Based Metal–Organic framework as an efficient Visible-Light-Driven photocatalyst. *Chemistry - a European Journal*, *21*(6), 2364–2367. https://doi.org/10.1002/chem.201405047.

Wang, S., Ding, X., Yang, N., Zhan, G., Zhang, X., Dong, G., Zhang, L., & Chen, H. (2020). Insight into the effect of bromine on facet-dependent surface oxygen vacancies construction and stabilization of Bi2MoO6 for efficient photocatalytic NO removal. *Applied Catalysis. B, Environmental*, *265*, 118585. https://doi.org/10.1016/j.apcatb.2019.118585.

Wang, Y., & Zhang, L. (2020). Improved performance of 3D hierarchical NiAl-LDHs micro-flowers via a surface anchored ZIF-8 for rapid multiple-pollutants simultaneous removal and residues monitoring. *Journal of Hazardous Materials*, *395*, 122635. https://doi.org/10.1016/j.jhazmat.2020.122635.

Wang, Y., Jiang, W., Yao, W., Liu, Z., Liu, Z., Wang, Y., Shi, L., & Gao, L. (2021). BiNV bond: A hole-transfer bridge for high-efficient separation and transfer of carriers. *Journal of Colloid and Interface Science*, *590*, 144–153. https://doi.org/10.1016/j.jcis.2021.01.043.

Wang, Y., Lü, Y., Zhan, W., Xie, Z., Kuang, Q., & Zheng, L. (2015). Synthesis of porous Cu2O/CuO cages using Cu-based metal–organic frameworks as templates and their gas-sensing properties. *Journal of Materials Chemistry A*, *3*(24), 12796–12803. https://doi.org/10.1039/c5ta01108f.

Williams, C. A., Blake, A. J., Wilson, C., Hubberstey, P., & Schröder, M. (2008). Novel Metal−Organic Frameworks Derived from Group II Metal Cations and Aryldicarboxylate Anionic Ligands. *Crystal Growth & Design*, *8*(3), 911–922. https://doi.org/10.1021/cg700731d.

Wu, C., & Au, V. K.-M. (2024). Efficient removal of piroxicam and ketoprofen by acid-modulated iron(III) metal–organic frameworks. *Journal of Industrial and Engineering Chemistry* (Seoul, Korea), *129*, 544–554. https://doi.org/10.1016/j.jiec.2023.09.013.

Wu, C., Low, K.-H., & Au, V. K.-M. (2023). Efficient removal and sensing of copper(II) ions by alkaline earth metal-based metal–organic frameworks. *Journal of Solid State Chemistry*, *322*, 123936. https://doi.org/10.1016/j.jssc.2023.123936.

Wu, X., Yue, H., Zhang, Y., Gao, X., Li, X., Wang, L., Cao, Y., Hou, M., An, H., Zhang, L., Li, S., Ma, J., Lin, H., Fu, Y., Gu, H., Lou, W., Wei, W., Zare, R. N., & Ge, J. (2019). Packaging and delivering enzymes by amorphous metal-organic frameworks. *Nature Communications*, *10*(1), 5165–5168. https://doi.org/10.1038/s41467-019-13153-x.

Wu, X., Yue, H., Zhang, Y., Gao, X., Li, X., Wang, L., Cao, Y., Hou, M., An, H., Zhang, L., Li, S., Ma, J., Lin, H., Fu, Y., Gu, H., Lou, W., Wei, W., Zare, R. N., & Ge, J. (2019). Enzyme-MOF nanoreactors for biomedical applications. Nature Communications, *10*, 5165–5168. https://doi.org/10.1038/s41467-019-13152-y.

Wu, Y., Li, Y., Zhao, T., Wang, X., Isaeva, V. I., Kustov, L. M., Yao, J., & Gao, J. (2022). Bimetal-organic framework-derived nanotube@cellulose aerogels for peroxymonosulfate (PMS) activation. *Carbohydrate Polymers*, *296*, 119969–119969. https://doi.org/10.1016/j.carbpol.2022.119969.

Xian, H., Zhu, J., Tan, W., Tang, H., Liu, P., Zhu, R., Liang, X., Wei, J., He, H., & Teng, H. H. (2018). The mechanism of defect induced hydroxylation on pyrite surfaces and implications for hydroxyl radical generation in prebiotic chemistry. *Geochimica Et Cosmochimica Acta*, *244*, 163–172. https://doi.org/10.1016/j.gca.2018.10.009.

Xiao, S., Pan, D., Liang, R., Dai, W., Zhang, Q., Zhang, G., Su, C., Li, H., & Chen, W. (2018). Bimetal MOF derived mesocrystal ZnCo2O4 on rGO with High performance in visible-light photocatalytic NO oxidization. *Applied Catalysis. B, Environmental*, *236*, 304–313. https://doi.org/10.1016/j.apcatb.2018.05.033.

Xiao, Y., Guo, X., Liu, J., Liu, L., Zhang, F., & Li, C. (2019). Development of a bismuth-based metal-organic framework for photocatalytic hydrogen production. *Chinese Journal of Catalysis*, *40*(9), 1339–1344. https://doi.org/10.1016/S1872-2067(19)63329-2.

Xie, D., Wang, S., Li, S., Yang, W., & Feng, Y.-S. (2022). A two-dimensional Bi-based porphyrin metal-organic framework photocatalyst for white light-driven selective oxidation of sulfides. *Catalysis Science & Technology*, *12*(1), 3254–3326. https://doi.org/10.1039/d2cy00387b.

Xin, Y., Zhu, Q., Gao, T., Li, X., Zhang, W., Wang, H., Ji, D., Huang, Y., Padervand, M., Yu, F., & Wang, C. (2023). Photocatalytic NO removal over defective Bi/BiOBr nanoflowers: The inhibition of toxic NO2 intermediate via high humidity. *Applied Catalysis. B, Environmental*, *324*, 122238. https://doi.org/10.1016/j.apcatb.2022.122238.

Xing, J., Schweighauser, L., Okada, S., Harano, K., & Nakamura, E. (2019). Atomically precise nanoclusters for catalysis. Nature Communications, *10*, 3608–3609. https://doi.org/10.1038/s41467-019-11547-5.

Xiong, W., Zeng, G., Yang, Z., Zhou, Y., Zhang, C., Cheng, M., Liu, Y., Hu, L., Wan, J., Zhou, C., Xu, R., & Li, X. (2018). Adsorption of tetracycline antibiotics from aqueous solutions on nanocomposite multi-walled carbon nanotube functionalized MIL-53(Fe) as new adsorbent. *The Science of the Total Environment*, *627*, 235–244. https://doi.org/10.1016/j.scitotenv.2018.01.249.

Xu, H., Zhong, F., Chen, F., Luan, T., Li, P., Xu, S., & Gao, J. (2022). A Zr-MOF nanoflower sensor and its mixed-matrix membrane for the highly sensitive detection of nitroaromatics. *Journal of Materials Chemistry C*, *10*(19), 7469–7475. https://doi.org/10.1039/d2tc00920j.

Xu, J., Teng, Y., & Teng, F. (2016). Effect of Surface Defect States on Valence Band and Charge Separation and Transfer Efficiency. *Scientific Reports*, *6*(1), 32457–32457. https://doi.org/10.1038/srep32457.

Xu, R., Jian, M., Ji, Q., Hu, C., Tang, C., Liu, R., Zhang, X., & Qu, J. (2020). 2D water-stable zinc-benzimidazole framework nanosheets for ultrafast and selective removal of heavy metals. *Chemical Engineering Journal (Lausanne, Switzerland : 1996)*, *382*, 122658-. https://doi.org/10.1016/j.cej.2019.122658.

Yaghi, M., O'Keeffe, M., Ockwig, N. W., Chae, H. K., Eddaoudi, M., & Kim, J. (2003). Reticular synthesis and the design of new materials. Nature, *423*, 705–714. https://doi.org/10.1038/nature01650.

Yaghi, O. M., Li, H., Eddaoudi, M., & O'Keeffe, M. (1999). Design and synthesis of an exceptionally stable and highly porous metal-organic framework. *Nature (London)*, *402*(6759), 276–279. https://doi.org/10.1038/46248.

Yaghi, O. M., O'Keeffe, M., Ockwig, N. W., Chae, H. K., Eddaoudi, M., & Kim, J. (2003). Reticular synthesis and the design of new materials. *Nature (London)*, *423*(6941), 705–714. https://doi.org/10.1038/nature01650.

Yang, H., Zhao, Y., Guo, Y., Wu, B., Ying, Y., Sofer, Z., & Wang, S. (2023). Surfactant-Mediated crystalline structure evolution enabling the ultrafast green synthesis of Bismuth-MOF in aqueous condition. *Small*, *20*(15). https://doi.org/10.1002/smll.202307484.

Yang, Q., Sun, X., Sun, Y., Shen, X., & Pang, Y. (2023). Bismuth Metal–Organic Framework/Carbon Nanosphere Composites for Ultrasensitive Simultaneous

Electrochemical Detection of Lead and Cadmium. *ACS Applied Nano Materials*, *6*(9), 7901–7909. https://doi.org/10.1021/acsanm.3c01096.

Yang, Y., Zheng, Z., Ji, W., Xu, J., & Zhang, X. (2020). Insights to perfluorooctanoic acid adsorption micro-mechanism over Fe-based metal organic frameworks: Combining computational calculation with response surface methodology. *Journal of Hazardous Materials, 395*, 122686. https://doi.org/10.1016/j.jhazmat.2020.122686.

You, Z., Wang, C., Xiao, Y., Guan, Q., Li, J., Xing, Y., Gao, H., Sun, L., & Bai, F. (2021). Integrated Photoresponsive Alkaline Earth Metal Coordination Networks: synthesis, Topology, Photochromism and Photoluminescence investigation. *Chemistry - a European Journal*, *27*(37), 9605–9619. https://doi.org/10.1002/chem.202100588.

Yu, C., Shao, Z., Liu, L., & Hou, H. (2018). Efficient and Selective Removal of Copper(II) from Aqueous Solution by a Highly Stable Hydrogen-Bonded Metal–Organic Framework. *Crystal Growth & Design*, *18*(5), 3082–3088. https://doi.org/10.1021/acs.cgd.8b00224.

Yusuf, V. F., Malek, N. I., & Kailasa, S. K. (2022). Review on Metal–Organic Framework Classification, Synthetic Approaches, and Influencing Factors: Applications in Energy, Drug Delivery, and Wastewater Treatment. *ACS Omega*, *7*(49), 44507−44531. https://doi.org/10.1021/acsomega.2c05310.

Zahn, G., Zerner, P., Lippke, J., Kempf, F. L., Lilienthal, S., Schröder, C. A., Schneider, A. M., & Behrens, P. (2014). Insight into the mechanism of modulated syntheses: In situ synchrotron diffraction studies on the formation of Zr-fumarate MOF. *CrystEngComm*, *16*(39), 9198–9207. https://doi.org/10.1039/c4ce01095g.

Zelepukin, I. V., Griaznova, O. Y., Shevchenko, K. G., Ivanov, A. V., Baidyuk, E. V., Serejnikova, N. B., Volovetskiy, A. B., Deyev, S. M., & Zvyagin, A. V. (2022).

Nanoparticle-based theranostics for biomedical applications. Nature Communications, *13*, 6910. https://doi.org/10.1038/s41467-022-34591-0.

Zhang, F., Zou, X., Gao, X., Fan, S., Sun, F., Ren, H., & Zhu, G. (2012). Hydrogen Selective NH2-MIL-53(Al) MOF Membranes with High Permeability. *Advanced Functional Materials*, *22*(17), 3583–3590. https://doi.org/10.1002/adfm.201200084.

Zhang, H., Shi, Z., Wang, X., Xu, X., Tang, Y., Liu, X., Tian, L., Xiao, Y., Wu, Z., Wang, H., & Yang, Y. (2023). Insights into the synthesis of monolithic and structured graphene bulks and its application for Cu2+ ions removal from aqueous solution. *Separation and Purification Technology*, *308*, 122847. https://doi.org/10.1016/j.seppur.2022.122847.

Zhang, J., White, G. B., Ryan, M. D., Hunt, A. J., & Katz, M. J. (2016). Dihydrolevoglucosenone (Cyrene) As a Green Alternative to N,N-Dimethylformamide (DMF) in MOF Synthesis. *ACS Sustainable Chemistry & Engineering*, *4*(12), 7186–7192. https://doi.org/10.1021/acssuschemeng.6b02115.

Zhang, P., Huang, Y., Rao, Y., Chen, M., Li, X., Ho, W., Lee, S., & Cao, J. (2021). Chemical etching fabrication of uniform mesoporous Bi@Bi2O3 nanospheres with enhanced visible light-induced photocatalytic oxidation performance for NOx. *Chemical Engineering Journal (Lausanne, Switzerland : 1996)*, *406*, 126910. https://doi.org/10.1016/j.cej.2020.126910.

Zhang, X., Bao, T., Wei, F., & Wang, S. (2022). Zeotype porous coordination networks as potential adsorbents for removing nonsteroidal anti-inflammatory drugs from water. *Colloids and Surfaces a Physicochemical and Engineering Aspects*, *640*, 128401. https://doi.org/10.1016/j.colsurfa.2022.128401.

Zhang, X., Yu, T., & Au, V. K. (2022). Photoresponsive Metal-Organic Frameworks: Tailorable Platforms of Photoswitches for Advanced Functions. *ChemNanoMat, 8*(3). https://doi.org/10.1002/cnma.202100486.

Zhang, X., Yu, T., & Au, V. K. (2022). Photoresponsive Metal-Organic Frameworks: Tailorable Platforms of Photoswitches for Advanced Functions. *ChemNanoMat : Chemistry of Nanomaterials for Energy, Biology and More*, *8*(3). https://doi.org/10.1002/cnma.202100486.

Zhang, Z., Chen, Y., Wang, Z., Hu, C., Ma, D., Chen, W., & Ao, T. (2020). Effective and structure-controlled adsorption of tetracycline hydrochloride from aqueous solution by using Fe-based metal-organic frameworks. *Applied Surface Science*, 542, 148662. https://doi.org/10.1016/j.apsusc.2020.148662.

Zhao, L., Duan, X., Azhar, M. R., Sun, H., Fang, X., & Wang, S. (2020). Selective adsorption of rare earth ions from aqueous solution on metal-organic framework HKUST-1. *Chemical Engineering Journal Advances*, *1*, 100009. https://doi.org/10.1016/j.ceja.2020.100009.

Zhao, X., Gao, X., Zhang, Y., Wang, M., Gao, X., & Liu, B. (2022). Construction of dual sulfur sites in metal–organic framework for enhanced mercury(II) removal. *Journal of Colloid and Interface Science*, 631, 191–201. https://doi.org/10.1016/j.jcis.2022.10.153.

Zhao, X., Zheng, M., Gao, X., Zhang, J., Wang, E., & Gao, Z. (2021). The application of MOFs-based materials for antibacterials adsorption. *Coordination Chemistry Reviews*, 440, 213970. https://doi.org/10.1016/j.ccr.2021.213970.

Zhou, H. C., Long, J. R., & Yaghi, O. M. (2012). Introduction to Metal–Organic Frameworks. *Chemical Reviews*, *112*(2), 673–674. https://doi.org/10.1021/cr300014x.

Zhou, H.-C., Long, J. R., & Yaghi, O. M. (2012). Introduction to metal-organic frameworks. Chemical Reviews, *112*, 673–674. https://doi.org/10.1021/cr300014x.

Zhou, L., Li, N., Owens, G., & Chen, Z. (2019). Simultaneous removal of mixed contaminants, copper and norfloxacin, from aqueous solution by ZIF-8. *Chemical Engineering Journal (Lausanne, Switzerland : 1996)*, *362*, 628–637. https://doi.org/10.1016/j.cej.2019.01.068.

Zhou, M., Zeng, L., Li, R., Yang, C., Qin, X., Ho, W., & Wang, X. (2022). Poly(heptazine imide) with Enlarged Interlayers Spacing for Efficient Photocatalytic NO Decomposition. *Applied Catalysis. B, Environmental*, *317*, 121719. https://doi.org/10.1016/j.apcatb.2022.121719.

Zhu, Y., Xu, Z., Yan, K., Zhao, H., & Zhang, J. (2017). One-Step Synthesis of CuO–Cu2O Heterojunction by Flame Spray Pyrolysis for Cathodic Photoelectrochemical Sensing of l-Cysteine. *ACS Applied Materials & Interfaces*, *9*(46), 40452–40460. https://doi.org/10.1021/acsami.7b13020.

Zhuang, S., Cheng, R., & Wang, J. (2018). Adsorption of diclofenac from aqueous solution using UiO-66-type metal-organic frameworks. *Chemical Engineering Journal*, 359, 354–362. https://doi.org/10.1016/j.cej.2018.11.150.

Zou, Z., Du, Z., Dai, L., Liu, D., & Du, W. (2024). Crystallization mechanisms and size control of metal-organic frameworks: Insights and applications. *Chemical Engineering Journal*, *480*, 148260. https://doi.org/10.1016/j.cej.2023.148260.

Appendix I

Inclusion of Publications Statement

EdUHK is supportive of candidates publishing their research results during their candidature as detailed in the EdUHK Thesis Examination Procedure.

For each publication included in the folio, provide all of the requested details and signature(s) required. Use one box for each publication.

Details of publication:
Full title: Efficient removal and sensing of copper(II) ions by alkaline earth metal-based metal–organic frameworks
Authors: Chen Wu, Kam-Hung Low, Vonika Ka-Man Au
Journal or book name: Journal of Solid State Chemistry
Volume/page numbers: 322/123936
Date accepted/published: 20 February 2023

***Status*[1]**	Published	√	Accepted and In press		In progress (Submitted)	

The Candidate's Contribution to the Work
Chen Wu: Methodology, Formal analysis, Investigation, Writing – original draft.

Candidate's Name Chen Wu	*Candidate's Signature*	*Date (dd/mm/yy)* 23 Jan 2025

Co-author's Contribution to the Work (Name of co-author: Kam-Hung Low**)**

Formal analysis, Investigation, Writing – review & editing

Co-author's Contribution to the Work (Name of co-author: Vonika Ka-Man Au**)**

Conceptualization, Formal analysis, Writing – review & editing, Supervision, Funding acquisition.

Co-authors' Declaration

I declare that:

- I have read the declaration from the all authors
- The information is correct and the description of their contribution is in accordance with my view

Co-author’s Name [2] Kam-Hung Low	*Co-author’s Signature*	*Date (dd/mm/yy)* *23 Jan 2025*
Co-author’s Name [2] Vonika Ka-Man Au	*Co-author’s*	*Date (dd/mm/yy)*

Candidate’s Declaration

I declare that:

- I have complied with the Thesis Examination Procedure
- The publications I have include in the folio meet the requirements for the submission of folios, and the publications are listed below.

Name Chen Wu	**Signature**	**Date (dd/mm/yy)** 23 Jan 2025

Details of publication:
Full title: Efficient removal of piroxicam and ketoprofen by acid-modulated iron(III) metal–organic frameworks
Authors: Chen Wu, Vonika Ka-Man Au
Journal or book name: Journal of Industrial and Engineering Chemistry
Volume/page numbers: 129/544-554
Date accepted/published: 11 September 2023

Status[1]	*Published*	√	**Accepted and In press**		**In progress (Submitted)**	

The Candidate’s Contribution to the Work
Chen Wu: Methodology, Formal analysis, Investigation, Writing – original draft.

Candidate’s Name Chen Wu	*Candidate’s Signature*	*Date (dd/mm/yy)* 23 Jan 2025

Co-author’s Contribution to the Work (Name of co-author: Vonika Ka-Man Au**)**

Conceptualization, Formal analysis, Writing – review & editing, Supervision, Funding acquisition.

Co-authors' Declaration

I declare that:

- I have read the declaration from the all authors
- The information is correct and the description of their contribution is in accordance with my view

Co-author's Name [2] Vonika Ka-Man Au	*Co-author's*	*Date (dd/mm/yy)* *23 Jan 2025*

Candidate's Declaration

I declare that:

- I have complied with the Thesis Examination Procedure
- The publications I have include in the folio meet the requirements for the submission of folios, and the publications are listed below.

Name Chen Wu	**Signature**	**Date (dd/mm/yy)** 23 Jan 2025

Details of publication:

Full title: Tunning bismuth metal-organic framework topology for enhanced photocatalytic NO oxidation

Authors: Chen Wu, Jincheng Mu, Xueying Wang, Pui-Yu Ho, Min Zhou, Can Yang, Chi-Fai Leung, Yu Huang, Wing-Kei Ho.

Journal or book name: Small

Volume/page numbers: Submitted

Date accepted/published: Submitted

Status[1]	*Published*	√	*Accepted and In press*		*In progress (Submitted)*	

The Candidate's Contribution to the Work

Chen Wu: Methodology, Formal analysis, Investigation, Writing – original draft.

Candidate's Name Chen Wu	*Candidate's Signature*	*Date (dd/mm/yy)* 23 Jan 2025

<table>
<tr><td colspan="3">Co-author’s Contribution to the Work (Name of co-author: Min Zhou)

Formal analysis, Investigation, Writing – review & editing</td></tr>
<tr><td colspan="3">Co-author’s Contribution to the Work (Name of co-author: Wing-Kei Ho)

Conceptualization, Formal analysis, Writing – review & editing, Supervision, Funding acquisition.</td></tr>
<tr><td colspan="3">Co-author’s Contribution to the Work (Name of co-author: Jincheng Mu)

Formal analysis, Investigation, – review & editing</td></tr>
<tr><td colspan="3">Co-author’s Contribution to the Work (Name of co-author: Xueying Wang)
Formal analysis, Investigation, – review & editing</td></tr>
<tr><td colspan="3">Co-author’s Contribution to the Work (Name of co-author: Pui-Yu Ho)
Formal analysis, Investigation, – review & editing</td></tr>
<tr><td colspan="3">Co-author’s Contribution to the Work (Name of co-author: Can Yang)
Formal analysis, Investigation, – review & editing</td></tr>
<tr><td colspan="3">Co-author’s Contribution to the Work (Name of co-author: Chi-Fai Leung)
Formal analysis, Investigation, – review & editing</td></tr>
<tr><td colspan="3">Co-author’s Contribution to the Work (Name of co-author: Yu Huang)
Formal analysis, Investigation, – review & editing</td></tr>
<tr><td colspan="3">Co-authors’ Declaration I declare that:
• I have read the declaration from the all authors
• The information is correct and the description of their contribution is in accordance with my view</td></tr>
<tr><td><i>Co-author’s Name</i> [2]
Min Zhou</td><td><i>Co-author’s Signature</i></td><td><i>Date (dd/mm/yy)</i>
<i>23 Jan 2025</i></td></tr>
</table>

Co-author's Name [2] Wing-Kei Ho	*Co-author's*	*Date (dd/mm/yy)*
Co-author's Name [2] Jincheng Mu	*Co-author's Signature*	*Date (dd/mm/yy)* *23 Jan 2025*
Co-author's Name [2] Xueying Wang	*Co-author's Signature*	*Date (dd/mm/yy)* *23 Jan 2025*
Co-author's Name [2] Pui-Yu Ho	*Co-author's Signature*	*Date (dd/mm/yy)* *23 Jan 2025*
Co-author's Name [2] Can Yang	*Co-author's Signature*	*Date (dd/mm/yy)* *23 Jan 2025*
Co-author's Name [2] Chi-Fai Leung	*Co-author's Signature*	*Date (dd/mm/yy)* *23 Jan 2025*
Co-author's Name [2] Yu Huang	*Co-author's Signature*	*Date (dd/mm/yy)* *23 Jan 2025*

Candidate's Declaration

I declare that:

- I have complied with the Thesis Examination Procedure
- The publications I have include in the folio meet the requirements for the submission of folios, and the publications are listed below.

Name	**Signature**	**Date (dd/mm/yy)**
Chen Wu		23 Jan 2025

Principal Supervisor's Declaration I declare that: • The information above is accurate • The thesis proposal presentation panel / qualifying examination panel has approved this candidate to submit their research work in the form of a folio (Date of approval: **23 Jan 2025**) • All of the co-authors of the publications included have reviewed the above information and signed in the appropriate places		
Supervisor's Name Ho Wing Kei	**Supervisor's Signature**	**Date (dd/mm/yy)** **23 Jan 2025**

Programme Director's Declaration I declare that: • The information above is accurate • The listed publications are included in compliance with the requirements for the submission of folios • The minimum requirements for the format of the folio have been met.		
Name	**PD's Signature**	**Date (dd/mm/yy)**